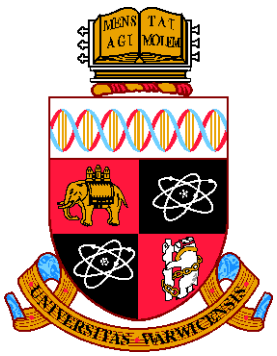

A Study of Tantalum-Based Perovskites as Anode Materials for Lithium-Ion Batteries

By

Badriya Nasser Alhashmi

Thesis

Submitted to the University of Warwick

for the degree of

Doctor of Philosophy

Department of Physics

January 2018

THE UNIVERSITY OF WARWICK

Contents

List of Tables **V**

List of Figures **VI**

Acknowledgments **XII**

Declarations **XIII**

Abstract **XIV**

Chapter 1 Introduction **1**

1.1 Thesis Plan 1

1.2 Motivation and Aim. 2

References 8

Chapter 2 Literature Review Of Battery Technology **10**

2.1 Brief History of Lithium-Ion Batteries 14

2.2 Latest Technology of Lithium-Ion Batteries 15

2.3 Electrode materials 18

2.3.1 Cathode Materials 22

2.3.2 Anode materials 26

2.2.4 The electrolyte 30

2.3 The Use of Metal Tantalite as Lithium Ion Storage Material, $MTaO_3$ (M= Li, Na, K) 32

References 33

Chapter 3 Methodology And Techniques **42**

3.1 Materials synthesis techniques 42

3.1.1 Hydrothermal Synthesis 42

3.1.2 Sol-Gel Synthesis 44
3.1.3 Solid-State Reaction 46
3.2 Materials Characterization and Morphology 47
3.2.1 X-ray Diffraction 47
3.2.2 Scanning electron microscopy (SEM) 51
3.3 Transmission electron microscopy (TEM) 57
3.4 Electrochemical Testing 58
3.3.1 Rate capability Test 59
3.3.2 Cyclic voltammetry 60
3.3.3 Electrode fabrication 62
References 66

Chapter 4 Material Synthesis And Electrochemical Properties Of Sodium Tantalate Nanoparticles, $NaTaO_3$ 69

4.1 Material synthesis 69
4.2 Results and Discussion 71
4.3 Electrochemical properties 78
4.4 Conclusion 85
References 88

Chapter 5 Material Synthesis And Electrochemical Properties Of Lithium Tantalate, $LiTaO_3$ 89

5.1 Material synthesis 89
5.2 Results and Discussion 91
5.3 Electrochemical Properties of Lithium Tantalate, $LiTaO_3$ 93
5.4 Conclusion 102
References 103

Chapter 6 Material Synthesis And Electrochemical Properties Of Potassium Tantalate, $KTaO_3$ 104

6.1 Material synthesis 104
6.1.1 Solid state synthesis of $KTaO_3$ perovskite Phase 105

6.1.2 Hydrothermal Synthesis of $KTaO_3$ Perovskite Powder 109
6.2 Results and Discussion 111
6.3 Electrochemical Properties of Potassium Tantalate, $KTaO_3$ 114
Electrochemical properties 115
6.4 Conclusion 120
References 122

Chapter 7 Conclusions **123**
Summery of Work Done 124
Suggestions for Future Work 124

Abbreviations **126**

List of tables

Table 1. 1: Table shows the Power consumption of different households (Germany) in the years 1996 and 2011 (in % of household's total consumption) (Hayn et al., 2014) . 5

Table 2. 1: Several positive electrode materials and their capacities. *17*

Table 2. 2: A listing of various negative electrode materials and their charge storage capacity. *17*

Table 2. 3: Common electrolyte salts used in lithium-ion cells and their corresponding conductivities. (Robinson & Stokes, 2002) *31*

Table 4. 1: A breakdown of the sample synthesis procedure for a typical synthesis set up. *70*

Table 5. 1: A breakdown of the sample synthesis procedure for a typical Sol-gel synthesis *90*

Table 6. 1: A breakdown of the sample synthesis procedure for a typical hydrothermal synthesis *111*

List of Figures

Figure 1. 1 world population, essential energy consumption, and CO2 emissions. Source: International Energy Agency (IEA) (Agency, 2007).....3

Figure 1. 2 : A graph showing the Worldwide energy usage distributed by region. (Agency, 2007) 4

Figure 1. 3: A plot showing the specific energy and volumetric energy for various battery chemistries (Landi et al., 2009).....6

Figure 2. 1: A schematic illustration for the working mechanism of a lithium-ion battery (a rocking chair type).(Xu et al., 2014).....11

Figure 2. 2: Image displays the intercalation process of lithium ions into a graphitic structure.(Stavins et al., 2003) 12

Figure 2. 3: Illustration of a lithium ion cell including all safety features. (Miller, 2015; Small et al., 2001 12

Figure 2. 4: collection of some familiar types of lithium-ion batteries, battery packs, and their safety concerns. (Warner, 2015). 13

Figure 2. 5: Modified schematic illustration of a lithium-ion battery during the charging/discharging process. The right-hand side shows the layered structure of $Li1\text{-}xCoO_2$ material, and the left side represents the anode as graphite sheets. During charging, the lithium-ion migrate from the cathode (positive electrode) to the anode (negative electrode). lithium-ion migrate the opposite direction during the discharging process (Aurbach et al., 2000; Lin et al., 2015; Nishimura et al., 2008). 20

Figure 2. 6: Image representing Li dendritic growth (a). displays a real secondary electron image of such a structure as grown in a cell (b) displays the Li dendritic growth was avoided when different material than lithium metal is used as electrode. (JM Tarascon 2001).....21

Figure 2. 7:.Potential vs. Li^+/Li state of charge on cycling Li_2FeSiO_4 material at a current rate of 10 mA/g (C/16) (Armstrong et al., 2011; Chen, 2013). Copyright 2011 American Chemical Society.....25

Figure 2. 8: Crystal structures of alkali metal tantalates: $LiTaO_3$, $NaTaO_3$, $KTaO_3$.....32

Figure3. 1: Photo of a stainless-steel autoclave and its Teflon liner 43

Figure3. 2: Schematic diagram of the stainless-steel autoclave and the Teflon liner. (Liu et al., 2007).....44

Figure3. 3: Schematic diagram shows an overview synthesis and the possible routes on synthesising of Nano-particles and crystalline films. 45

Figure3. 4: Illustration shows a Sol-gel method as condensation-based system formation reactions. (Feinle et al., 2016) 46

Figure3. 5: diffraction of X-ray beam on crystal planes, Bragg's law. 48

Figure3. 6: Schematic diagram of the essential components of XRD equipment. (Sharma et al., 2012).....49

Figure3. 7: The Panalytical X-Pert Pro MPD powder diffractometer at X-ray Diffraction facility. (physics department, university of Warwick). 51

Figure3. 8: A schematic diagram of scanning electron microscope (SEM). 53

Figure3. 9: Illustrated diagram, up the outcomes of the interaction of electron beam with sample. Down: the interaction volume as encountered by SEM and the regions of the various detected signals. (Biswas, 2016; Microscopy, 2013). 56

Figure3. 10: Schematic diagram of TEM.....58

Figure3. 11: Linear sweep at rate of 0.1 mV/s in the range of 3.5 - 4.3 V vs. Li/Li+. 61

Figure3. 12: A diagram represents the two electrode Swagelok test cell. (Canas et al., 2013).....64

Figure3. 13: Components of coin cell. (Solarajan et al., 2016).....65

Figure 4. 1: X-Ray diffraction pattern of $NaTaO_3$ Nano-cubes.....71

Figure 4. 2: A general SEM image showing the well-defined cubic shaped morphology of $NaTaO_3$ Nano-cubes.....72

Figure 4. 3: SEM images (top and bottom) of obtained $NaTaO_3$ Nano-cubes obtained at two different magnifications exhibiting that the typical size of the Nano-cubes is in the range of 200-450nm.....73

Figure 4. 4: HRTEM images and inset electron diffraction patterns of two $NaTaO_3$ Nano-cubes. Left crystal is an oblique projection, right is along [010].....74

Figure 4. 5: A histogram shows the length distribution of 396 measured sides of our $NaTaO_3$ Nano-cubes structure.....75

Figure 4. 6: Histogram of the enclosing volume calculated for each measure Nano-cubes. All measured Nano-cubes were assumed to be perfect cubes in the calculation.....76

Figure 4. 7: A Calculated surface area for 396 Nano-cubes.....77

Figure 4. 8: A histogram showing surface area to volume ratio for various selected Nano-cubes particles; using SEM image. (Yu et al., 2015).....77

Figure 4. 9: SEM images of sodium Tantalate, $NaTaO_3$ electrode before use at different magnifications. The particles show well distribution on the electrode surface.....79

Figure 4. 10: The electrochemical performance profile of the $NaTaO_3$ electrode at 10mA/g for 16 cycles and the Galvanostatic charge/ discharge at 10mA/g for the 1st and 2nd cycles.as a comparison of the capacity drop between the first and the second cycles.....80

Figure 4. 11: Constant current cycling at 10 mA/g. Notice that the time for the first cycle was longer than the subsequent cycles.....81

Figure 4. 12: CV curves of $NaTaO_3$ at seven different scan rates speeds; 0.5mVs^{-1}, 1 mVs^{-1}, 5 mVs^{-1}, 10 mVs^{-1}, 25 mVs^{-1},50 mVs^{-1}, and 100 $mVs^{-1}$for the 2^{nd} cycle of each ramping voltage.....82

Figure 4. 13: Initial four CV curves of the $NaTaO_3$ electrode at scan rate speed of 10 mVs^{-1} between the voltage range of 3.0 -0.1 V vs. Li^+/Li.....83

Figure 4. 14: Initial four CV curves of the $NaTaO_3$ electrode at scan rate speed of 100 mVs^{-1} between the voltage range of 3.0 -0.1 V vs. Li^+/Li.....84

Figure 4. 15: Cyclic voltammetry curves of $LiTaO_3$ at a scan rate of 0.1 $mV\,s^{-1}$ in the voltage range 3–0.1 V vs. Li/Li^+. 86

Figure 4. 16: Cyclic voltammetry curves of $NaTaO_3$ at a scan rate of 0.1 $mV\,s^{-1}$ in the voltage range 3–0.1 V vs. Li/Li^+. 87

Figure 5. 1: SEM micrographs of Lithium Tantalate particles at different magnifications: a) 3.6k, b)15.6k.....91

Figure 5. 2: XRD profile of $LiTaO_3$ calcined at 750 ^0C for 12hrs with the major peaks indexed – all of the other peaks correspond to the phase pure material (Yamanaka, 2016).....92

Figure 5. 3: SEM micrographs of Lithium Tantalate particles at different magnifications: a) 3.6k, b)15.6k.....92

Figure 5. 4: SEM images with different magnifications for the prior to use $LiTaO_3$ electrode. 95

Figure 5. 5: SEM images with different magnifications for #6 coin cell electrode after use.....96

Figure 5. 6: The electrochemical performance profile of the $LiTaO_3$ electrode at 10mA/g for 16 cycles and the Galvanostatic charge/ discharge at 10mA/g for the 1st and 2nd cycles as a comparison of the capacity drop between the first and the second cycles. 97

Figure 5. 7: Constant current cycling at 10 mA/g.notice that the time for the first cycle was longer than the subsequent cycles.....98

Figure 5. 8: CV curves of $LiTaO_3$ at seven different scan rates speeds; 0.5mVs^{-1}, 1 mVs^{-1}, 5 mVs^{-1}, 10 mVs^{-1}, 25 mVs^{-1},50 mVs^{-1}, and 100 $mVs^{-1}$for the 2nd cycle.....99

Figure 5. 9: Initial four CV curves of the $LiTaO_3$ electrode at scan rate speed of 10 mVs^{-1} between the voltage range of 3.0 -0.1 V vs. Li^+/Li. 100

Figure 5. 10: Initial four CV curves of the $LiTaO_3$ electrode at seven different scan rate speed of 10 mVs^{-1} between the voltage range of 3.0 -0.1 V vs. Li^+/Li 101

Figure 6. 1: XRD pattern of $KTaO_3$ powder sintered at 0^0C, 1000^0C, and 1200^0C 106

Figure 6. 2: XRD pattern of $KTaO_3$ powder sintered at 1000^0C, and 1200^0C and the existence of pyrochlore phase 107

Figure 6. 3: XRD pattern of $KTaO_3$ powder sintered at 1300^0C, and the profile shifted away from the pure perovskite structure. 108

Figure 6. 4: SEM image of solid state synthesised $KTaO_3$ powder showing the multiphase nature of the product. 109

Figure 6. 5: XRD profile of $KTaO_3$ hydrothermally obtained at 240°C for 24hrs which has an excellent match with the published structure (Zhurova et al., 1992). 112

Figure 6. 6: SEM images for 2 different samples of potassium tantalate, $KTaO_3$ cubes synthesised using the hydrothermal synthesis method showing high magnification (top) and low magnification image. 113

Figure 6. 7: a) shows the ideal $KTaO_3$ structure and b) SEM image of potassium tantalate, $KTaO_3$ cubes prepared by hydrothermal synthesis. 114

Figure 6. 8: Swagelok cells assemblies as used in this study. Right the cells placed under increased compression to ensure electrical contact through the cell. 115

Figure 6. 9: CV curves of $KTaO_3$ at seven different scan rates speeds; $0.5mVs^{-1}$, mVs^{-1}, $5\ mVs^{-1}$, $10\ mVs^{-1}$, $25\ mVs^{-1}$,$50\ mVs^{-1}$, and $100\ mVs^{-1}$for the 2^{nd} cycle. 116

Figure 6. 10: Initial four CV curves of the $KTaO_3$ electrode at seven different scan rate speed of $10\ mVs^{-1}$ between the voltage range of 3.0 -0.1 V vs.Li^+/Li. 118

Figure 6. 11: Galvanostatic charge/ discharge profiles of the $KTaO_3$ electrode at 10mA/g for: a) 16 cycles, b) The second cycle. Significant number of Li+ migrate one-way route during the first de-lithiation. 119

Figure 6. 12: Constant current cycling at 10 mA/g, as the cell potential ramping within the chosen potential window of 3.5V- 0.1V. The first cycle took

considerable time to complete the cycle compared to the subsequence cycles. *120*

Acknowledgments

Initially, I would like to thank my supervisor Dr Jeremy Sloan for his endless guidance and support throughout my PhD project; along with Professor Chris McConville for his supervision during the period from my fresh start at the University of Warwick until the moment I submitted this thesis. I would have never been able to finish my thesis without their guidance, motivation and patience.

A big thank you goes to Dr Susan Borrows, for all the help she has provided, with regards to using the setup in the downstairs labs and for introducing me for the first time to the solid-state synthesis. I am also particularly grateful to Dr Scott Gorman for all his patience and support during my work in their labs and special thanks for Dr Emma Kendrick for giving me the opportunity to wo test my materials in her labs. Thanks also go to Dr David Walker for training me in the use of the XRD machines. And once again I would like to say a special thanks to Dr Jeremy Sloan, and Prof. Chris McConville.

Finally, this work would not have been possible without the unlimited support of my family; my husband Salim, my children Jay, Mazin, Yumna, and Aalia. My endless appreciation and gratefulness will always be for the most influencing person in my life and will forever be, dearest Mum, Maryam Salim. And finally thank you to you, the reader, for taking the time to read this document.

Declarations

This thesis is submitted to the University of Warwick, UK, as part of the requirements for the admission to the degree of Doctor of Philosophy. The work described within was performed during the period from March 2013 to January 2018 under the supervision of Dr Jeremy Sloan and Prof. Chris McConville and, unless otherwise specified, was carried out by myself.

Electron microscopy measurements were undertaken at the Microscopy at Warwick group facility. Transmission electron microscopy was performed with the full assistance of Dr Jeremy Sloan.

Electrochemistry experiments were conducted at the Warwick Manufacturing Group laboratories, University of Warwick, UK.

Powder XRD measurements were conducted at the X-ray diffraction suite at the University of Warwick.

Abstract

In this thesis, I demonstrate my work on three types of Nano-particle materials, all of the perovskite structure with the intention to study their lithium-ion storage features. Two types of perovskite tantalates; sodium tantalate, $NaTaO_3$, and potassium tantalate, $KTaO_3$ were grown hydrothermally in this work. The third perovskite material; lithium tantalate, $LiTaO_3$ was produced by Sol-gel method. The structure morphology was investigated by scanning electron microscopy SEM and powder X-Ray Diffraction. The electro chemical properties were investigated using both; the cyclic voltammetry (CV), and the charge discharge profile which gave us a better understanding of their abilities of lithium ions. Half -cells were used for the study. Coin cells, as well as two-electrode Swagelok cells, were used.

The hydrothermal synthesis has produced a fine powder product of sodium tantalate and potassium tantalate. The solid-state method was used to produce the potassium tantalate material as well. A quality product of lithium tantalate was produced by Sol-gel method. The electrochemical properties were tested. The consistent resultant capacity of the type of material acting as an active material for lithium ion storage is quite interesting. It showed better electrochemical stability than the other two materials; potassium tantalate and sodium tantalate. The electrochemical test shows that there is a relatively high drop in the value of the irreversible capacity after the first cycle for the three materials. More studies must be conducted to give explanations and solutions leading to solid electrochemical findings. Initial test cells were constructed and tested, but solid electrochemical results could not be gathered before the end of the project.

Chapter 1

Introduction

Air pollution and global warming are among the damaging impacts on the environmental and climate caused by using coals and fossil fuels. On the other hand, one of the most promising solutions is the use of renewable energy, i.e. wind power and solar energy. Hence, the need for the higher energy power, density storage device is becoming more and more apparent as the energy demand is increasingly supplied by the renewable sources (Feldman et al., 2014). For instance, in the last couple of decades, one has observed a dramatic decrease in the electrical power cost produced by green energy, i.e. photovoltaic (PV) panels, rechargeable batteries etc.

1.1 Thesis plan

This project is aimed at studying three types of perovskite materials for the use of anodes in lithium-ion batteries. These batteries are used in essentially all modern electronic devices, extending from mobile phones over laptops to automobile systems such as electric vehicles and planes. They are therefore a pillar of the universal power storage challenge, and intensive and continuous scientific research is pledged to enhance their proficiencies. The materials under study in this project were planned to be used as anodes contained within lithium-ion cells. First, they were physically characterised to investigate their topological properties and then tested as half cells (coin cells and Swagelok cells). Additionally, the aim was to try to investigate the exact relationship between the topology of nanoparticles of the produced material and their electrochemical properties.

This chapter is a general introduction to the thesis. Chapter Two is a literature review of lithium-ion batteries, their components, and electrochemical principles. The third chapter is about the experimental methods which were used in this project. Chapter four,

five, and six are the characterisation and electrochemistry results discussion of the sodium tantalate, $NaTaO_3$ material, lithium tantalate, $LiTaO_3$ material and the potassium tantalate, $KTaO_3$ material, respectively. The final chapter; chapter seven is a general conclusion and future work

1.2 Motivation and Aim

The voltaic pile, which was invented in the early nineteenth century, was the first use of electrochemically energy storage. Batteries have delivered a terrific alternative source of energy for non-connected to the grid applications, i.e. portable fashion devices, or where consumption is separated from production in time, i.e. power storage (Tarascon & Armand, 2001).

Over the last five decades, universal significant changes have undergone on the worldwide number of population. As an example, in 1999 it was recorded to be approx. 5.98 billion (Cincotta *et al.*, 2000), which has increased the demand not just on the consumption of the power in general, but the general power consumption per individual was intensely increased with time as well (Cincotta *et al.*, 2000). This rapidly increases usage of the world energy has raised the alarm on the supply of different resources of energy, the limitation of these energy resources, and the negative effect on the environment, such as global warming, change of climate all over the world, due to ozone layer depletion, air pollution, etc. (Dorian *et al.*, 2006; Figueroa *et al.*, 2008; Sieminski, 2014).

Taking as an example, the energy consumption data collected for 20 years for the years from 1984- 2004 in a study conducted by the IEA (International Energy Agency). This data raised the alarm with the rapidly growing population. Figure1.1 shows that the consumption of the essential energy has increased by nearly 50%, compared to the 33% increase in the world population, and by more than 40% for the CO2 emissions. The graphs show that the average annual increment was 2% and 1.8% respectively (Agency, 2007; Figueroa *et al.*, 2008).

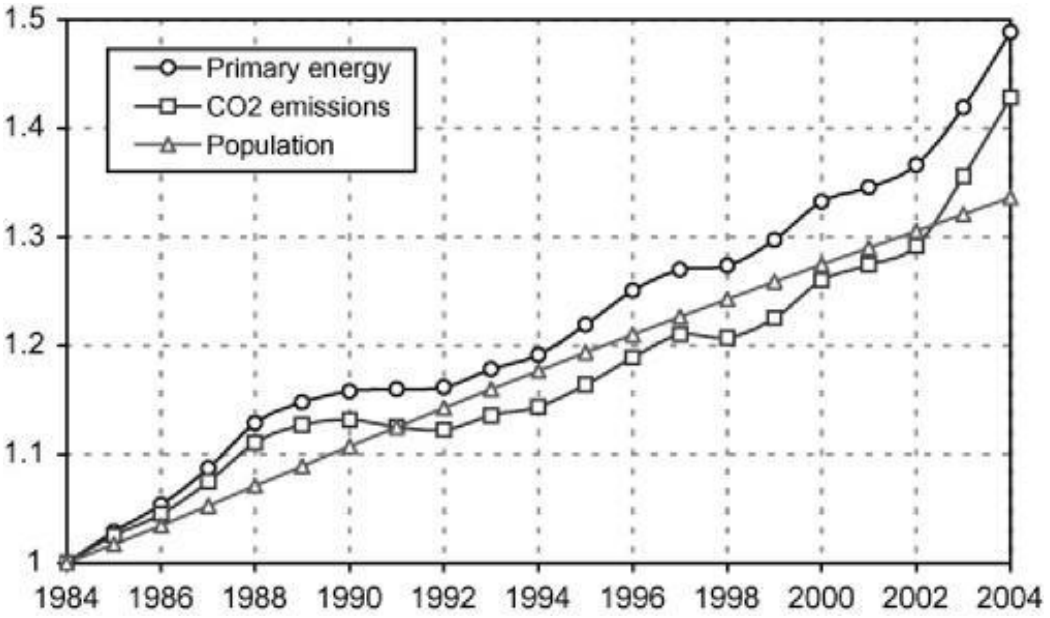

Figure 1. 1 world population, essential energy consumption, and CO2 emissions. Source: International Energy Agency (IEA) (Agency, 2007).

Present estimations indicate that the rising tendency in the primary energy consumption will rapidly continue and directly proportional to the growing number population over the years.

In the same study (Figure 1.2), the growing rate is about 3.2% of primary energy usage for emerging economies such as: Middle East, South Asia, Africa, and South America countries, and expected to exceed that for the developed countries (United States, Canada, Japan, Australia, Western Europe, and New Zealand) by 2020. The case is more concerning for Chain, which has doubled its consumption in just twenty years with 3.7% average growth rate (Agency, 2007; Sieminski, 2014).

Moreover, the third world households have experienced a dramatic increase in average primary energy consumption as well, due to enormous development in the technology in the recent years, succeeding to catch up with the developing countries. Al the above factors have left the global population in an increasing demand for primary energy consumption and a rising noteworthy issue of this primary energy distribution in the first place. The innovation of primary power grids and the raising distribution of fuel networks can recompense to a level, but it raises the need to find improved methods for the

power to be stored and transported, especially off-grid electricity (Dorian et al., 2006; Nishi, 2001).

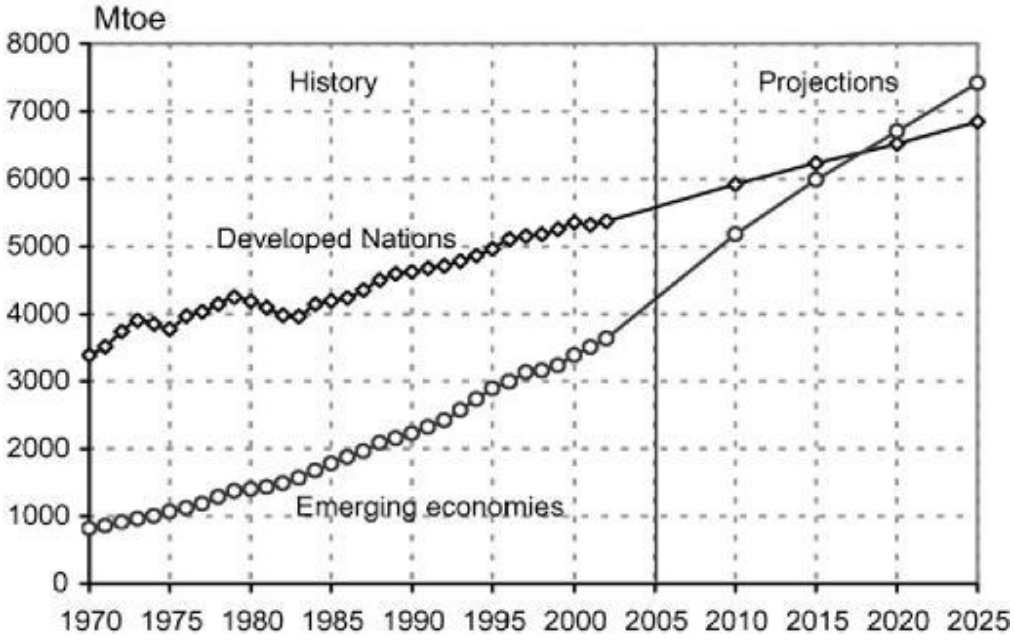

Figure 1. 2 : A graph showing the Worldwide energy usage distributed by region. (Agency, 2007)

Similarly, with the rising silicon era, the demand for the use of electronic devices has significantly increased starting from the professional use of the entertainment to another different usage. This leads to a tremendous rise in power/primary energy consumption (Table 1.1). Table 1.1 below shows that the power consumption of the TV, office and audio has tripled in the year 2011 from that in 1996, where it remained the same for water heating.

Use	1996	2011
Hot Water	14.8%	14.8%
Office, TV, and Audio	6.7%	25.5%
Coolers & Freezers	22.6%	16.7%
Dishwashing, Washing, & Drying	10.4%	12.4%
Lighting	9.2%	8.1%
Cooking	9.6%	9.8%
Other purposes electrical appliances (Gardening, Wellness, Climate, etc.)	26.8%	12.5%

Table 1. 1: Table shows the Power consumption of different households (Germany) in the years 1996 and 2011 (in % of household's total consumption) (Hayn et al., 2014)

With the advances in material science research, the invention of portable electronic devices made life become easier but growing the number of built-in characteristics on the other hand. As a result, this has doubled the energy consumption of these devices multiple times and raising the need of developing the means of storing energy in some portable fashion devices. As such minimised devices didn't allow for a simple increase in battery size, it became essential to improve the storage features of these batteries.

The lead-acid battery has been the most popular energy source associated with the early start of the automotive industry, due to its components low cost and the system robustness in general, which made lead-acid battery the most excellent candidate for such applications.

Figure.1.3 shows a comparison plot of volumetric energy and the energy density of various battery chemistries. Concerning both gravimetric and volumetric energy density, the lead-acid battery isn't the best chemistry of choice. The same plot shows that Ni-MH makes a decent alternative regarding the performance enhancement; with lighter weight and smaller enhanced size. The energy density (WhI^{-1}) ranges between ~100-300 and the energy density ($Whkg^{-1}$) is above 50. This battery type later conquered the portable power

tools market because of its light weight which made it suitable for handheld devices and its higher power. In theory, lithium-based batteries have the best features regarding the weight, size, and the performance but unfortunately, they were not representing a real competition for a long time because of the high cost and reliability regarding the functioning cells production (Tarascon & Armand, 2001).

The discovery of portable fashion devices, i.e. mobile phones, laptops, etc., has created a dramatical demand for increased battery performance. In the early 1980s, promising anode and cathode materials were already discovered, as a result of the impact research on the Li-ion batteries (LIBs). The actual commercialisation of LIBs didn't take place until a decade later though, by the original work of Sony & Asahi Kasei (Nishi, 2001). LIBs market has had high demand since then; this is not only because of the increasing

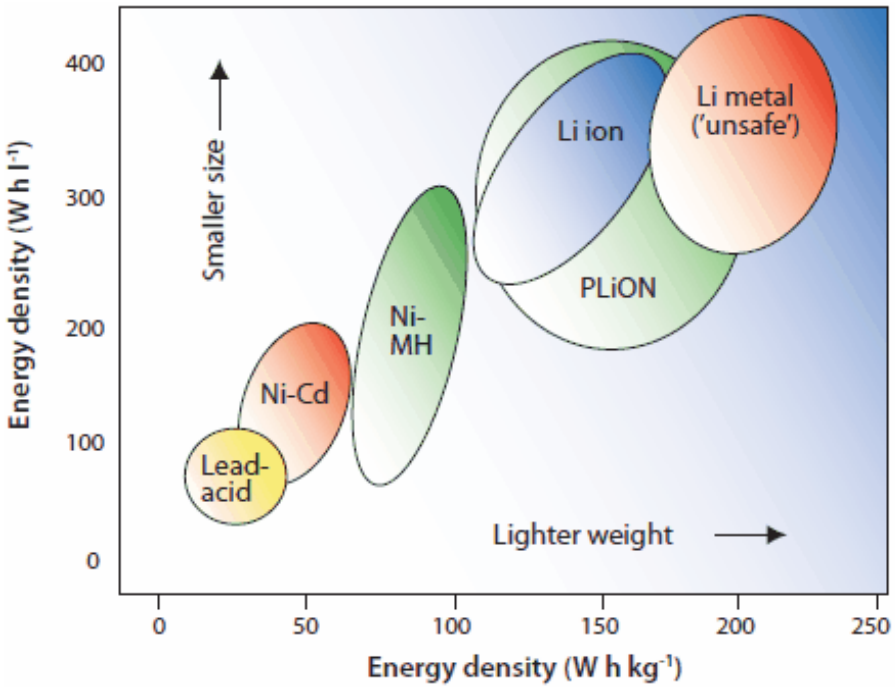

Figure 1. 3: A plot showing the specific energy and volumetric energy for various battery chemistries (Landi et al., 2009)

worldwide usage of portable electronic devices but due to rising environmental concerns as well. This had opened the door to the hybrid and electric vehicles development which created a brand new market for the LIBs to expand through (Goriparti et al., 2014; Han et al., 2009).

The last point to be considered is the increasing concerns about the global greenhouse effect. The climate change has been under the microscope for the last two decades, and more studies concluded that the rapid use of coal, fossil fuels, natural gas, oil as a dirty source of energy, increases the global warming emissions. Globally, fossil fuels and oil are the dominant energy source used to produce electrical energy and transport. They have been slowly challenged by innovative technologies such as nuclear and renewable energy in the electricity production sector and hybrid and electric vehicles. However, because of the discontinuous nature of renewable energy sources, effective storage and mobile system are crucial (Guerard & Herold, 1975; Nishi, 2001; Palacin, 2009).

Lately, there has been a noticeable development in the mobile electric systems which can contend traditional oil cars. The Model S vehicles produced by Tesla is the most remarkable

References

Feldman, D., Barbose, G., Margolis, R., James, T., Weaver, S., Darghouth, N., Fu, R., Davidson, C., Booth, S. & Wiser, R. (2014) Photovoltaic system pricing trends. *US Department of Energy*,

Tarascon, J.-M. & Armand, M. (2001) Issues and challenges facing rechargeable lithium batteries. *Nature*, 414 (6861): 359-367.

Agency, I. E. (2007) *Key world energy statistics*. International Energy Agency.

Cincotta, R. P., Wisnewski, J. & Engelman, R. (2000) Human population in the biodiversity hotspots. *Nature*, 404 (6781): 990-992.

Dorian, J. P., Franssen, H. T. & Simbeck, D. R. (2006) Global challenges in energy. *Energy Policy*, 34 (15): 1984-1991.

Figueroa, J. D., Fout, T., Plasynski, S., McIlvried, H. & Srivastava, R. D. (2008) Advances in CO 2 capture technology—the US Department of Energy's Carbon Sequestration Program. *International journal of greenhouse gas control*, 2 (1): 9-20.

Goriparti, S., Miele, E., De Angelis, F., Di Fabrizio, E., Proietti Zaccaria, R. & Capiglia, C. (2014) Review on recent progress of nanostructured anode materials for Li-ion batteries. *Journal of Power Sources*, 257 (Supplement C): 421-443.

Guerard, D. & Herold, A. (1975) Intercalation of lithium into graphite and other carbons. *Carbon*, 13 (4): 337-345.

Han, J.-T., Liu, D.-Q., Song, S.-H., Kim, Y. & Goodenough, J. B. (2009) Lithium-ion intercalation performance of niobium oxides: KNb5O13 and K6Nb10. 8O30. *Chemistry of Materials*, 21 (20): 4753-4755.

Hayn, M., Bertsch, V. & Fichtner, W. (2014) Electricity load profiles in Europe: The importance of household segmentation. *Energy Research & Social Science*, 3 30-45.

Landi, B. J., Ganter, M. J., Cress, C. D., DiLeo, R. A. & Raffaelle, R. P. (2009) Carbon nanotubes for lithium-ion batteries. *Energy & Environmental Science*, 2 (6): 638-654.

Nishi, Y. (2001) Lithium ion secondary batteries; past 10 years and the future. *Journal of Power Sources*, 100 (1): 101-106.

Palacin, M. R. (2009) Recent advances in rechargeable battery materials: a chemist's perspective. *Chemical Society Reviews*, 38 (9): 2565-2575.

Sieminski, A. (2014) International energy outlook. *Energy Information Administration (EIA)*,

Zhou, P. (2010) Electric vehicle thermal management system.

Chapter 2 Literature Review of Battery Technology

The fundamental concept of Lithium-ion battery can be concluded into two basic chemical reduction and oxidation reactions separated in space and forcing the electrons to transfer in an external circuit; producing power which is used for powering a desired electric device. The initial or first generation of batteries operated an irreversible chemical process restricting them to be used for once only. These type of batteries called primary batteries. On the other hand, lithium-ion batteries, i.e. LIBs are built so that the chemical process is reversible, enabling periodic recharging process after use, yielding so-called secondary batteries. Factually, secondary batteries frequently undertook a pre-cycling at the factory before they can be ready for market. The prefixes 'secondary' and 'primary' are therefore standing for which cycle the battery is in when they are marketed.

The essential safety concerns with dendrite formation and subsequent short-circuiting forced the "rocking chair" achievement cells type in which intercalation of lithium ions into graphite prevented the dendrite formation to allow maximum volumetric and gravimetric capacities of metallic lithium (Xu *et al.*, 2014). Figure. 2.1 shows a schematic illustration of the basic workings of a secondary battery of a 'rocking chair' type. More details on this type are provided in section 2.3. The negative electrode represents the anode, and the positive electrode is the cathode which hosts intercalation materials in which lithium ions travel amongst during discharge-charge processes, Figure 2.2. lithium ions move from anode to cathode during the discharge process (usually called the normal operation), while the direction is reversed during the charging process.

Lithium-ion batteries adopt a wide range of different forms. However, they can be split into the following main categories (Balakrishnan *et al.*, 2006; Mikolajczak, 2011):

1- Cylindrical Cells (Small/Large), similar to the standard AA batteries in shape. Figures 2.3, and 2.4 illustrate the cylindrical shape cells and some other types of lithium batteries with all safety features.

2- Coin Cells (common examples are the industry standards CR2016 and CR2032);

3- Pouch Cells (mobile phone batteries);

4- Prismatic (takes a range of different shapes; e.g. laptop and electric vehicle batteries.

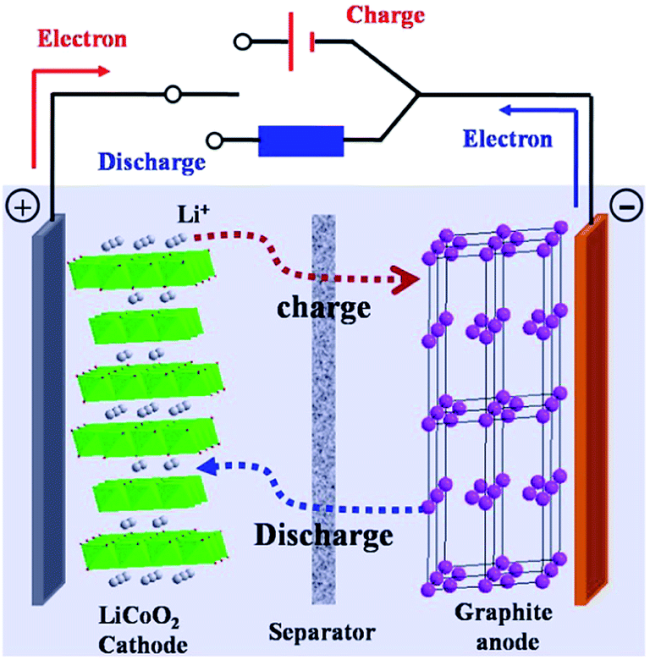

Figure 2. 1: A schematic illustration for the working mechanism of a lithium-ion battery (a rocking chair type).(Xu et al., 2014)

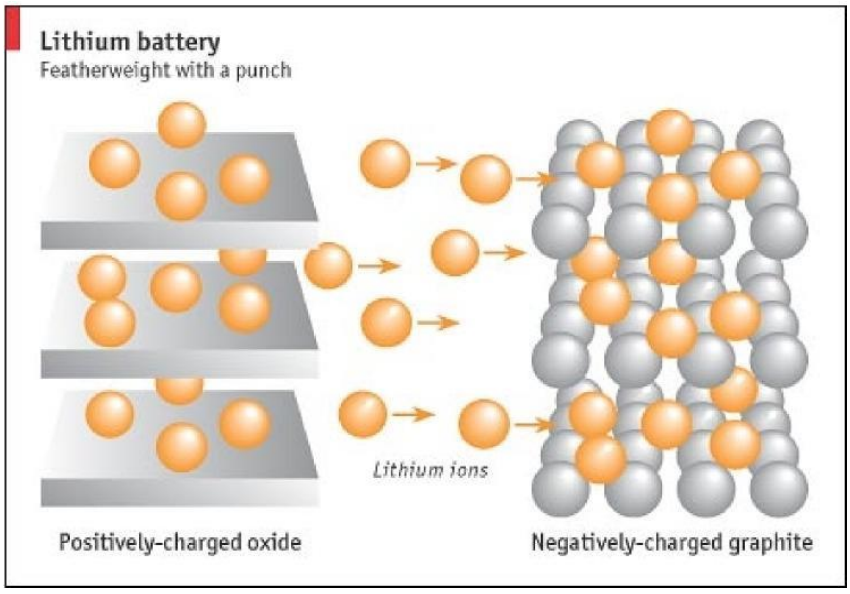

Figure 2. 2: Image displays the intercalation process of lithium ions into a graphitic structure.(Stavins et al., 2003)

Figure 2. 3: Illustration of a lithium ion cell including all safety features. (Miller, 2015; Small et al., 2001

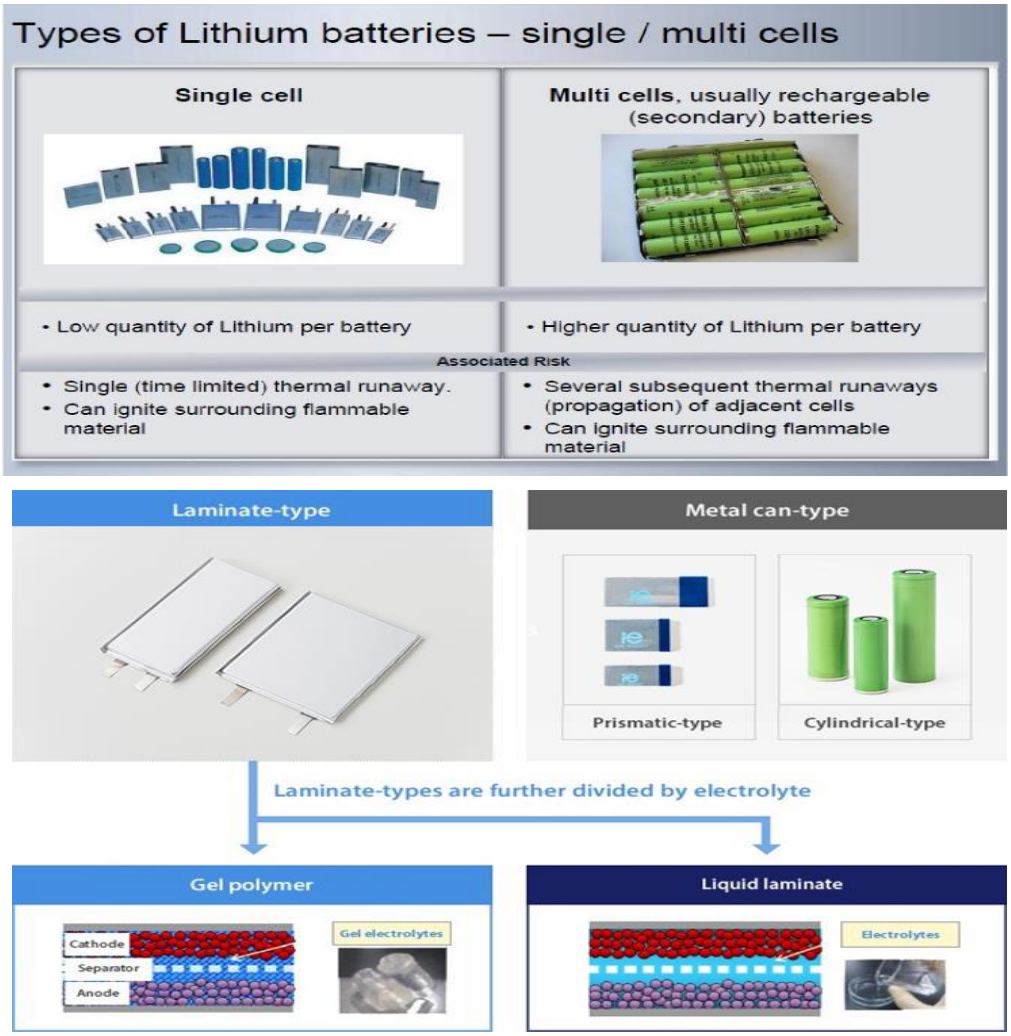

Figure 2. 4: A collection of some familiar types of lithium-ion batteries, battery packs, and their safety concerns. (Warner, 2015).

2.1 Brief History of Lithium-Ion Batteries

Using lithium-ion batteries as electrical energy storage was first introduced by M. Whittingham in the middle of1970. He used a prototype cell with lithium metal and titanium sulphide as electrodes (Whittingham, 1976).

Usage of metallic lithium had severe downsides due it's high reactive features and for known as very unstable if it contacts atmospheric (Kirchhoff & Bunsen, 1861). The main research aim back then was to develop better choices of more stable and less hazardous lithium-based compounds electrodes rather than the pure metal.

The first successful attempt was carried by J.O. Besenhard, who was able to show the lithium intercalation in both graphite and chromium oxides and Mn3Se4 cathodic material (Besenhard & Fritz, 1974; Besenhard & Schöllhorn, 1977; Schöllhorn *et al.*, 1977) in the mid-1970s in Germany, as previously illustrated in Figure 2.2.

Apart from the significant importance of this work, having in mind the fact that Besenhard was not just able to exhibit the intercalation into the mentioned materials but he was able to prove the reversible reaction is possible. At that time, the electrolyte used in the lithium-ion cells represented the main severe issue the cells suffered from. In 1979, (Basu *et al.*, 1979) was able to develop a Li-ion intercalated graphite electrode replacing the hazardous metallic lithium.

In 1981, a discovery of LiCoO2 compound by J. Goodenough and K. Mizushima when they were inspecting list compounds of $A_xM_yO_2$ type when this compound became the most important compound in the lithium-ion batteries development searches due to its high stability and safety characteristics at that time. The fact that LiCoO2 compound is capable of donating lithium ion in the electrochemical cells, made it possible to build Li-ion cells which do not depend on lithium metal as a lithium ion source (Mizushima *et al.*, 1981). This fact made all the difference since then by giving up using lithium metal as the

only lithium source and opened the door for new possibilities in the lithium-ion batteries developments research.

A year earlier (1980), R. Yazimi used a new type of solid electrolyte to further improve already well-known graphite electrodes. The idea of solid electrolyte was to reduce the influence of the known issues at that time related to the use of liquid organic electrolytes, such as the electrolyte decomposition obstacle when cycling (Yazami & Touzain, 1983). His developed electrode type is being widely used since then in commercial lithium-ion cells.

In general, the mid-1980s can be said to be the start for lithium-ion batteries to be industrially possible. Another research carried by A. Yoshino created a model cell with carbonaceous material as negative electrode and $LiCoO_2$ as the positive electrode, eliminating the hazardous use of the pure lithium metal (Yoshino *et al.*, 1987). However, in the year 1991, a joint project between Sony and Asahi Kasei made the first lithium-ion battery officially became commercially possible to the public (Scott *et al.*, 2010)

Wide ranging research in the field has created various type of materials for use as an anode and/or cathode electrodes, and electrolytes and many more are definitely expected to be revealed in the future research.

2.2 Latest Technology of Lithium-Ion Batteries

Up-to-date lithium-ion batteries depend on the intercalation and de-intercalation of lithium ions in the host electrodes structural matrix. In the intercalation, lithium ions are hosted in vigorously constructive positions inside the electrode structure. Usually, this is accomplished via different processes depending on the host material of the electrode, e.g. the alloying process as is the case with silicon. (Chan *et al.*, 2008). During the de-

intercalation which is the opposite process of intercalation, lithium ions are freed from the host material electrode. The ions' transfer through electrodes is usually accompanied by equivalent electron current over the external circuit.

Lithium-ion battery (LIB) is one of several categories of chemical energy storage which can be attained by taking advantage of a reversible chemical reduction-oxidation reaction. Energy is released during the red-ox reaction, and electrons and ions are traded between the cathode and the anode yielding more stable, promising compounds.

A large number of recent electrical devices such as mobile phones, laptops, electric vehicles etc. count on lithium-ion batteries. The unique advantages of lithium-ion batteries compared to other types of energy storage, made them of a high demand recently. Not suffering from memory issues that can affect the usual battery operation and the fact that they can achieve very high energy because of the typical tiny size of the charge carrier, as well as the light weight in comparison with lead-acid batteries, made them an ideal candidate for the automotive industry.

The electrochemical features of lithium-ion battery differ significantly over several factors. Electrode material, electrolyte type i.e. voltage window, and the geometry of the cell itself all have a huge effect on the charge capacity. As an example, handheld devices usually depend on lithium-ion batteries with positive electrodes made from lithium iron phosphate or lithium cobalt-oxide. Table 2.1 shows a number of positive electrode materials compared to their measured capacities.

Electrode Material	Capacity (mAh/g)
Lithium-Cobalt Oxide, LiCoO2. (Chen et al., 2002)	130
Lithium-Iron Phosphate. (Chen & Whittingham, 2006)	145
Lithium-Nickle Manganese Cobalt Oxide. (Yoshizawa & Ohzuku, 2007)	185
Lithium Nickel Cobalt Aluminium Oxide. (Chen et al., 2004)	210
Lithium-Manganese-Oxide [xLi2MnO3 · (1 − x)Li + yMn2 − yO4 . (Johnson et al., 2005)	250
Metallic Lithium. (Fauteux & Koksbang, 1993)	3860

Table 2. 1: Several positive electrode materials and their capacities.

Similarly, there are some common negative electrodes such as graphite and other carbon compounds. A range of potential materials is listed in Table 2.2. Each material has got certain advantages, such as Lithium cobalt oxide-based electrodes delivering a high storage capacity, while lithium iron phosphate provides better safety properties.

Electrode Material	Capacity(mAh/g)
Lithium Titanate. (Tang et al., 2009)	125
Graphite. (Yazami, 1999)	372
Hard Carbon. (Wang et al., 2001)	430
Tin Oxide. (Brousse et al., 1998)	500
Silicon. (Chan et al., 2008)	4,200

Table 2. 2: A listing of various negative electrode materials and their charge storage capacity.

In certain circumstances, lithium-ion batteries can present huge safety hazardous, e.g. basic cells use lithium metal as a battery electrode, which, can aggressively react if it happens to be in contact with water, producing hydrogen gas and consequently may cause an explosion. Moreover, best known used electrolytes contain flammable organic compounds as well as toxic lithium-based salts. (Franco, 2015)

2.3 Electrode materials

In any lithium-ion battery, the three essential functional components are the electrodes, the positive electrode (cathode), the negative electrode (anode), and the electrolyte which ionically connects the two electrodes. Lithium metal is used to be used as a cathode in the early lithium-ion batteries, but for safety concerns, the pure metal was replaced by lithium compounds instead. On the other hand, carbon is still the most popular element used as the anode in lithium-ion batteries. however, it is also gradually being replaced by a higher charge capacity material, such as silicon (see Table. 2.1, 2.2).

In principle, current Lithium-ion batteries rely on phosphates such as LiFePO4 or transition metals oxides active materials, e.g. the widely investigated active materials, lithium metal cobalt oxide family, $LiCoO_2$, $LiCo_{1/3}Mn_{1/3}Ni_{1/3}O_2$, $LiMn_2O_4$, etc. These active materials are used as cathode materials. On the other hand, graphite is widely used as anode active material. They are separated by a polyethylene or polypropylene membrane separator, immersed in suitable electrolyte which is a mixture of organic solvents such as ethylene carbonate (EC) with dimethyl carbonate (DMC), propylene carbonate (PC), diethyl carbonate (DEC), and/or ethyl methyl carbonate (EMC) (Xu, 2004), at different ratio, mixed with some lithium salts, e.g. lithium hexafluorophosphate ($LiPF_6$).

The two main purpose of the separator is to prevent any electrical contact might occur between the anode and the cathode (i.e. negative charges movement between electrodes) and allowing only the diffusion of Li ions between the electrodes at the same time during the discharge/ charge process. The lithium-ion immigration from the cathode to the anode results in the conversion of electrical energy into chemical energy and vice versa, as it is a reversible process. Taking the charging process, for example, the chemical reactions on both sides in an ideal Lithium-ion battery with $LiCoO_2$ as a cathode active material and graphite as anode electrode are as follows (Poizot *et al.*, 2000);

$$\text{Anode side:} \quad C + xLi + xe^{-}{}_4 \leftrightarrow Li_xC_6 \tag{2.1}$$

$$\text{Cathode side:} \quad LiCoO_2 \leftrightarrow 4\,Li_1 - xCoO_2 + xLi + xe- \tag{2.2}$$

For a material, to be considered as an appropriate contender for a lithium-ion battery electrode, it must achieve the need for:

- good electric and ionic conductivity,
- excellent reversible capacity,
- long life cycling,
- great rate diffusion/host of Li ions into the active material,
- and finally, decisively low in cost (Armand & Tarascon, 2008).

More details of cathode materials using LiFePO4, LiCoO2, and, LiMn2O4, can be found in (Prakash *et al.*, 2010; Whittingham, 2004), while graphite is absolutely still the most suitable candidate for anode electrodes because of its outstanding characteristics, e.g. low & flat potential window compared with pure lithium metal, and for it's good cycling life, low cost, etc. (Li *et al.*, 2009; Marom *et al.*, 2011; Scrosati & Garche, 2010). However, in the above example, where $LiCoO_2$ represents the active material for the cathode, graphite permits the intercalation (see Figure 2.5) of only one Li-ion for every six carbon atoms, LiC6 and thus a resulting reversible equivalent capacity of 372 mAh g^{-1}.

Furthermore, the lithium-ion diffusion rate into disordered carbon layers is between 10^{-12} and $10^{-6}cm^2s^{-1}$ compared with graphite which is between 10^{-9} and 10^{-7} cm^2 s^{-1}, therefore resulting in batteries with low power density (Dambournet *et al.*, 2009; Kaskhedikar & Maier, 2009).

Recently, there is a demand for replacing graphite material for anodes with materials with better and enhanced capacities features, and power density. Although pure lithium metal has a very high capacity amongst anode materials, C_{Li} =3860 mAh g^{-1}, safety concerns restricts the continuity to use pure lithium metal as anode material in rechargeable batteries, knowing that the formation of dendrites (Figure 2.6) over lithium metal leads to a short circuit between cathode and anode (Liu, 2013; Orsini *et al.*, 1999; Pham *et al.*, 2013).

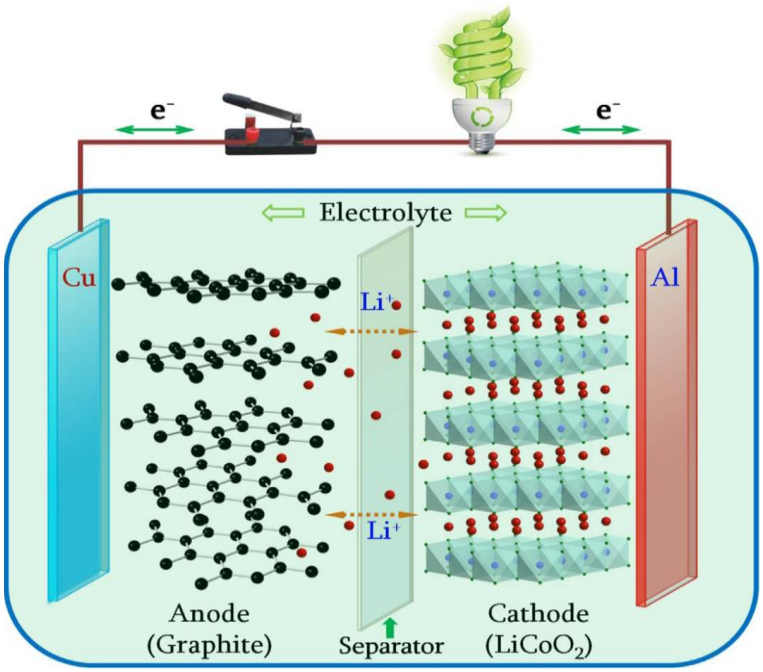

Figure 2. 5: Modified schematic illustration of a lithium-ion battery during the charging/discharging process. The right-hand side shows the layered structure of Li1-xCoO2 material, and the left side represents the anode as graphite sheets. During charging, the lithium-ion migrate from the cathode (positive electrode) to the anode

(negative electrode). lithium-ion migrate the opposite direction during the discharging process (Aurbach et al., 2000; Lin et al., 2015; Nishimura et al., 2008).

Therefore, the path leading to LIBs with improved energy and power density has a major challenge, the selection of suitable anode materials which can provide high capacity and ease diffusion of Li-ions into the anode, along with good cycling life and free from safety concerns (see Figure 2).

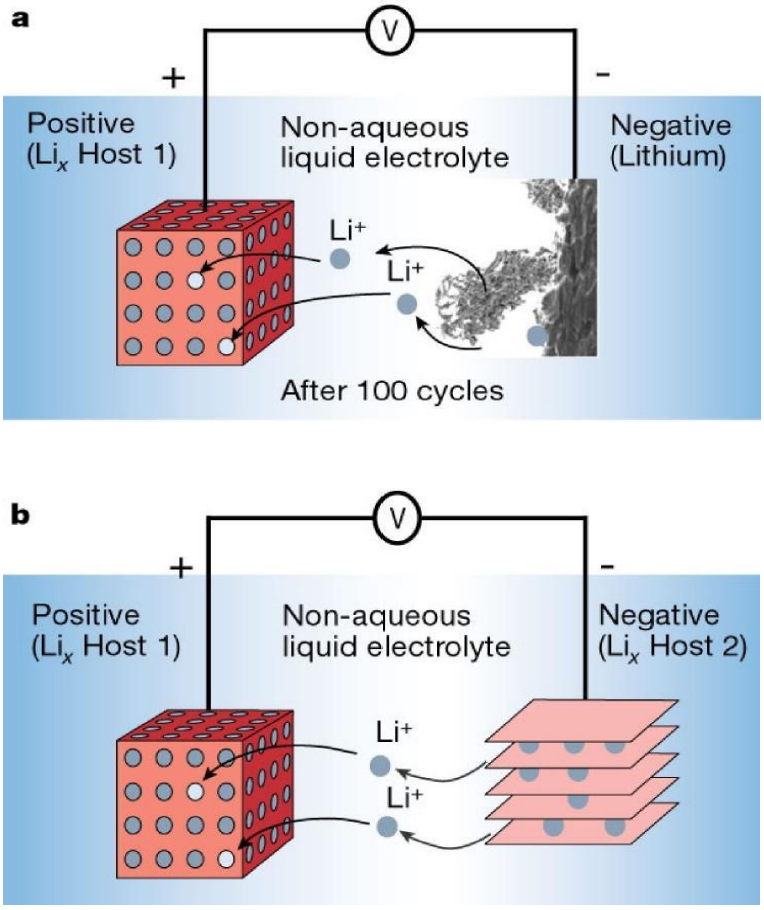

Figure 2. 6: Image representing Li dendritic growth (a). displays a real secondary electron image of such a structure as grown in a cell (b) displays the Li dendritic growth was avoided when different material than lithium metal is used as an electrode. (JM Tarascon 2001)

2.3.1 Cathode Materials

The cathode acts as a lithium host during the discharge process, collecting lithium ions migrated from the other electrode, i.e. the anode through the electrolyte. Good cathode material, on one hand, has to be stable enough to host the lithium ions without reacting with them to the level where the material structure changes permanently or distorted (i.e. good reversible material) but, on the other hand, not very stable to the level it reduces the chance of lithium ions acceptance leading to irreversible process, as the case in primary batteries. Intensive research on the intercalation materials proves that they are most suitable materials for this purpose because lithium ions can host themselves inside the material vacancies without a significant change in the structural features (i.e. the intercalation process is a reversible process. It can be easily attained by applying nearly the same voltage on the opposite side which practically used for the intercalation).

In 1991, the Lithium cobalt oxide, LiCoO2 as a cathode material was the first lithium-ion battery commercialised by Sony as mentioned above. Apart from the very high cost of the cobalt element as well as it's known hazardous and safety concerns, Lithium cobalt oxide was the best choice at that the time. intensive research conducted leading to the discovery of new types of LCO can be used as alternative cathode materials, with the addition of Mn, Al, and Ni to form new improved cathode materials (Goodenough & Kim, 2009; Goodenough & Park, 2013; Wang *et al.*, 2012). Materials such as lithium nickel cobalt aluminium oxide (NCA) and lithium manganese cobalt oxide (NMC) have enhanced the thermal stability of the structure layers of cathode materials, despite the remaining obstacles with cobalt which is part of the structure (Aoshima *et al.*, 2001).

Many research of iron-based materials for cathodes has been started, as Fe is low in cost because of its abundance in nature. The research introduced a type of materials having a very strong system reasonable potential it was the lithium iron phosphate (LiFePO4, LFP) was found to fulfil many requirements (Stamps *et al.*, 2016; Yi *et al.*, 2012).

$LiFePO_4$ was widely studied since then, influenced by the investigation work of Goodenough et al, because of its low cost and the high cathode materials performance in for lithium ion batteries. Moreover, it is described as environmentally friendly (Padhi *et al.*, 1997). The discharge voltage of $LiFePO_4$ is measured to be approximately 3.45 V *vs.* (Li/Li^+) (Huang *et al.*, 2001), and its theoretical capacity is about 170 mAh/g(Huang *et al.*, 2001; Yang *et al.*, 2003a). therefore, $LiFePO_4$ as a cathode material has the gravimetric energy density of approx. 586 Wh/kg, which is not much higher than lithium cobalt oxide, $LiCoO_2$ (Gibot *et al.*, 2008; Yang *et al.*, 2003a). However, the electrochemical features of this material weren't the best in the beginning, but substantial research work has been conducted in order to enhance such property. The electronic conductivity of the pure $LiFePO_4$ is significantly very low. (Gibot *et al.*, 2008) recorded it to be about 10^{-9} S/cm which is extremely low. Carbon coating in latter studies by Goodenough and others show that this can substantially increase its electronic conductivity (Armand *et al.*, 2003) if the particle size is small enough and narrowing the size distribution. Because its volumetric energy density is somewhat less than lithium cobalt oxide, $LiCoO_2$ (~ 2100 Wh/l), as well as its reasonable cost, long life cycle, and environmentally friendly, all these features make it a perfect candidate for the new type cathode (Yoshio *et al.*, 2009).

Lithium -manganese oxide, LiMn2O4, is an interesting example here as a very early candidate for cathode materials, in the LIB time line research. In the beginning, it was described as a promising cathode material, but manganese dissolution as an inherent problem found to be impossible to be resolved. This was thought to be because of the "average oxidation states~" (Mn+III→Mn+II+Mn+IV) (Chung *et al.*, 2002; Yang *et al.*, 2003a). Lately, and on the way to study the possibilities to overcome the dissolution problem, a new cathode material was derived from the same material called lithium manganese-nickel oxide, $LiMn_{1.5}Ni_{0.5}O_2$ (LMNO). this material illustrated very promising features starting from increasing the potential of intercalation to be ~ 4.7V instead of ~ 4.0V for LMO material. This high potential, made LMNO material to be the first high potential material in the history of cathode materials (Delacourt *et al.*, 2006).

lately, research shows that Orthosilicates Li_2MSiO_4 (M= Mn, Co, Fe) materials are promising as a new group of 'polyoxyanion' cathodes for lithium-ion batteries. They deliver two Li ions for every formula unit in the reversible potential, i.e. extraction and incertion of Li ions during the discharge/chage processes, corresponding to about 330mAh/g theoritical capacity which is significantly high. This capacity is two times more than the olivine $LiMPO_4$ (M= Mn, Fe, Ni, Co) type materials (Delacourt *et al.*, 2006; Dominko, 2008).

Li2FeSiO4 is the most promising material amongst orthorhombic Li2MSiO4, because of the abundant and the significant low cost of both, silicon and iron elements. However, there is a major drawback related to the intrinsic low electronic conductivity of Si (silicate, in general). The electronic conductivity for Li2FeSiO4 calculated to be 6 × 10−14 $S.cm^{-1}$. (Dominko, 2008; Nytén *et al.*, 2005).

Figure 2.7 shows the electrochemical behaviour of Li2FeSiO4 material at C/16 rate. The corresponding specific capacity is found to be 165 mAh/g with the capability of removing 1Li+/ Li2FeSiO4. The capacity was then reduced to140 mAh/g after few cycles. The reason according to (Armstrong *et al.*, 2011), and during cycling, some coexisting impurity phases with the material produce side reactions lowering the potential from above 3V for initial charge profiles to about 2.9V. (Armstrong *et al.*, 2011; Chen, 2013; Nytén *et al.*, 2006).

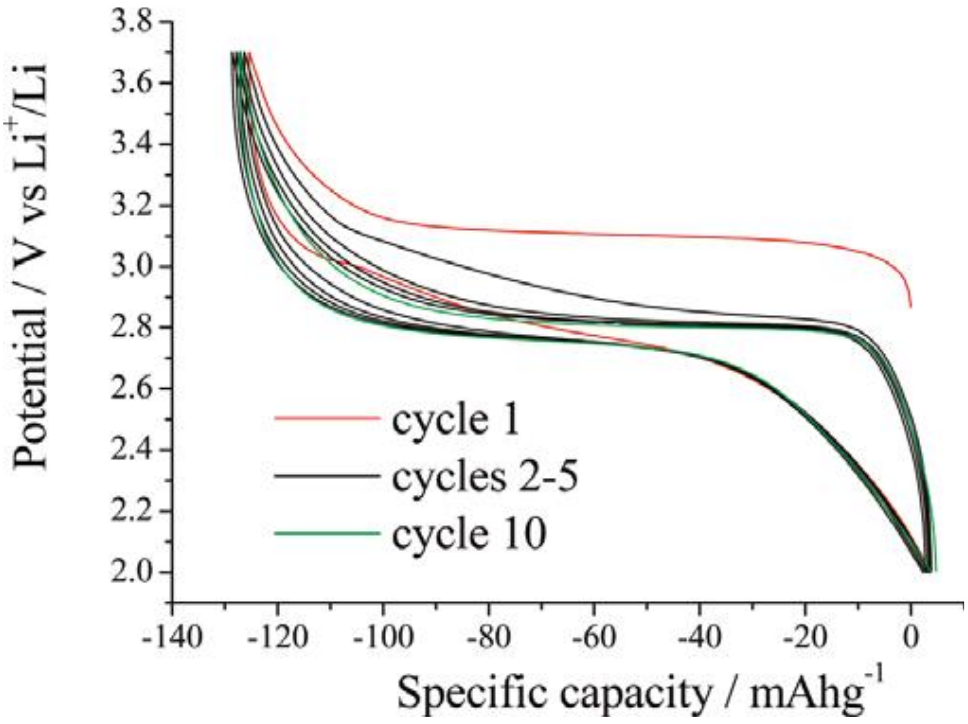

Figure 2. 7:Potential vs. Li^+/Li state of charge on cycling Li2FeSiO4 material at a current rate of 10 mA/g (C/16) (Armstrong et al., 2011; Chen, 2013). Copyright 2011 American Chemical Society

2.3.2 Anode materials

The negative electrode in a primary cell represents the battery anode and is always related to the oxidation i.e. the movement of electrons across the external circuit. The case is different in the rechargeable battery, where the anode works as the positive electrode during the charging process and alters its pole to be a negative electrode during discharge. The latest case applies for the lithium-ion battery anode.

Pure lithium metal was known to be used as the anode in the lithium-ion batteries at the beginning of batteries development, which then proved to be dangerous. During the battery recharging and with using lithium metal as an anode, lithium ions tend to move through the shortest route from the cathode to the anode, and over time, dendrites start to built-up until it grow-over the cathode eventually causing a battery short and in the worst scenario case leading to battery explosion resulting from thermal escapee. Remarkable research efforts were made to overcome safety hazardous, and many alternative materials have thoroughly been investigated. These materials can be concluded to three categories: intercalation materials, conversion materials, and alloying materials. (Palacin, 2009; Tarascon & Armand, 2001).

2.3.2.1 Intercalation materials

The main idea of intercalation is to locate Li ions in the interstitial vacancies within a hosting matrix of the material so that the general structure of the materials stays the same without any significant changes. i.e. no covalent bonds breakdown or forming during the reversible insertion/extraction of Li ions inside the structure. In 1991, Graphite, as a layered intercalation material, was one of the first ever anode intercalation material used in the commorcialised lithium-ion batteries by Sony. Therefore, the risk of the formation of dendrite was tremendously reduced. The intercalation in graphite usually takes place at a

potential value of 0.125V versus Li+/Li, which is a significant low voltage loss compared to the pure lithium metal. lithium titanate, ($Li_4Ti_5O_{12}$, LTO) material with a high potential of 1.55 V has been investigated as an alternative to graphite with a specific capacity of 176 mAh/g. This capacity is very low compared to the specific capacity of graphite, C= 372 mAh/g. (Ferg *et al.*, 1994; Li *et al.*, 2009; Xu *et al.*, 2012). Another challenge is the cost and the abundance of lithium titanate compared to graphite. The specific capacity, the availability, and the low cost of graphite made it a dominant and a better choice and more appealing than for lithium titanate in the lithium-ion batteries market as a promising intercalation anode material. (Ferg *et al.*, 1994; Li *et al.*, 2009; Li *et al.*, 2012).

The ratio of lithium ions to the material is relatively low in the case of intercalation materials, which results' in a relatively low specific capacity compared to the alloying and conversion anode materials.

2.3.2.2 Alloying materials

The second possible alternative materials for anodes in the lithium-ion batteries are the elements that can form an alloy with lithium such as silicon, Si. (Palacin, 2009). One of the most important properties of alloying materials is they are showing a noticeable high specific capacity compare to intercalation materials such as graphite. Tin, silicon, aluminium, and manganese are the most studied elements for alloying materials for anodes. Silicon, Si, is intensively investigated due to its low cost and its high capacity of 3600 mAh/g compared to only 375mAh/g for graphite. (Ji et al., 2011) However, having some intrinsic issues with alloying materials limits the ambition to be the ideal alternative for anode materials. Taking silicon as an example, during the battery operation, approximately, 300% of the volume change of the material takes place caused by the chemical changes. This has proven to negatively affect the structural reliability of the LIB battery, which eventually, cause lost in the electronic contact due to mechanical exhaustion. The continuous electrolyte degradation is another problem caused by the large change of the material volume. (Ji et al., 2011; Reddy et al., 2013; Yazami).

2.3.2.3 Conversion materials

The most important property of the conversion electrodes is their significant high specific capacity compared with graphite an intercalation anode material. The exchange reaction is generalised by the following equation (Cabana *et al.*, 2010; Nitta & Yushin, 2014; Palacin, 2009):

$$Li + M_aX_b \leftrightarrow aM + bLi_nX \quad (2.3)$$

Where M is a transition metal (Fe, Co, Mn, etc.), while X is an anion, electronegative element (O, P, S, etc., commonly O in the case of anodes). M in special cases can be extended to be an alloying metal such as the intermetallic elements (Group IV)

Examples of conversion materials are oxides, such as Iron oxides and cobalt oxide which have been under investigation. (Larcher *et al.*, 2002). They benefit from a high capacity compared to graphite and they are abundant which make them be the best option. On the other hand, they suffer from the large volume changes as well and electrolyte decomposition. They have the lowest kinetic-energy of all the three families of anode materials. The initial lithiation, a step most often differs from the later cycles because of the kinetics. Whereas, delithiation usually results in a metal oxide phase with better kinetics. (Chadwick *et al.*, 2007)

Nitrides are another example of conversion materials, yet, few studies have been conducted on them. They are interesting materials such as LiN which is known to be a lithium ion conductor, and this is true for all elements in GroupV. (Bresser *et al.*, 2016).

The third type of conversion materials is Phosphides and phosphorus. Phosphorus as a Group V element can benefit from the enhanced Li conductivity and being in period three allows it to be in the solid state at room temperature due to its multiple valencies and its atomic number. (Pralong *et al.*, 2002). It has been suggested that phosphide plays a vital role in redox reactions. It is found that the major peaks of lithiation for P element take place

potential window of 0.6-0.9 V and = 0.1 V. whilst, it is between 1.0-1.2 V for the major de-lithiation peaks. (Park & Sohn, 2007) (León *et al.*, 2006)

Tin-based materials as advanced anode materials for lithium-ion batteries are another type of conversion materials as well. The pure tin element has a theoretical capacity of about 994 mAh/g (Kamali & Fray, 2011), which is almost triple the theoretical capacity of graphite anode (C= 375 mAh/g). Tin- based anodes tend to have a bit higher potential than graphite anodes. This reduces the potential safety risks during lithiation/delithiation process. However, the large volume change is still an issue during the lithiation/delithiation process. Whittingham group reported that the pure tin foil can be cycled between 10-15 cycles giving a capacity of 600 mAh/g, which is near twice the capacity of graphite anodes. (Yang *et al.*, 2003b)

In general, comprehensive efforts have been conducted in the exploration of different types of materials to get high capacity anode in LIBs. For example: Carbone-based materials such as: graphite (375 mAh/g), NCT (1100 mAh/g) (De las Casas & Li, 2012), carbon nanofibers(450 mAh/g) (Gentili *et al.*, 2012), graphene (960 mAh g^{-1}) (Liu *et al.*, 2011), porous carbon (800-1100 mAh/g) (Xu *et al.*, 2013), SiO (1600 mAh/g) (Park *et al.*, 2011), silicon (4200 mAh/g) (Wang *et al.*, 2013)], germanium (1601 mAh/g) (Reddy *et al.*, 2012), tin (995 mAh g^{-1}) (Park *et al.*, 2010), and transition metal oxides (500-1000 mAh/g) (Kasavajjula *et al.*, 2007; Zhang & Braun, 2012; Zhang, 2011). additionally, metal sulphides, phosphides and nitrides (Gu *et al.*, 2012; Park & Sohn, 2007) are promising candidates for anode materials, as they all possess a theoretical capacity above 500 mAh/g.

However, before such materials can be used as efficient anode materials, a number of major obstacles that have to be resolved; e.g. poor electron transport, high volume charges (expansion), high cost, abundance, and capacity-fading, as well as low coulombic efficiency. (Abu-Lebdeh & Davidson, 2013; Goriparti *et al.*, 2014; Teki *et al.*, 2009)

2.2.4 The Electrolyte

The electrolyte functions as a catalyst inside the LIBs to make it conductive by endorsing the lithium ions travelling from anode to cathode during discharge and vice versa on the charging process on the one hand. On the other hand, it has to be electronically insulating to restrict electrons movement from one electrode to the other during the charge-discharge process only through an external circuit but not through the electrolyte itself. It consists of soluble lithium salts, acids or bases in liquid, polymer, dry, or gelled formats. The liquid electrolyte is usually flammable, organic not aqueous type. It consists of lithium salts mixed with two or more organic solvents such as ethylene carbonate. The carbonates insure higher conductivity and widen the temperature range (Li et al., 2016; Ohno, 2005)

In conclusion, the electrolyte in a lithium ion battery has two main purposes. The first task is to make the lithium ions' movement possible between the anode and cathode electrodes during the charge-discharge processes. The second task is to be electrically insulting to prevent electrons from travelling between electrodes through elsewhere but the external circuit. Practically, this occurs by dissolving a lithium salt such as lithium hexafluoroarsenate monohydrate ($LiAsF_6$), or lithium hexafluorophosphate ($LiPF_6$), in a mixture of organic carbonates such as ethylene carbonate, dimethyl carbonate or diethyl carbonate. It is common that during charging, electrolyte decomposition takes place resulting in the built up of a layer on the negative electrode which influences the cell performance in general. This layer is commonly called the solid electrolyte interface (SEI).(Balbuena & Wang, 2004). Creating an SEI with desirable properties such as excellent stability and favourable ionic conductivity is possible by choosing the right mixture of organic solvents. (Fong *et al.*, 1990)

Despite that the electrolyte has to be stable, this is not the case with Li-ion though. A passivation film starts to be created immediately covering the anode called the solid electrolyte interface (SEI). This layer isolates the cathode from the anode but permits Li-ions to pass through the separator. In fact, the SEI layer must frame in order for the battery to work. It stabilizes the system. and ensures the Li-ion a longer life.

However, this leads to capacity reduction. On the other side of the battery (the cathode), electrolyte oxidation occurs as well that permanently reduces the capacity (Li & Dahn, 1995).

The first commercially introduced rechargeable battery was at the beginning of 1990 by the Sony Corporation commercially. Since then, non-aqueous solutions commercial lithium-ion batteries are mostly used, in which Lithium hexafluorophosphate (LiPF6) salt or other Li salt, dissolved in a mixture of organic carbonates. Specifically, mixtures of ethylene carbonate (EC) with dimethyl carbonate (DMC), propylene carbonate (PC), diethyl carbonate (DEC), and/or ethyl methyl carbonate (EMC) (Xu, 2004). Example of lithium salts, such as lithium hexafluorophosphate (LiPF6), lithium hexafluoroarsenate monohydrate (LiAsF6), lithium perchlorate (LiClO4) or lithium tetrafluoroborate (LiBF4) which can be dissolved in the carrier fluid (organic carbonates solution mixture), which can subsequently be used in cell construction. In Table 2.1, some examples of these electrolytes and their conductivities are listed.

Type of electrolyte material	Conductivity
Lithium(Trifluoromethylsulfone)-imide (LiTFSI)	9.21 mS/cm at 25°C in y-Butyr-olactone (BL)
Lithium Hexafluoroarsenate Monohydrate (LiAsF6)	10.48 mS/cm at 25°C in y-Bu-tyrolactone (BL)
Lithium Hexafluorophosphate (LiPF6)	11.63 mS/cm at 25°C in y-Bu-tyrolactone (BL)

Table 2. 3: Common electrolyte salts used in lithium-ion cells and their corresponding conductivities. (Robinson & Stokes, 2002)

As pure lithium metal is well known to be highly reactive. It vigorously reacts with water forming lithium-hydroxide. The above-listed electrolytes are all non-aqueous and are typically active, and to get rid of the moisture issues in the battery pack, a sealed container

must be used. Nevertheless, a number of aqueous electrolytes have also been discovered and been used in lithium-ion batteries (Ein-Eli *et al.*, 1994; Li *et al.*, 19

2.3 The Use of Metal Tantalite as Lithium Ion Storage Material, MTaO3 (M= Li, Na, K)

The three M-tantalate perovskites are not traditionally associated with any of lithium-ion battery's electrodes, neither cathode nor anode. They are well known for their excellent properties in electronic, piezoelectric, pyroelectric, and optical devices. Lithium tantalite, LiTaO3 is well known as an optical waveguide (Kip, 1998; Åhlfeldt, 1994). Sodium tantalate is known for its electronic and optical properties (Ece Eyi & Cabuk, 2010), for its photocatalytic properties (Li & Zang, 2009), and for its ferroelectric properties (Kamba *et al.*, 2012). The last material, potassium tantalate, KTaO3 is well known for its photocatalytic properties (Liu *et al.*, 2007) as well as its dielectric (Axelsson *et al.*, 2009) and optical properties (Michel-Calendini & Castet, 1976). However, at the time of this thesis writing, I am unaware of any existing work done on electrochemically characterising and using such materials as Lithium-ion storage, which was one of the main goals of our project.

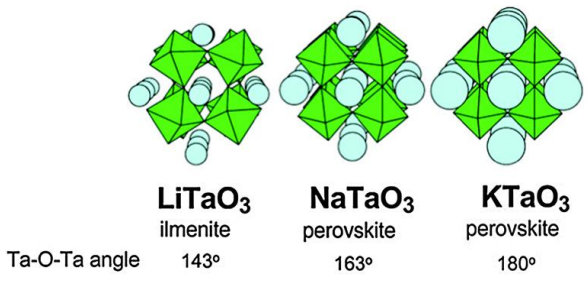

Figure 2. 8: Crystal structures of alkali metal tantalates: $LiTaO_3$, $NaTaO_3$, $KTaO_3$

References

Abu-Lebdeh, Y. & Davidson, I. (2013) Nanotechnology for lithium-ion batteries. [online] New York: Springer.

Åhlfeldt, H. (1994) Nonlinear optical properties of proton-exchanged waveguides in z-cut LiTaO3. Journal of applied physics, 76 (6): 3255-3260.

Aoshima, T., Okahara, K., Kiyohara, C. & Shizuka, K. (2001) Mechanisms of manganese spinels dissolution and capacity fade at high temperature. *Journal of Power Sources*, 97 377-380.

Armand, M., Goodenough, J. B., Padhi, A. K., Nanjundaswamy, K. S. & Masquelier, C. (2003) Cathode materials for secondary (rechargeable) lithium batteries.

Armand, M. & Tarascon, J.-M. (2008) Building better batteries. *Nature*, 451 (7179): 652-657.

Armstrong, A. R., Kuganathan, N., Islam, M. S. & Bruce, P. G. (2011) Structure and lithium transport pathways in Li2FeSiO4 cathodes for lithium batteries. *Journal of the American Chemical Society*, 133 (33): 13031-13035.

Aurbach, D., Lu, Z., Schechter, A., Gofer, Y., Gizbar, H., Turgeman, R., Cohen, Y., Moshkovich, M. & Levi, E. (2000) Prototype systems for rechargeable magnesium batteries. *Nature*, 407 (6805): 724-727.

Axelsson, A. K., Pan, Y., Valant, M. & Alford, N. (2009) Synthesis, sintering, and microwave dielectric properties of KTaO3 ceramics. *Journal of the American Ceramic Society*, 92 (8): 1773-1778.

Balakrishnan, P., Ramesh, R. & Kumar, T. P. (2006) Safety mechanisms in lithium-ion batteries. *Journal of Power Sources*, 155 (2): 401-414.

Balbuena, P. B. & Wang, Y. (2004) *Lithium-ion batteries: solid-electrolyte interphase*. World Scientific.

Basu, S., Zeller, C., Flanders, P., Fuerst, C., Johnson, W. & Fischer, J. (1979) Synthesis and properties of lithium-graphite intercalation compounds. *Materials Science and Engineering*, 38 (3): 275-283.

Besenhard, J. & Fritz, H. (1974) Cathodic reduction of graphite in organic solutions of alkali and NR4+ salts. *Journal of Electroanalytical Chemistry and Interfacial Electrochemistry*, 53 (2): 329-333.

Besenhard, J. & Schöllhorn, R. (1977) Chromium oxides as cathodes for secondary high energy density lithium batteries. *Journal of The Electrochemical Society*, 124 (7): 968-971.

Bresser, D., Passerini, S. & Scrosati, B. (2016) Leveraging valuable synergies by combining alloying and conversion for lithium-ion anodes. *Energy & Environmental Science*, 9 (11): 3348-3367.

Brousse, T., Retoux, R., Herterich, U. & Schleich, D. (1998) Thin-Film Crystalline SnO_2-Lithium Electrodes. *Journal of The Electrochemical Society*, 145 (1): 1-4.

Cabana, J., Monconduit, L., Larcher, D. & Palacin, M. R. (2010) Beyond Intercalation-Based Li-Ion Batteries: The State of the Art and Challenges of Electrode Materials Reacting Through Conversion Reactions. *Advanced Materials*, 22 (35):

Chadwick, A. V., Savin, S. L., Fiddy, S., Alcantara, R., Fernández Lisbona, D., Lavela, P., Ortiz, G. F. & Tirado, J. L. (2007) Formation and oxidation of nanosized metal particles by electrochemical reaction of Li and Na with NiCo2O4: X-ray absorption spectroscopic study. *The Journal of Physical Chemistry C*, 111 (12): 4636-4642.

Chan, C. K., Peng, H., Liu, G., McIlwrath, K., Zhang, X. F., Huggins, R. A. & Cui, Y. (2008) High-performance lithium battery anodes using silicon nanowires. *Nature nanotechnology*, 3 (1): 31-35.

Chen, C., Liu, J., Stoll, M., Henriksen, G., Vissers, D. & Amine, K. (2004) Aluminum-doped lithium nickel cobalt oxide electrodes for high-power lithium-ion batteries. *Journal of Power Sources*, 128 (2): 278-285.

Chen, H., Qiu, X., Zhu, W. & Hagenmuller, P. (2002) Synthesis and high rate properties of nanoparticled lithium cobalt oxides as the cathode material for lithium-ion battery. *Electrochemistry communications*, 4 (6): 488-491.

Chen, J. (2013) Recent progress in advanced materials for lithium ion batteries. *Materials*, 6 (1): 156-183.

Chen, J. & Whittingham, M. S. (2006) Hydrothermal synthesis of lithium iron phosphate. *Electrochemistry Communications*, 8 (5): 855-858.

Chung, S.-Y., Bloking, J. T. & Chiang, Y.-M. (2002) Electronically conductive phospho-olivines as lithium storage electrodes. *Nature materials*, 1 (2): 123-128.

Dambournet, D., Belharouak, I. & Amine, K. (2009) Tailored preparation methods of TiO2 anatase, rutile, brookite: mechanism of formation and electrochemical properties. *Chemistry of materials*, 22 (3): 1173-1179.

De las Casas, C. & Li, W. (2012) A review of application of carbon nanotubes for lithium ion battery anode material. *Journal of Power Sources*, 208 74-85.

Delacourt, C., Poizot, P., Levasseur, S. & Masquelier, C. (2006) Size effects on carbon-free LiFePO4 powders the key to superior energy density. *Electrochemical and Solid-State Letters*, 9 (7): A352-A355.

Dominko, R. (2008) Li_2MSiO_4 (M= Fe and/or Mn) cathode materials. *Journal of Power Sources*, 184 (2): 462-468.

Ece Eyi, E. & Cabuk, S. (2010) Ab initio study of the structural, electronic and optical properties of NaTaO3. *Philosophical Magazine*, 90 (21): 2965-2976.

Ein-Eli, Y., Markovsky, B., Aurbach, D., Carmeli, Y., Yamin, H. & Luski, S. (1994) The dependence of the performance of Li-C intercalation anodes for Li-ion secondary batteries on the electrolyte solution composition. *Electrochimica Acta*, 39 (17): 2559-2569.

Fauteux, D. & Koksbang, R. (1993) Rechargeable lithium battery anodes: alternatives to metallic lithium. *Journal of applied electrochemistry*, 23 (1): 1-10.

Ferg, E., Gummow, R., De Kock, A. & Thackeray, M. (1994) Spinel anodes for lithium-ion batteries. *Journal of the Electrochemical Society*, 141 (11): L147-L150.

Fong, R., Von Sacken, U. & Dahn, J. R. (1990) Studies of lithium intercalation into carbons using nonaqueous electrochemical cells. *Journal of The Electrochemical Society*, 137 (7): 2009-2013.

Franco, A. (2015) Rechargeable lithium batteries: from fundamentals to applications. Elsevier.

Gentili, V., Brutti, S., Hardwick, L., Armstrong, A., Panero, S. & Bruce, P. (2012) Lithium insertion into anatase nanotubes. *Chemistry of Materials*, 24 (22): 4468-4476.

Gibot, P., Casas-Cabanas, M., Laffont, L., Levasseur, S., Carlach, P., Hamelet, S., Tarascon, J.-M. & Masquelier, C. (2008) Room-temperature single-phase Li insertion/extraction in nanoscale Li_xFePO_4. *Nature Materials*, 7 (9): 741-747.

Goodenough, J. B. & Kim, Y. (2009) Challenges for rechargeable Li batteries. *Chemistry of materials*, 22 (3): 587-603.

Goodenough, J. B. & Park, K.-S. (2013) The Li-ion rechargeable battery: a perspective. *Journal of the American Chemical Society*, 135 (4): 1167-1176.

Goriparti, S., Miele, E., De Angelis, F., Di Fabrizio, E., Proietti Zaccaria, R. & Capiglia, C. (2014) Review on recent progress of nanostructured anode materials for Li-ion batteries. *Journal of Power Sources*, 257 (Supplement C): 421-443.

Gu, J., Collins, S. M., Carim, A. I., Hao, X., Bartlett, B. M. & Maldonado, S. (2012) Template-Free Preparation of Crystalline Ge Nanowire Film Electrodes via an Electrochemical Liquid–Liquid–Solid Process in Water at Ambient Pressure and Temperature for Energy Storage. *Nano Letters*, 12 (9): 4617-4623.

Huang, H., Yin, S.-C. & Nazar, L. s. (2001) Approaching theoretical capacity of LiFePO4 at room temperature at high rates. *Electrochemical and Solid-State Letters*, 4 (10): A170-A172.

Ji, L., Lin, Z., Alcoutlabi, M. & Zhang, X. (2011) Recent developments in nanostructured anode materials for rechargeable lithium-ion batteries. *Energy & Environmental Science*, 4 (8): 2682-2699.

Johnson, C., Li, N., Vaughey, J., Hackney, S. & Thackeray, M. (2005) Lithium–manganese oxide electrodes with layered–spinel composite structures xLi 2 MnO 3·(1− x) Li $_{1+y}$ Mn $_{2-y}$ O 4 (0< x< 1, 0⩽ y⩽ 0.33) for lithium batteries. *Electrochemistry Communications*, 7 (5): 528-536.

Kamali, A. R. & Fray, D. J. (2011) Tin-based materials as advanced anode materials for lithium ion batteries: a review. *Rev. Adv. Mater. Sci*, 27 (1): 14-24.

Kamba, S., Goian, V., Bovtun, V., Nuzhnyy, D., Kempa, M., Spreitzer, M., König, J. & Suvorov, D. (2012) Incipient Ferroelectric Properties of $NaTaO_3$. *Ferroelectrics*, 426 (1): 206-214.

Kasavajjula, U., Wang, C. & Appleby, A. J. (2007) Nano-and bulk-silicon-based insertion anodes for lithium-ion secondary cells. *Journal of Power Sources*, 163 (2): 1003-1039.

Kaskhedikar, N. A. & Maier, J. (2009) Lithium storage in carbon nanostructures. *Advanced Materials*, 21 (25-26): 2664-2680.

Kip, D. (1998) Photorefractive waveguides in oxide crystals: fabrication, properties, and applications. *Applied Physics B: Lasers and Optics*, 67 (2): 131-150.

Kirchhoff, G. & Bunsen, R. (1861) LXIV. Chemical analysis by spectrum-observations. *The London, Edinburgh, and Dublin Philosophical Magazine and Journal of Science*, 22 (150): 498-510.

Larcher, D., Sudant, G., Leriche, J., Chabre, Y. & Tarascon, J. (2002) The Electrochemical Reduction of Co3 O 4 in a Lithium Cell. *Journal of the Electrochemical Society*, 149 (3): A234-A241.

León, B., Corredor, J. I., Tirado, J. L. & Pérez-Vicente, C. (2006) On the mechanism of the electrochemical reaction of tin phosphide with lithium. *Journal of The Electrochemical Society*, 153 (10): A1829-A1834.

Li, H., Wang, Z., Chen, L. & Huang, X. (2009) Research on Advanced Materials for Li-ion Batteries. *Advanced Materials*, 21 (45): 4593-4607.

Li, N., Chen, Z., Ren, W., Li, F. & Cheng, H.-M. (2012) Flexible graphene-based lithium-ion batteries with ultrafast charge and discharge rates. *Proceedings of the National Academy of Sciences*, 109 (43): 17360-17365.

Li, Q., Chen, J., Fan, L., Kong, X. & Lu, Y. (2016) Progress in electrolytes for rechargeable Li-based batteries and beyond. *Green Energy & Environment*, 1 (1): 18-42.

Li, W. & Dahn, J. R. (1995) Lithium-Ion Cells with Aqueous Electrolytes. *Journal of the Electrochemical Society*, 142 (6): 1742-1746.

Li, W., Dahn, J. R. & Wainwright, D. S. (1994) Rechargeable lithium batteries with aqueous electrolytes. *Science-AAAS-Weekly Paper Edition-including Guide to Scientific Information*, 264 (5162): 1115-1117.

Li, X. & Zang, J. (2009) Facile hydrothermal synthesis of sodium tantalate ($NaTaO_3$) nanocubes and high photocatalytic properties. *The Journal of Physical Chemistry C*, 113 (45): 19411-19418.

Lin, M.-C., Gong, M., Lu, B., Wu, Y., Wang, D.-Y., Guan, M., Angell, M., Chen, C., Yang, J. & Hwang, B.-J. (2015) An ultrafast rechargeable aluminium-ion battery. *Nature*, 520 (7547): 324-328.

Liu, H., Bi, Z., Sun, X. G., Unocic, R. R., Paranthaman, M. P., Dai, S. & Brown, G. M. (2011) Mesoporous TiO2–B microspheres with superior rate performance for lithium ion batteries. *Advanced Materials*, 23 (30): 3450-3454.

Liu, J. (2013) Addressing the grand challenges in energy storage. *Advanced Functional Materials*, 23 (8): 924-928.

Liu, J., Chen, G., Li, Z. & Zhang, Z. (2007) Hydrothermal synthesis and photocatalytic properties of ATaO3 and ANbO3 (A= Na and K). *International Journal of Hydrogen Energy*, 32 (13): 2269-2272.

Marom, R., Amalraj, S. F., Leifer, N., Jacob, D. & Aurbach, D. (2011) A review of advanced and practical lithium battery materials. *Journal of Materials Chemistry*, 21 (27): 9938-9954.

Michel-Calendini, F. & Castet, L. (1976) Band structure, optical and transport properties of $KTaO_3$, $KNbO_3$ and $BaTiO_3$ in the paraelectric phase. *Ferroelectrics*, 13 (1): 367-370.

Mikolajczak, C. (2011) Lithium-ion batteries hazard and use assessment. [online] New York: Springer.

Miller, P. (2015) Automotive Lithium-Ion Batteries. *Johnson Matthey Technology Review*, 59 (1): 4-13.

Mizushima, K., Jones, P., Wiseman, P. & Goodenough, J. (1981) Li_xCoO_2 ($0< x\leqslant 1$): A new cathode material for batteries of high energy density. *Solid State Ionics*, 3 171-174.

Nishimura, S.-i., Hayase, S., Kanno, R., Yashima, M., Nakayama, N. & Yamada, A. (2008) Structure of Li_2FeSiO_4. *Journal of the American Chemical Society*, 130 (40): 13212-13213.

Nitta, N. & Yushin, G. (2014) High-capacity anode materials for lithium-ion batteries: choice of elements and structures for active particles. *Particle & Particle Systems Characterization*, 31 (3): 317-336.

Nytén, A., Abouimrane, A., Armand, M., Gustafsson, T. & Thomas, J. O. (2005) Electrochemical performance of Li_2FeSiO_4 as a new Li-battery cathode material. *Electrochemistry Communications*, 7 (2): 156-160.

Nytén, A., Kamali, S., Häggström, L., Gustafsson, T. & Thomas, J. O. (2006) The lithium extraction/insertion mechanism in Li_2FeSiO_4. *Journal of Materials Chemistry*, 16 (23): 2266-2272.

Ohno, H. (2005) Electrochemical aspects of ionic liquids. John Wiley & Sons.

Orsini, F., Du Pasquier, A., Beaudouin, B., Tarascon, J., Trentin, M., Langenhuizen, N., De Beer, E. & Notten, P. (1999) In situ SEM study of the interfaces in plastic lithium cells. *Journal of power sources*, 81 918-921.

Padhi, A. K., Nanjundaswamy, K. S. & Goodenough, J. B. (1997) Phospho-olivines as positive-electrode materials for rechargeable lithium batteries. *Journal of the electrochemical society*, 144 (4): 1188-1194.

Palacin, M. R. (2009) Recent advances in rechargeable battery materials: a chemist's perspective. *Chemical Society Reviews*, 38 (9): 2565-2575.

Park, C.-M., Kim, J.-H., Kim, H. & Sohn, H.-J. (2010) Li-alloy based anode materials for Li secondary batteries. *Chemical Society Reviews*, 39 (8): 3115-3141.

Park, C. M. & Sohn, H. J. (2007) Black phosphorus and its composite for lithium rechargeable batteries. *Advanced Materials*, 19 (18): 2465-2468.

Park, S.-J., Kim, Y.-J. & Lee, H. (2011) Synthesis of carbon-coated TiO_2 nanotubes for high-power lithium-ion batteries. *Journal of Power Sources*, 196 (11): 5133-5137.

Pham, V. H., Kim, K.-H., Jung, D.-W., Singh, K., Oh, E.-S. & Chung, J. S. (2013) Liquid phase co-exfoliated MoS_2–graphene composites as anode materials for lithium-ion batteries. *Journal of Power Sources*, 244 280-286.

Poizot, P., Laruelle, S., Grugeon, S., Dupont, L. & Tarascon, J. (2000) Nano-sized transition-metal oxides as negative-electrode materials for lithium-ion batteries. *Nature*, 407 (6803): 496-499.

Prakash, A., Manikandan, P., Ramesha, K., Sathiya, M., Tarascon, J. & Shukla, A. (2010) Solution-combustion synthesized nanocrystalline $Li_4Ti_5O_{12}$ as high-rate performance Li-ion battery anode. *Chemistry of Materials*, 22 (9): 2857-2863.

Pralong, V., Souza, D., Leung, K. & Nazar, L. (2002) Reversible lithium uptake by CoP 3 at low potential: role of the anion. *Electrochemistry Communications*, 4 (6): 516-520.

Reddy, A. L. M., Gowda, S. R., Shaijumon, M. M. & Ajayan, P. M. (2012) Hybrid nanostructures for energy storage applications. *Advanced materials*, 24 (37): 5045-5064.

Reddy, M., Subba Rao, G. & Chowdari, B. (2013) Metal oxides and oxysalts as anode materials for Li-ion batteries. *Chemical reviews*, 113 (7): 5364-5457.

Robinson, R. A. & Stokes, R. H. (2002) *Electrolyte solutions*. Courier Corporation.

Schöllhorn, R., Kümpers, M. & Besenhard, J. (1977) Topotactic redox reactions of the channel type chalcogenides Mo 3 S 4 and Mo 3 Se 4. *Materials Research Bulletin*, 12 (8): 781-788.

Scott, I. D., Jung, Y. S., Cavanagh, A. S., Yan, Y., Dillon, A. C., George, S. M. & Lee, S.-H. (2010) Ultrathin coatings on nano-LiCoO2 for Li-ion vehicular applications. *Nano letters*, 11 (2): 414-418.

Scrosati, B. & Garche, J. (2010) Lithium batteries: Status, prospects and future. *Journal of Power Sources*, 195 (9): 2419-2430.

Small, D., Farley, B. D. & McKeefery, W. J. (2001) Rechargeable battery pack charging system with redundant safety systems.

Stamps, M. A., Eischen, J. W. & Huang, H.-Y. S. (2016) Particle-and crack-size dependency of lithium-ion battery materials LiFePO4. *AIMS Mater. Sci*, 3 (1): 190.

Stavins, R. N., Wagner, A. F. & Wagner, G. (2003) Interpreting sustainability in economic terms: dynamic efficiency plus intergenerational equity. *Economics Letters*, 79 (3): 339-343.

Tang, Y., Yang, L., Fang, S. & Qiu, Z. (2009) Li 4 Ti 5 O 12 hollow microspheres assembled by nanosheets as an anode material for high-rate lithium ion batteries. *Electrochimica Acta*, 54 (26): 6244-6249.

Tarascon, J.-M. & Armand, M. (2001) Issues and challenges facing rechargeable lithium batteries. *Nature*, 414 (6861): 359-367.

Teki, R., Datta, M. K., Krishnan, R., Parker, T. C., Lu, T. M., Kumta, P. N. & Koratkar, N. (2009) Nanostructured silicon anodes for lithium-ion rechargeable batteries. *Small*, 5 (20): 2236-2242.

Wang, H., Liang, Y., Gong, M., Li, Y., Chang, W., Mefford, T., Zhou, J., Wang, J., Regier, T. & Wei, F. (2012) An ultrafast nickel–iron battery from strongly coupled inorganic nanoparticle/nanocarbon hybrid materials. *Nature Communications*, 3 917.

Wang, J., Zhou, Y., Xiong, B., Zhao, Y., Huang, X. & Shao, Z. (2013) Fast lithium-ion insertion of TiO 2 nanotube and graphene composites. *Electrochimica Acta*, 88 847-857.

Wang, Q., Li, H., Chen, L. & Huang, X. (2001) Monodispersed hard carbon spherules with uniform nanopores. *Carbon*, 39 (14): 2211-2214.

Warner, J. T. (2015) The Handbook of Lithium-Ion Battery Pack Design: Chemistry, Components, Types and Terminology. Elsevier.

Whittingham, M. S. (1976) Electrical energy storage and intercalation chemistry. *Science*, 192 (4244): 1126-1127.

Whittingham, M. S. (2004) Lithium batteries and cathode materials. *Chemical reviews*, 104 (10): 4271-4302.

Xu, B., Qian, D., Wang, Z. & Meng, Y. S. (2012) Recent progress in cathode materials research for advanced lithium-ion batteries. *Materials Science and Engineering: R: Reports*, 73 (5): 51-65.

Xu, G.-L., Wang, Q., Fang, J.-C., Xu, Y.-F., Li, J.-T., Huang, L. & Sun, S.-G. (2014) Tuning the structure and property of nanostructured cathode materials of lithium ion and lithium sulfur batteries. *Journal of Materials Chemistry A*, 2 (47): 19941-19962.

Xu, K. (2004) Nonaqueous liquid electrolytes for lithium-based rechargeable batteries. *Chemical reviews*, 104 (10): 4303-4418.

Xu, W., Wang, Z., Guo, Z., Liu, Y., Zhou, N., Niu, B., Shi, Z. & Zhang, H. (2013) Nanoporous anatase TiO 2/single-wall carbon nanohorns composite as superior anode for lithium-ion batteries. *Journal of Power Sources*, 232 193-198.

Yang, S., Song, Y., Ngala, K., Zavalij, P. Y. & Whittingham, M. S. (2003a) Performance of LiFePO 4 as lithium battery cathode and comparison with manganese and vanadium oxides. *Journal of Power Sources*, 119 239-246.

Yang, S., Zavalij, P. Y. & Whittingham, M. S. (2003b) Anodes for lithium batteries: tin revisited. *Electrochemistry communications*, 5 (7): 587-590.

Yazami, R. Nanomaterials for lithium-ion batteries : fundamentals and applications.

Yazami, R. (1999) Surface chemistry and lithium storage capability of the graphite–lithium electrode. *Electrochimica acta*, 45 (1): 87-97.

Yazami, R. & Touzain, P. (1983) A reversible graphite-lithium negative electrode for electrochemical generators. *Journal of Power Sources*, 9 (3): 365-371.

Yi, T.-F., Li, X.-Y., Liu, H., Shu, J., Zhu, Y.-R. & Zhu, R.-S. (2012)

Recent developments in the doping and surface modification of LiFePO4 as cathode material for power lithium-ion battery. *Ionics*, 18 (6): 529-539.

Yoshino, K., Nakajima, S. & Sugimoto, R.-i. (1987) Fusibility of polythiophene derivatives with substituted long alkyl chain and their properties. *Japanese journal of applied physics*, 26 (6A): L1038.

Yoshio, M., Brodd, R. J. & Kozawa, A. (2009) Lithium-ion batteries : science and technologies. [online] New York, NY: Springer,

Yoshizawa, H. & Ohzuku, T. (2007) An application of lithium cobalt nickel manganese oxide to high-power and high-energy density lithium-ion batteries. *Journal of Power Sources*, 174 (2): 813-817.

Zhang, H. & Braun, P. V. (2012) Three-dimensional metal scaffold supported bicontiuous silicon battery anodes. *Nano letters*, 12 (6): 2778-2783.

Zhang, W.-J. (2011) A review of the electrochemical performance of alloy anodes for lithium-ion batteries. *Journal of Power Sources*, 196 (1): 13-24.

Chapter 3

Methodology and Techniques

3.1 Materials synthesis techniques

A wide range of synthesis methods used in material science research such as chemical vapour deposition, RF plasma method, sol-gel powder synthesis method, and a hydrothermal method, for creating different types of nanomaterials.

The powders under investigation in this project were all of the very small dimensions, i.e. the order of hundreds of nanometers. Here, hydrothermal and sol-gel methods were used to produce fine nanoparticles to be used as active materials in the lithium-ion battery study.

3.1.1 Hydrothermal Synthesis

Recently, preparation of metal oxides using hydrothermal synthesis process has become a favourable choice for many reasons such that no further calcination under high temperatures is required for the final powder, preventing the nano-sized particle from re-clustering, and contamination. Another advantage is that the heating path and the low used temperature in this method prevent the nanomaterial from any phase transition. Furthermore, the resulting powder is highly homogeneous, and it is easy to control the composition, the size and the shape of the crystal, and the purity of the resulting powder. (Kulkarni, 2015; Liu *et al.*, 2007).

In hydrothermal synthesis, crystallisation takes place in an aqueous medium, e.g. ethanol, water, etc., inside a steel bomb called autoclave. Figure 3.1 shows the hydrothermal apparatus used to produce the final product. The synthesis' ideal conditions of the temperature and pressure are usually of the range 80 - 250^{0}C for the temperature resulting to 1- 20bars for the pressure, which can be simply calculated using the ideal gas law (Hadjipanayis & Siegel, 2012):

$$PV = nRT \tag{3.1}$$

The temperature is significantly low compared to the other materials' syntheses methods such as solid state and Sol-gel methods. Two powder materials were produced by the hydrothermal method to serve the investigation purpose of this project. Both sodium tantalate ($NaTaO_3$), and potassium tantalate $KTaO_3$ were produced hydrothermally with nearly ideal crystallisation conditions and a very small size in the order of a few hundreds of nanometres

Figure3. 1: Photo of a stainless-steel autoclave and its Teflon liner

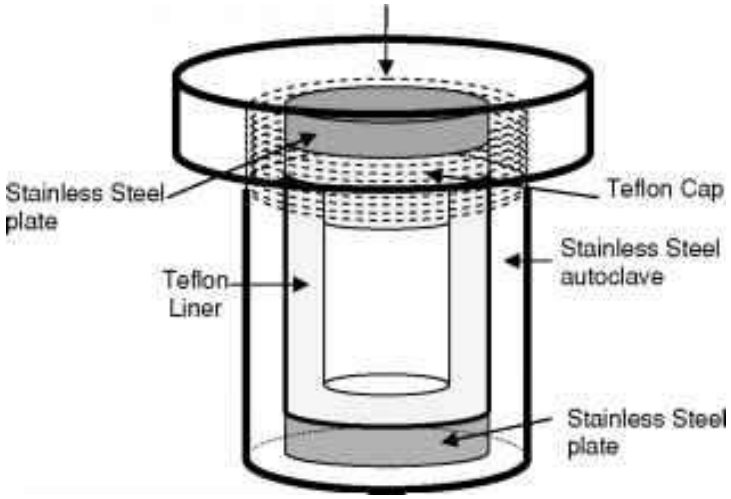

Figure3. 2: Schematic diagram of the stainless-steel autoclave and the Teflon liner. (Liu et al., 2007)

3.1.2 Sol-Gel Synthesis

Sol-gel chemical synthesis is a well-known method since the early nineteenth century, but it was re-discovered the late 1970s for glasses production under low temperatures. Basically, it is a chemical solution-based method used to synthesise glass and ceramics in the form of powders, thin films, or fibres (see Figure 3.3, Figure 3.4).

In this chemical solution-based method, the solution slowly transforms into a gel-like with time, but still containing both solid and liquid phases. At first, a significant quantity of solution possibly will have to be taken away from solution/ mixture until the gel-like start to be created. This can be achieved by applying medium-low heat to assist with the evaporation process. (Talam *et al.*, 2012). In our lithium tantalate sol-gel synthesis, a temperature of ~100^0C mixture for few hours until it reaches the desired thickness.

The advantages of Sol-gel method, its low cost, it is noticeably a low temperatures method, and the chemical composition can be easily controlled. This

technique can be used in ceramics processing and producing thin films of metal oxides. Nanomaterials derived by this method have wide applications in electronics, medicine, separation technology, and optics. (Feinle *et al.*, 2016)

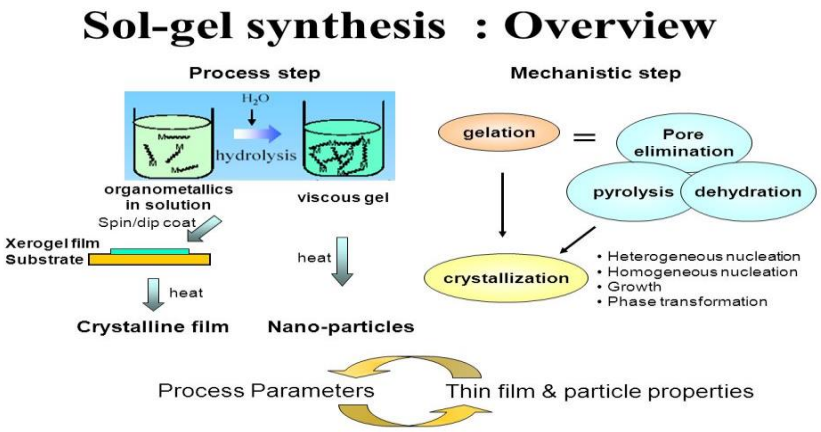

Figure3. 3: Schematic diagram shows an overview synthesis and the possible routes on the synthesising of Nano-particles and crystalline films. (http://slideplayer.com/slide/6848362/23/images/4/Sol-gel+synthesis)

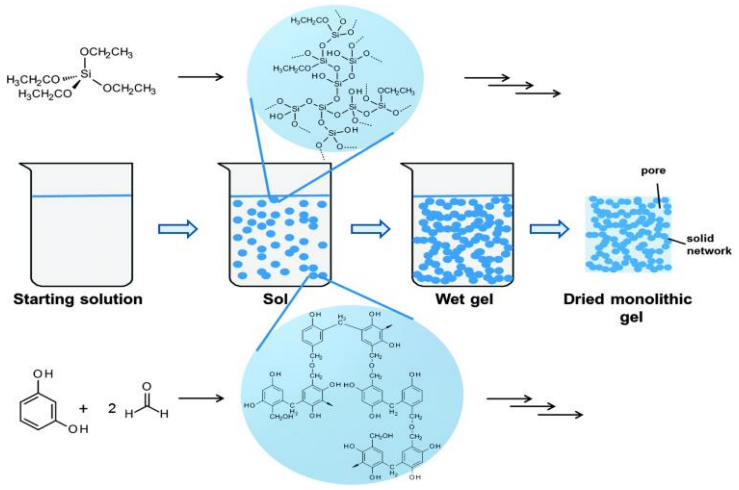

Figure3. 4: Illustration shows a Sol-gel method as condensation-based system formation reactions. (Feinle et al., 2016)

3.1.3 Solid-State Reaction

The most widly used method for the preparation of polycrystalline solids from a mixture of two or more solid reactants under extremely high temperatures compared to the above two methods, often more than 1000- 1500 °C due to the low diffusion in solids. In this work, an unsuccessful attempt was made to obtain a pure phase of potassium tantalate, KTaO3 powder and the result wasn't promising (West, Anthony R, 2014).

The solid state was terminated after the final product found to suffer from multi-phases and all the attempts to produce a single perovskite phase were failed. On the other hand, the hydrothermal method produced a very fine product of pure perovskite phase.

3.2 Materials Characterization and Morphology

3.2.1 X-ray Diffraction

Powder X-ray Diffraction (XRD) is a powerful non-destructive technique for the identification of the bulk structure of nanomaterials such as powder and polycrystalline materials. It provides information on the crystal orientation, material structure, and its different phases, as well as various structural parameters, such as average grain size, strain, and crystal defects. Furthermore, the XRD pattern of any pure substance is unique which makes it a fingerprint of the material. (Borie, 1965; Moore & Reynolds, 1989

Physical Concept

X-rays are electromagnetic radiation used to generate the diffraction pattern due to their short wavelengths λ which is on the range of a few angstroms (1-100 Ångströms), the same order of magnitude as the spacing *d* between planes in crystalline solids. In principle, diffraction occurs as waves interfere with a regular structure whose spacing distance, d and the beam wavelength λ are approximately identical. Ideally, X-ray diffraction based on the *elastic* scattering of generated electromagnetic waves in the form of X-rays from the sample structures. These generated X-rays are known to be the resultant interaction between the incidence of high energy electrons beam with a copper target (8.05 keV, 0.154 nm) (Warren, 1969)

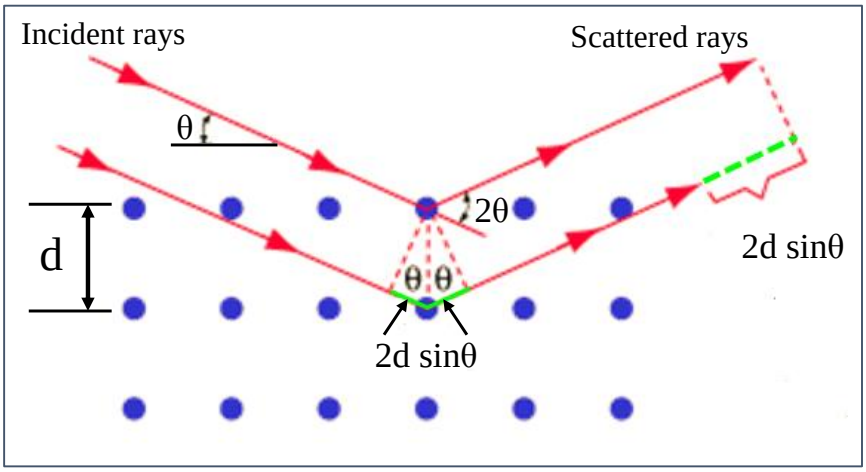

Figure3. 5: diffraction of X-ray beam on crystal planes, Bragg's law.

In 1912, W. L. Bragg was able to identify a simple mathematical relationship between several factors. He assumed that the crystal consists of long arrays of atoms in different equidistant parallel planes. Constructive interference takes place when the incident X-rays beam penetrates the crystalline plane at angle θ (with respect to the crystalline plane normal) and interacts with the internal structure of the solid sample. The constructive interference takes place under two conditions, the angles of incidence and scattering beams are equal; and the path difference between the diffracted beams from two different planes is equal to a multiple n of the beam wavelength λ (Figure 3.5). This results in Bragg's law:

$$n\lambda = 2d \sin\theta, \quad n = 1, 2, \ldots \tag{3.2}$$

where λ is the wavelength of the incident electromagnetic beam, n is an integer indicates the order of reflectance, d is the spacing distance between two atomic planes, and θ is the incident between the incident beam and normal to the reflecting crystalline plane. (Sharma *et al.*, 2012; Warren, 1969)

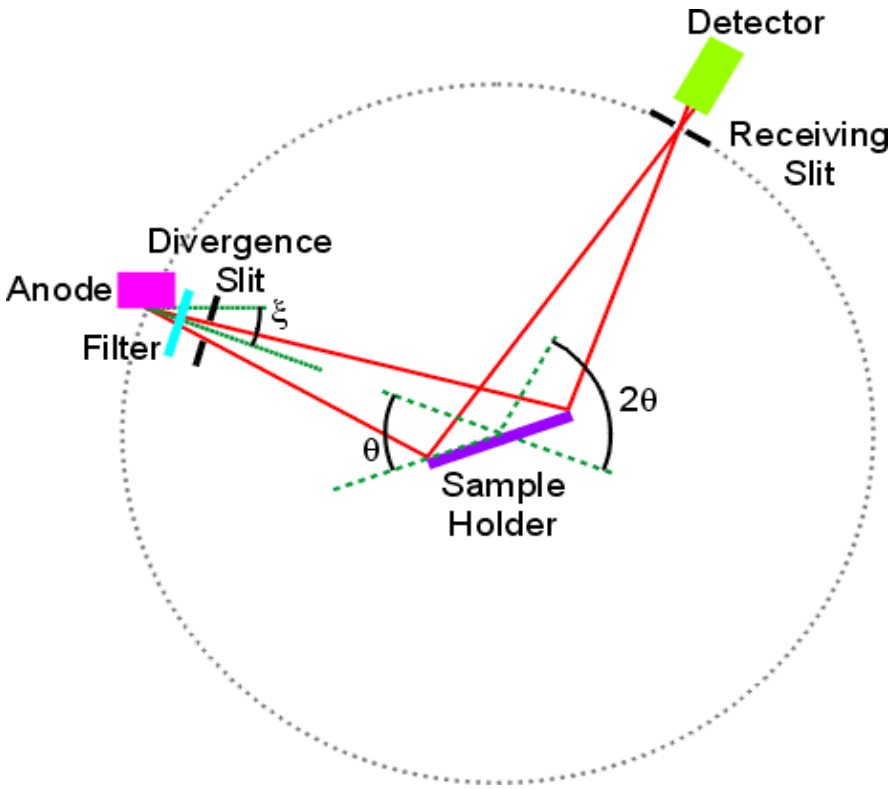

Figure3. 6: Schematic diagram of the essential components of XRD equipment. (Sharma et al., 2012)

.

The detector then collects the interference signals at different angles, θ, which are the lattice spacing, *d* based on Bragg's law. The diagrams in Figure 3.6 simply represents the X-ray diffraction technique. The characteristics of the crystalline sample; such as the atomic composition and the crystal structure can be identified using the lattice spacing, *d*.

For crystallite sizes smaller than1 μm, crystallite sizes and strains can be calculated using the Scherrer equation (Borie, 1965; Guinier, 1994):

$$D = K\lambda(\beta\cos\Theta)^{-1} \tag{3.3}$$

where *D* is the mean size of the particle of the nanoparticle, *K* the shape factor (~1), λ corresponds to the wavelength of the electromagnetic X-ray beam, and β *is* the peak broadening at full width at half maximum intensity. This derivation is based on the assumption of a Gaussian shape profile.

In this work, the structure of three powder samples was investigated using powder X-Ray diffraction technique; $NaTaO_3$ powder, $LiTaO_3$ powder, and $KTaO_3$ powder. The X-ray measurements were carried out using a Panalytical X-Pert Pro MPD powder diffractometer at the X-ray diffraction facility. (Figure 3.7).

Figure 3.6 shows a Schematic diagram of the setup for a θ-2θ measurement XRD equipment. The electromagnetic waves of X-rays are generated using a tube anode of a Cu source operating at 45 kV high voltage and 40 mA current. A monochromatic filter is used to improve the angular resolution of the measurement. As a result, only Cu $K_{\alpha 1}$ radiation was selected and used to characterise the powders in the 2θ range of 10^o to 70^o with a step size of 0.01^o and counting time of 0.2s per step.

Figure3. 7: The Panalytical X-Pert Pro MPD powder diffractometer at X-ray Diffraction facility. (physics department, University of Warwick).

3.2.2 Scanning electron microscopy (SEM)

The main tool in our project is Scanning electron microscopy (SEM) SEM is a microscopy method which uses electrons as probes to form a 3D image of the sample. Yet it is one of the most powerful and productive techniques of microscopy. Scanning the electron microscope since it was first invented in early 1950, have established new zones of study in the physical and medical science communities. The advantages of SEM technique over traditional microscopes, the fact that its field has a large depth which allows much more of a sample to be in focus at one time. It has allowed researchers to test a wider variety of specimens. Additionally, its higher resolution over the remaining microscopes

gave it another bonus, as this allows a higher magnification of the closely placed specimens.

SEM user has more control over the magnification degree as well; this is because it uses electromagnets rather than tradition optical lenses. All these advantages, as well as the actual amazingly focused images, have made the scanning electron microscope one of the most powerful instruments in the research community. It is being proven that scanning electron microscope has become a valuable instrument in evaluating different types of materials; the metallic, non-metallic, surfaces, and assemblies as well. (Bozzola & Russell, 1999). Moreover, it is a nondestructive tool in a way that sample can be extracted and reduced as such after scanning process, e.g. powder types materials.

Equipment Setup

The below SEM setup diagram shown in Figure3.8 can be divided into three different stages.

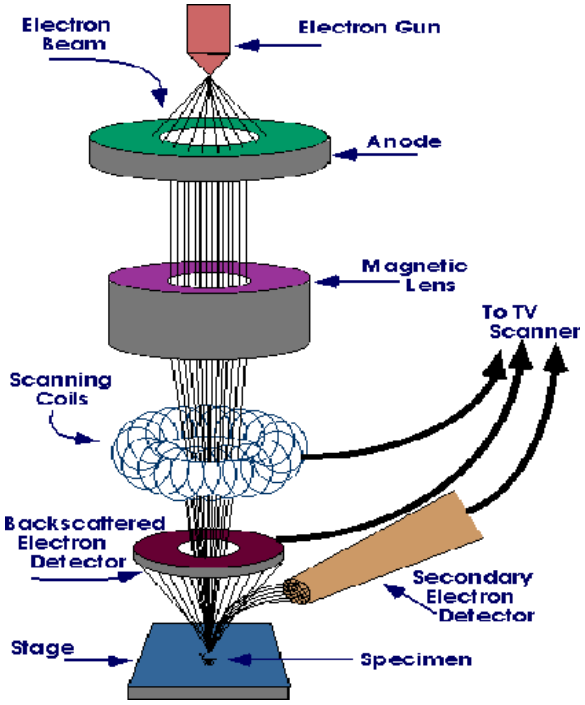

Figure3. 8: A schematic diagram of a scanning electron microscope (SEM).

The first stage is the electron gun: as shown in the diagram (Figure 3.8), the electron source is seated on the top of the tool column. In general, there are three different types of electron sources known to be used as electron sources in electron microscopes. The simplest type is the tungsten filament, which is composed of a one bent tungsten wire. The tip starts to emit electrons thermionically once a strong voltage is applied to the tungsten source. The electrons beam can then be controlled in further stages. (Avadhanulu, 1992) (Avadhanulu, 1992).

The second type of emitter uses the lanthanum hexaboride LaB_6 filament (De Harven *et al.*, 1984). It consists of tiny, single lanthanum hexaboride crystal; set on a sharp tip. Similarly, the tip of the crystal emits thermionic radiation of electrons; if a high potential is applied to the source. In spite, the emission process of the tip in this type is similar to that in the first type; which uses tungsten instead, but the use of lanthanum hexaboride crystal produces electron beam much brighter than the electron beam emitted from the first type

using tungsten filament. According to (Zhang *et al.*, 2005), the brightness is double or higher from the tungsten filament. However, the required conditions for LaB6 based source are of higher demanding compared to the tungsten-based source.

The last type of electron source to be discussed here is the cold field emission gun (Crewe *et al.*, 1971). Likewise, the first type source; it is made up of very sharp tip of tungsten wire with a diameter of 100nm or less (Otten & Coene, 1993). This allows electrons emission via tunnelling to occur instantly when applied electric field targets the tip, without the need of pre-heating current. Schottky type is another type of field emission guns (Tuggle & Swanson, 1985) as well. A coated tungsten wire with some materials to improve the electrons' thermionic emission; e.g. zirconium oxide is used as a source in this type (Pawley, 1997), which as a consequence improves the electric conductivity under high temperatures.

In the second stage of the electron microscope, the emitted electron beam then moves through the next microscope stage; the electromagnetic condenser lens system. The main function of these type of lenses is to form the primary beam. The electron beam first passes through these lenses set up. This system of lenses is usually made of electromagnetic quadrupole and hexapole lenses (Mispelter *et al.*, 1972) or (Kohl & Reimer, 2008). The beam condensation takes place

The third stage of the electron microscope is the scanning stage: in this stage, the electron beam tailored by the electromagnetic lenses is then shifted by applying an electric field, in a way that showers the area of interest. The electron bean can then can be then focused on the desired area of the specimen using an electromagnetic lens as well.

Specimen Scan and Image Formation

Two main types of electron scattering result when the electron beam hits the surface and penetrates the specimen, elastic and inelastic. As a result of the penetration, the produced volume of interaction is usually shaped in a water drop-like shape as illustrated in Figure 3.9.

Various factors stand behind the exact size and shape of the volume interaction, such as the incident angle between the incident electron beam and the specimen surface, the initial energy of the incident beam, the nature of the specimen material and its topology, and the energy loss through both; elastic and inelastic interactions

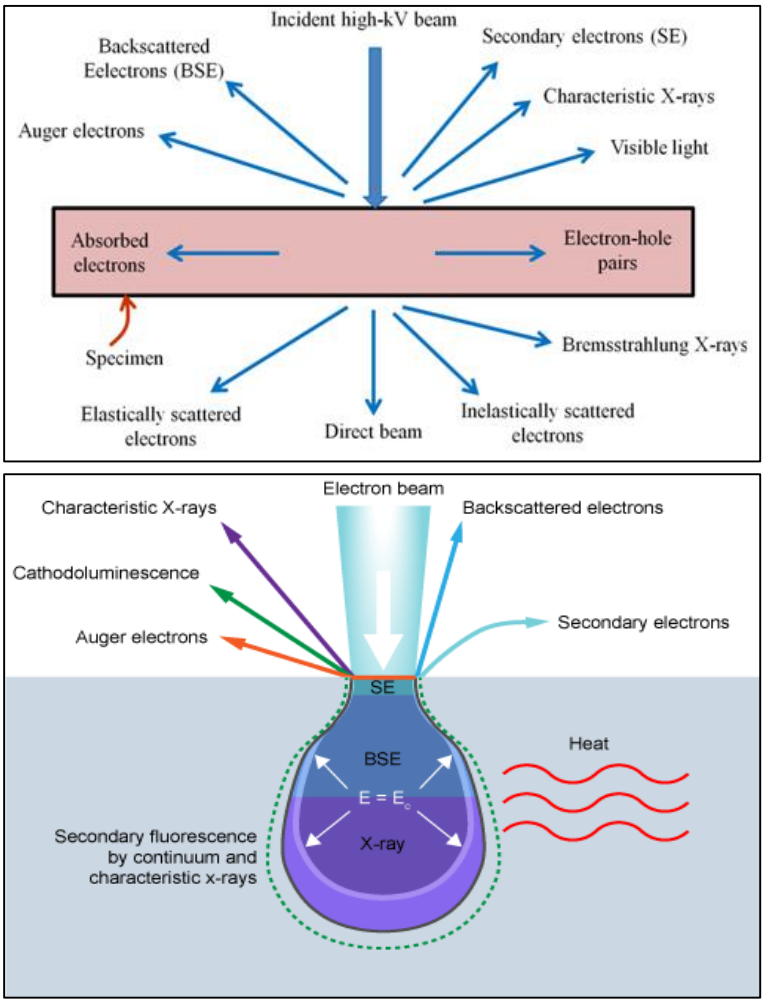

Figure3. 9: Illustrated diagram, up the outcomes of the interaction of the electron beam with the sample. Down: the interaction volume as encountered by SEM and the regions of the various detected signals. (Biswas, 2016; Microscopy, 2013).

3.3 Transmission electron microscopy (TEM)

is a microscopy technique where an electron beam is transmitted through a very thin specimen. An image is formed from the interaction of the electrons transmitted through the specimen. The electrons interact with the material in two ways: inelastic and elastic scattering. Inelastic scattering- which leading eventually to absorption- must be avoided since it contains no significant information. The electron beam then will be only elastically scattered (diffracted). The image is then magnified onto an imaging device, such as a fluorescent screen, or to be detected by a sensor such as CCD camera. This process provides a basis for studying the structure of crystals and of identifying materials.

The electron beam will be diffracted by the crystalline specimen through very specific directions given in angles, θ. These directions are not just an electon wavelength dependent but crystal lattice spacing as well, according to Bragg's law:

$$n\lambda = 2\mathrm{d}\sin\theta,$$

where n is ian nteger, λ is electron wavelength, d is crystal lattice spacing between atomic planes, θ is athe ngle of incidence and also of reflection.

Usually, TEM consists of three stages of lensing: the condenser lenses, the objective lenses, and the projector lenses. The condenser lenses are necessary for primary beam formation, while the objective lenses focus the beam that comes through the sample itself. The projector lenses are used to expand the beam onto the phosphor screen. The magnification of the TEM is due to the ratio of the distances between the specimen and the objective lens' image plane. The magnification of objective lens is determined by the ratio of the distances between its object plane (the specimen) and its image plane, Figure 3.10 shows a schematic diagram of TEM (C. Meyer *et al*, 2008)

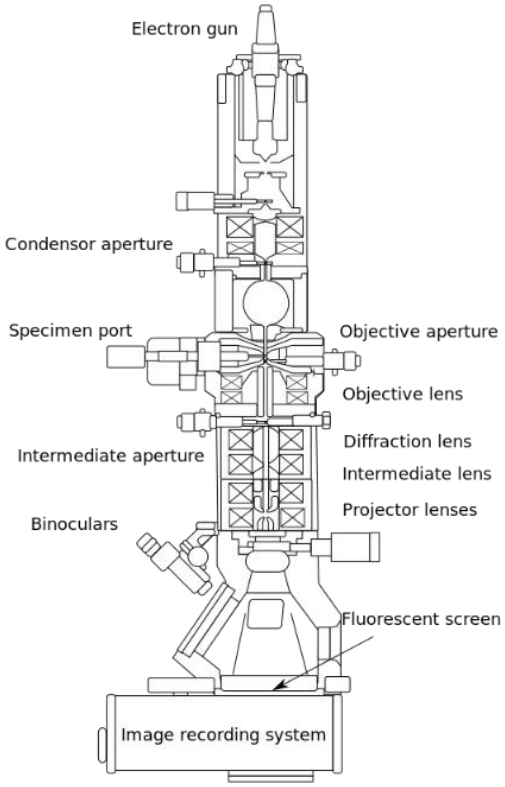

Figure3. 10: Schematic diagram of TEM

3.4 Electrochemical Testing

At the cell level, the assessment of lithium-ion battery materials is essential to evaluate the capability of an electrochemical pair; a cathode and the anode electrodes for practical use. Important data can be obtained such as; discharge capacity and potential profile and the discharge capacity at different rates, i.e. rate capability, internal resistance, i.e. impedance, cycle life and safety. This project has investigated three different materials as Li-ion anodes at the half-cell level.

Two types of half-cells were fabricated at the dry room in the WMG labs; coin cells (CR2032) and the two electrodes Swagelok cells. In our work, galvanostatic cycling, i.e. C-rate, cyclic voltammetry tests and the impedance spectroscopy were evaluated for the chosen half-cells. Our fabricated electrodes for the use of such tests were fabricated to contain AM:CB:PVdF mass ratio of 8:1:1.

3.3.1 Rate capability Test

Charge/discharge test is a useful test for examining the electrochemical performance of the Li-ion electrodes. Essentially, it tests the amount of the stored charge within the cell electrode under certain conditions with respect to increasing cycle numbers. One way of controlling charge/discharge experiments is by setting a potentiostatic step, holding the voltage at a constant value allowing the current to decrease until it reaches a certain limit. On the other hand, in Galvanostatic setup, the potential varies with time at constant current. The current density i_m, is usually denoted by mA/g (where the mass is relative to the active material amount inside the electrode). The term "C-rate" is often used to identify the charge/discharge current which is calculated from the battery capacity, i.e. the discharge current relative to its capacity. 1C-rate. Refers to the current at which the battery will be fully discharged in one hour.

However, the discharge capacity (Q_p) time can be easily calculated using the Peukert's law:

$$t = (Q_p / I^k) \tag{3.4}$$

where I is the drawn current battery in amps., Q_p is the discharge capacity at the rate of 1amp., and t is the time duration - calculated in hours- for the battery to sustain, and k called Peuker number and is closer to unity for lithium-ion batteries.

In general, battery capacity refers to the amount of the charge the battery capable to store in certain conditions. The practical capacity of a battery can be measured by

discharging it when it is fully-charged at a constant current rate through a load. The practical capacity can be found and calculated from the potential vs. discharging capacity graph.

On the other hand, the theoretical specific capacity of an electrode, Q_{charge}; measured in mAh g^{-1} indicates number of reactive charges and the weight of the active material of that electrode, i.e. is the amount of charges (electricity) involved in the battery electrochemical reaction for various battery systems. Theoretical capacity can be calculated using the following formula (Bard *et al.*, 1980; Liu *et al.*, 2016):

$$C_{theo.} = nF/3.6x\ M \tag{3.5}$$

where n is the number of transferred electrons/mole of the reaction, M is the mass of the active material, and F is Faraday's constant.

The capacity and the rate capability of the electrodes were investigated in the Energy Innovation Centre (EIC) labs; by Galvanostatic discharge/charge tests at a constant current density mode (10 µA/g) using a battery test device (BT-Cell-Tester) with a computer (PC) and software BT-Lab 1.5v. for our Cell-Testers operate in the voltage range of 1V - 3V, with a maximum current of 10µA.

The capacity and cycling performance of the materials were investigated by Galvanostatic charge/discharge tests using constant current density mode.

3.3.2 Cyclic voltammetry

Cyclic voltammetry (CV) is a popularly used technique to investigate the kinetics of electron transfer and the thermodynamic behaviour during the electrochemical reaction in the working electrode. Cyclic voltammetry (CV) is very similar to the linear sweep voltammetry (LSV). However, in the case of CV, the potential of the working electrode is set to ramp linearly between two set values as a function of time; at a fixed potential rate

(mV/s). The difference is when the potential reaches its maximum value (V2), the scan is inverted, and the potential sweeps back to the minimum value (V1).

Figure 3.11 shows a typical cyclic voltammogram recorded for a reversible single electrode transfer reaction.

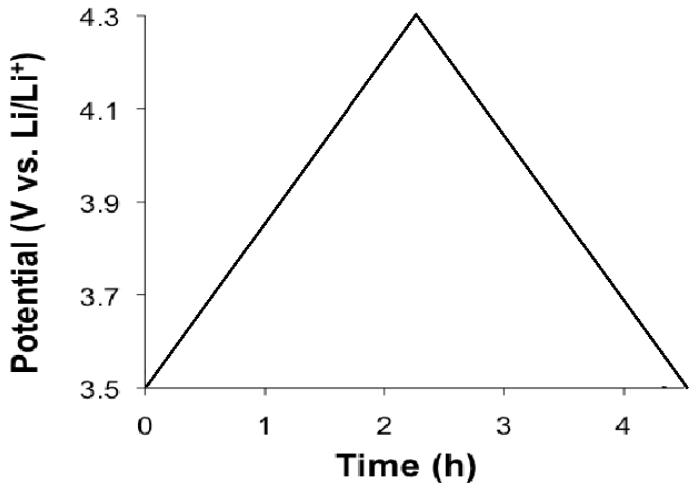

Figure3. 11: Linear sweep at a rate of 0.1 mV/s in the range of 3.5 - 4.3 V vs. Li/Li+.

In a redox reaction, the oxidation/reduction peaks appear in pairs when potential is swept in different directions. The change of voltage vs. time is represented by the "scan rate". The peak current (i_n) and the scan rate relationship follows the Randles-Sevcik equation (at T= 25^0C):

$$i_n = (0.4463)nFAC(nF\nu D/RT)^{1/2} \quad (3.6)$$

where i_n is maximum current, n is the number of transferred electrons in the re-dox reaction (usually 1), A is electrode's area, F is Faraday's Constant, D is the diffusion coefficient, C is the concentration, ν is the scan rate in V/s, R is gas constant, T is temperature in K.

Furthermore, the cell potential, E can be calculated using Nernst's Equation (Jiang & Zhang; Yoshio *et al.*, 2009)

$$E = E^{0'} - RT\, nF \ln(Q) \tag{3.7}$$

E^0 is the formal electrode potential, R is ideal gas constant , T is the temperature, *n* is number of moles, F: Faraday's constant, Q is the Reaction quotient, E^0 is direct measurable reading from the cyclic voltammetry graph.

In this work, a BT-Lab electrochemical workstation was used to collect the CV data. In fact, this value can be estimated as the average value between the point of maximum and the minimum currents:

$$E^{0'} = (E_{max} - E_{min})/ 2 \tag{3.8}$$

The term 'terminal potential' here refers to the potential difference between the terminals of the battery when the load is applied to it. Whereas the open-circuit-voltage, V_{oc} is the voltage between the battery terminals without applied load.

3.3.3 Electrode fabrication

The electrodes were fabricated by dispersing a mixture of 80wt% active materials, 10 wt% carbon black (conductive agent) and 10wt% polyvinylidene difluoride (PVDF, a binder, dissolved by the ratio of 8w% in N-methyl-2-pyrrolidinone, NMP solvent) to obtain the desired slurry. The slurry then was spread onto a sheet of copper foil using a Doctor blade, and the thickness of the spread slurry was approximately 20 microns in thickness.

The electrode was then kept drying at ~120°C for about 2-3 hours, then transferred to the vacuum furnace and set to dry under vacuum for no less than 24 hours. Finally, the

electrode sheet was transferred to the dry room where it was punched into discs of ~13-16mm in diameter, and area of ~1cm^2 depending on the type of the test cell. The weight and the thickness of each electrode were recorded and the weight of the active material of each electrode was calculated as 80% of the weight difference of the Cu sheet after and before the paste application. The electrodes were then ready for the next step; to be used in the half-cell assembly

Half-Cells Construction

Two configurations of test cells were fabricated; the two electrode Swagelok cells (see Figure 3.12), and the CR 2032 standard coin cells. Figure 3.13, shows how the coin cells were assembled in our work.

The test half-cells were assembled in the dry room (WMG lab, University of Warwick, UK), in which moisture and oxygen were automatically controlled to satisfy the cells' fabrication conditions. Lithium metal discs of ~16mm in diameter were used as a standard counter electrode in both types of test cells to examine the electrochemical properties of the prepared electrodes of the three materials. 60 µL of the electrolyte was used in this work per cell assembly. The electrolyte consists of $LiPF_6$ salt dissolved in a 20:20:60 volume per cent (v/o) mixture solvent of EC (ethylene carbonate), PC (propylene carbonate), and DEC (diethyl carbonate), -2 spacers per test cell (for coin cell assembly), and Celgard 2500 microporous plastic film was used as a separator.

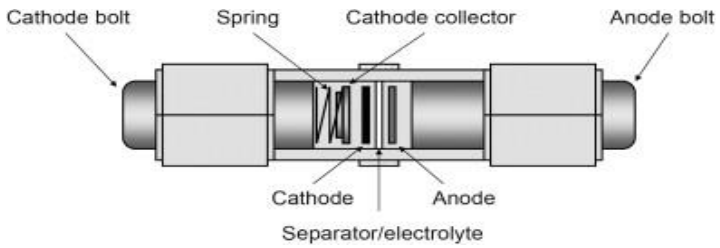

Figure3. 12: A diagram represents the two electrode Swagelok test cell. (Canas et al., 2013)

Coin Cell Assembly Procedure

Figure 3.12 shows the right method in order to assemble a coin cell. First, the anode; which is the fabricated active materials electrode in our project, is cantered inside the positive casing (the base), and 60 µL drops of the electrolyte were placed on the electrode disc, after that, the separator was carefully placed over the wet electrode. Electrolyte plays a vital role in the in which it enhances the Li ions transfer between the working and counter electrodes. Lack of electrolyte reduces the chance of adequate transfer of lithium-ions and as a result; increases of the coin cell's internal resistance and decreases the efficiency. A gasket must be used to lock the separator on the top of the electrode to prevent the contact between the lithium metal and the counter electrode. Lithium metal disc was then placed on the top of the separator, and 1-2 spacers to prevent any misalign of any of the coin cell components, A spring is placed above the spacer and the top of the coin cell is eventually closed by the negative case; ready to be crimped. After all the components were correctly aligned, the cell was crimped under ~1500 psi using a hydraulic crimping machine the cell is then thoroughly cleaned from the excess electrolyte and the potential, Voc then measured. Ideally, a good fabricated cell measures from 3-4V.

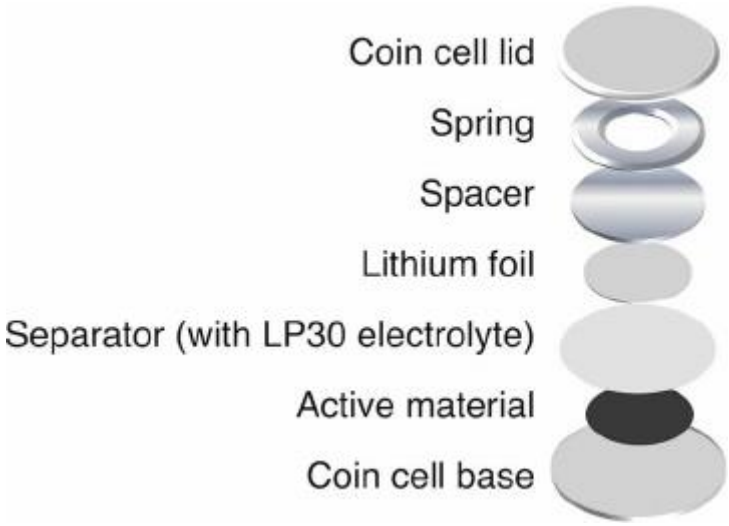

Figure3. 13: Components of coin cell. (Solarajan et al., 2016)

References

A.R. West "Solid State Chemistry and its Applications" Chapter 2 – Preparative Methods

Anon Sol-gel Synthesis sketch. Available from: http://slideplayer.com/slide/6848362/23/images/4/Sol-gel+synthesis+:+Overview.jpg

Avadhanulu, M. (1992) A textbook of engineering physics. S. Chand Publishing.

Bard, A. J., Faulkner, L. R., Leddy, J. & Zoski, C. G. (1980) Electrochemical methods: fundamentals and applications. wiley New York.

Biswas, K. (2016) Advanced Characterization Techniques.

Borie, B. (1965) X-Ray Diffraction in Crystals, Imperfect Crystals, and Amorphous Bodies. Journal of the American Chemical Society, 87 (1): 140-141.

Borie, B. (1965) X-Ray Diffraction in Crystals, Imperfect Crystals, and Amorphous Bodies. Journal of the American Chemical Society, 87 (1): 140-141.

Bozzola, J. J. & Russell, L. D. (1999) Electron microscopy: principles and techniques for biologists. Jones & Bartlett Learning.

Canas, N. A., Hirose, K., Pascucci, B., Wagner, N., Friedrich, K. A. & Hiesgen, R. (2013) Investigations of lithium–sulfur batteries using electrochemical impedance spectroscopy. Electrochimica Acta, 97 42-51.

Crewe, A., Isaacson, M. & Johnson, D. (1971) A high resolution electron spectrometer for use in transmission scanning electron microscopy. Review of Scientific Instruments, 42 (4): 411-420.

De Harven, E., Leung, R. & Christensen, H. (1984) A novel approach for scanning electron microscopy of colloidal gold-labeled cell surfaces. The Journal of cell biology, 99 (1): 53-57.

Feinle, A., Elsaesser, M. S. & Huesing, N. (2016) Sol–gel synthesis of monolithic materials with hierarchical porosity. Chemical Society Reviews, 45 (12): 3377-3399.

Guinier, A. (1994) X-ray diffraction in crystals, imperfect crystals, and amorphous bodies. Courier Corporation.

Hadjipanayis, G. C. & Siegel, R. W. (2012) Nanophase materials: Synthesis-properties-applications. Springer Science & Business Media.

Hemavibool, s. (2007) the microstructure of synthetic aggregate produced from waste materials and its influence on the properties of concrete by.

Jiang, J. & Zhang, C. Fundamentals and applications of lithium-ion batteries in electric drive vehicles. [online] Available from: http://0-onlinelibrary.wiley.com.pugwash.lib.warwick.ac.uk/book/10.1002/9781118414798

Kohl, H. & Reimer, L. (2008) Transmission electron microscopy: physics of image formation. Springer.

Kulkarni, S. K. (2015) Synthesis of Nanomaterials—I (Physical Methods). In: Nanotechnology: Principles and Practices. Cham: Springer International Publishing: 55-76.

Liu, C., Neale, Z. G. & Cao, G. (2016) Understanding electrochemical potentials of cathode materials in rechargeable batteries. Materials Today, 19 (2): 109-123.

Liu, J., Chen, G., Li, Z. & Zhang, Z. (2007) Hydrothermal synthesis and photocatalytic properties of ATaO3 and ANbO3 (A= Na and K). International Journal of Hydrogen Energy, 32 (13): 2269-2272.

Meyer, Jannik C.; Girit, C. O.; Crommie, M. F.; Zettl, A., Nature (Berkeley) 454(2008)319.

Microscopy, A. (2013) Microanalysis Research Facility. MyScope: training for advance research,

Mispelter, J., Grivet, J.-P., Baiwir, M. & Lhoste, J.-M. (1972) Electron spin resonance of phosphorescent fluorine-substituted aromatics: III. Derivatives of biphenyl and of o, o'-bridged bipheyls in dibenzofuran single crystal and in frozen ethanol. Molecular Physics, 24 (1): 205-213.

Moore, D. M. & Reynolds, R. C. (1989) X-ray Diffraction and the Identification and Analysis of Clay Minerals. Oxford university press Oxford.

Otten, M. T. & Coene, W. M. (1993) High-resolution imaging on a field emission TEM. Ultramicroscopy, 48 (1-2): 77-91.

Pawley, J. (1997) The development of field-emission scanning electron microscopy for imaging biological surfaces. Scanning-New York And Baden Baden Then Mahwah-, 19 324-336.

Sharma, R., Bisen, D., Shukla, U. & Sharma, B. (2012) X-ray diffraction: a powerful method of characterizing nanomaterials. Recent Research in Science and Technology, 4 (8):

Solarajan, A. K., Murugadoss, V. & Angaiah, S. (2016) Montmorillonite embedded electrospun PVdF–HFP nanocomposite membrane electrolyte for Li-ion capacitors. Applied Materials Today, 5 33-40.

Talam, S., Karumuri, S. R. & Gunnam, N. (2012) Synthesis, characterization, and spectroscopic properties of ZnO nanoparticles. ISRN Nanotechnology, 2012

Tuggle, D. & Swanson, L. (1985) Emission characteristics of the ZrO/W thermal field electron source. Journal of Vacuum Science & Technology B: Microelectronics Processing and Phenomena, 3 (1): 220-223.

Warren, B. E. (1969) X-ray Diffraction. Courier Corporation.

Yoshio, M., Brodd, R. J. & Kozawa, A. (2009) Lithium-ion batteries: science and technologies. [online] New York, NY: Springer, Available from: https://0-link-springer-com.pugwash.lib.warwick.ac.uk/book/10.1007/978-0-387-34445-4

Zhang, M., Fang, S., Zakhidov, A. A., Lee, S. B., Aliev, A. E., Williams, C. D., Atkinson, K. R. & Baughman, R. H. (2005) Strong, transparent, multifunctional, carbon nanotube sheets. Science, 309 (5738): 1215-1219.

Chapter 4

Material Synthesis and Electrochemical Properties of Sodium Tantalate Nanoparticles, $NaTaO_3$

Sodium tantalate, $NaTaO_3$ is one of the perovskites, alkali tantalates ($ATaO_3$, A= alkali metal) powders. Two types of $NaTaO_3$ perovskite structures; orthorhombic, and pseudocubic were first studied by (Kay & Miles, 1957), where they were able to measure their lattice parameters. It is well known for its interesting physical properties such as its reasonable stability, low density, high photocatalytic activity in water splitting process, and high sound velocity, as well as its extensive use for piezoelectric and ferroelectric applications. (Reznitchenko *et al.*, 2001; Saito *et al.*, 2004; Shanker *et al.*, 2009). In this work, and for the first time, the $NaTaO_3$ nanocubes powder was used as an active material electrode in the lithium-ion test cells.

4.1 Material synthesis

Sodium tantalate, $NaTO_3$ nanocubes were synthesised using hydrothermal synthesis method. High purity powder of tantalum pent oxide, and commercially available Ta_2O_5 (Sigma-Aldrich, 99.997% trace metal basis), and different concentrations of sodium hydroxide, NaOH solutions (Analar, Warwick chemistry stores) were used.in this synthesis without further purification.

In a typical synthesis procedure, different concentrations of NaOH solution of 5-1M were first prepared and added along with approx. 2.209 g of Ta_2O_5 powder into a 40mL Teflon-lined stainless steel autoclave up to approximately 80% of the autoclave's total volume. The autoclave was kept at a temperature between 120-140°C for a designated period of time. The autoclave was then kept to cool down to room temperature naturally. The resulting precipitates, $NaTaO_3$ in the form of pure white sediment, were collected and filtered using microporous filter papers and washed several times thoroughly with DI water. It was then allowed to dry under vacuum at 60 °C for about 6 hrs prior to the next step.

Parameter Name	Parameter Value
Mass of Tantalum (V) Oxide	2.209 g
Concentration of Sodium Hydroxide	1M
Volume of the used NaOH Solution	32mL
Dwell temperature	140°C
Temperature Ramp Rate	5°C
Dwell Time	12 hours
Precipitate Colour	Pure White
No. of washing cycles (DI water)	4 cycles
Drying Temperature	60°C
Drying Time	4-8 hours

Table 4. 1: A breakdown of the sample synthesis procedure for a typical synthesis set up.

4.2 Results and Discussion

Throughout the powder tested, we were able to characterise our powder. Powder X-ray diffraction (XRD) measurements were carried out using Panalytical X-Pert Pro MPD powder diffractometer setup; with a Cu $K_{\alpha 1}$ (λ= 0.1541784 nm) radiation source. Diffraction patterns were collected from 10° to 120° at first. The diffraction structure of the produced powder was of very high quality, compared to (Li & Zang, 2009), the obtained XRD pattern of $NaTaO_3$ material (see Figure 4.1) However, all identified peaks showed broadening to some degree.

It is worthwhile to mention that the effect of alkaline concentration is the key factor of controlling the crystal structure in any hydrothermal synthesis, as well as the temperature and the time duration. This is quite obvious in our sample structure pattern, as there no any impurity peaks related to Ta_2O_5 phase can be detected, and the reflection peaks are all indexed to as the pure phase of orthorhombic structure $NaTaO_3$ was identified only.

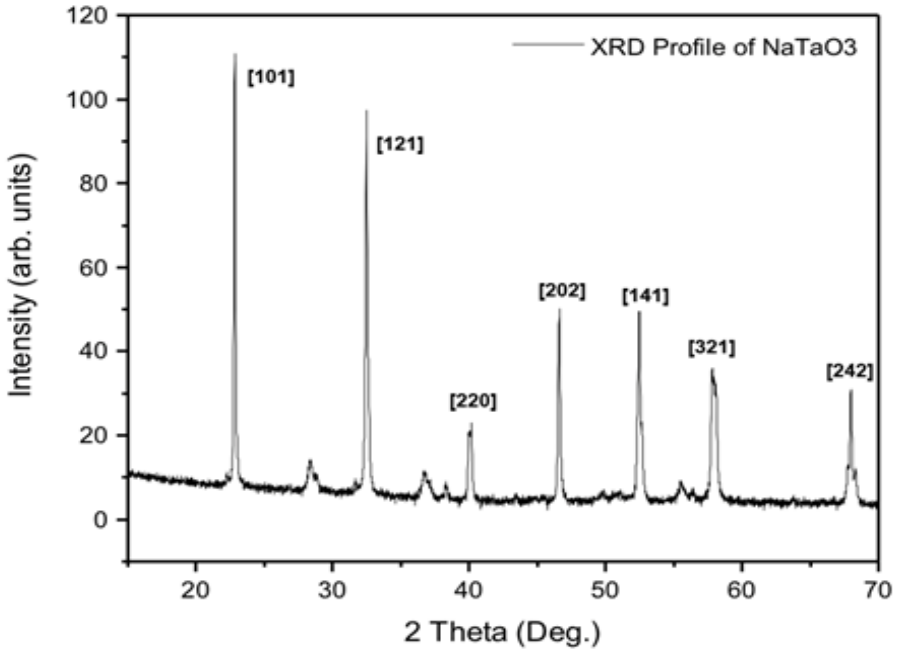

Figure 4. 1: X-Ray diffraction pattern of $NaTaO_3$ Nano-cubes

The morphology of the $NaTaO_3$ Nano-cubes sample is introduced in this section. Scanning electron microscopy was the essential tool used to investigate the powder morphology and typical particle size. As can be seen in Figure 4.2, and Figure 4.3, our synthesised powder shows a well-defined Nano cubic-shaped morphology with an edge size of approximately 200-400nm.

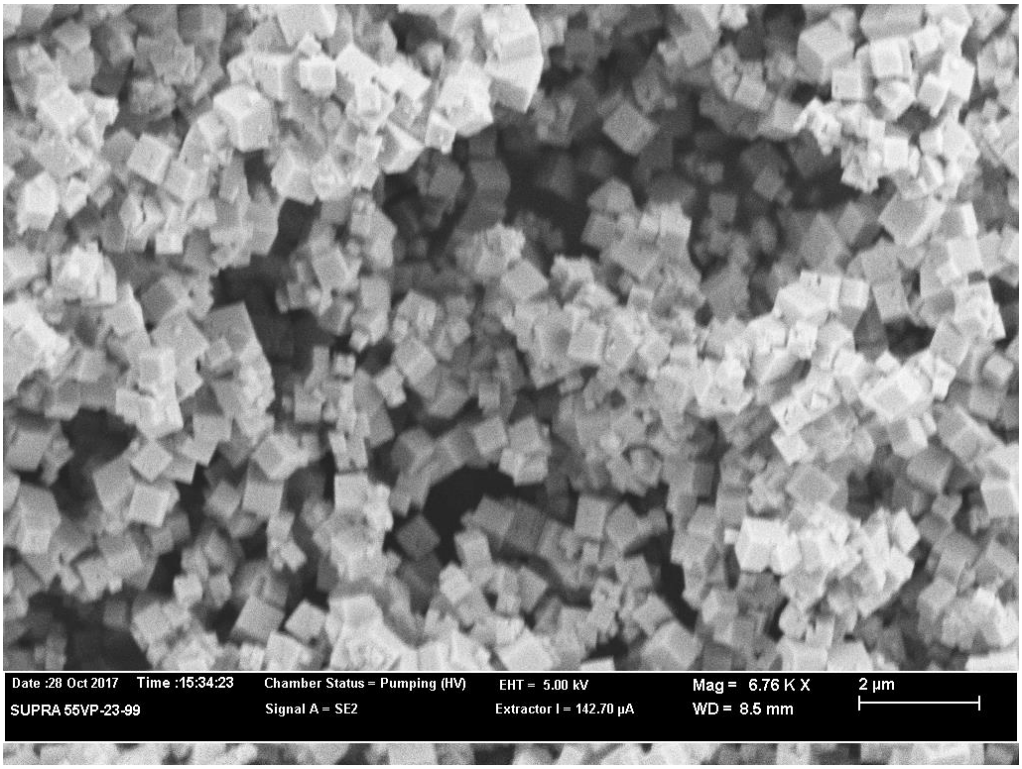

Figure 4. 2: A general SEM image showing the well-defined cubic shaped morphology of $NaTaO_3$ Nano-cubes.

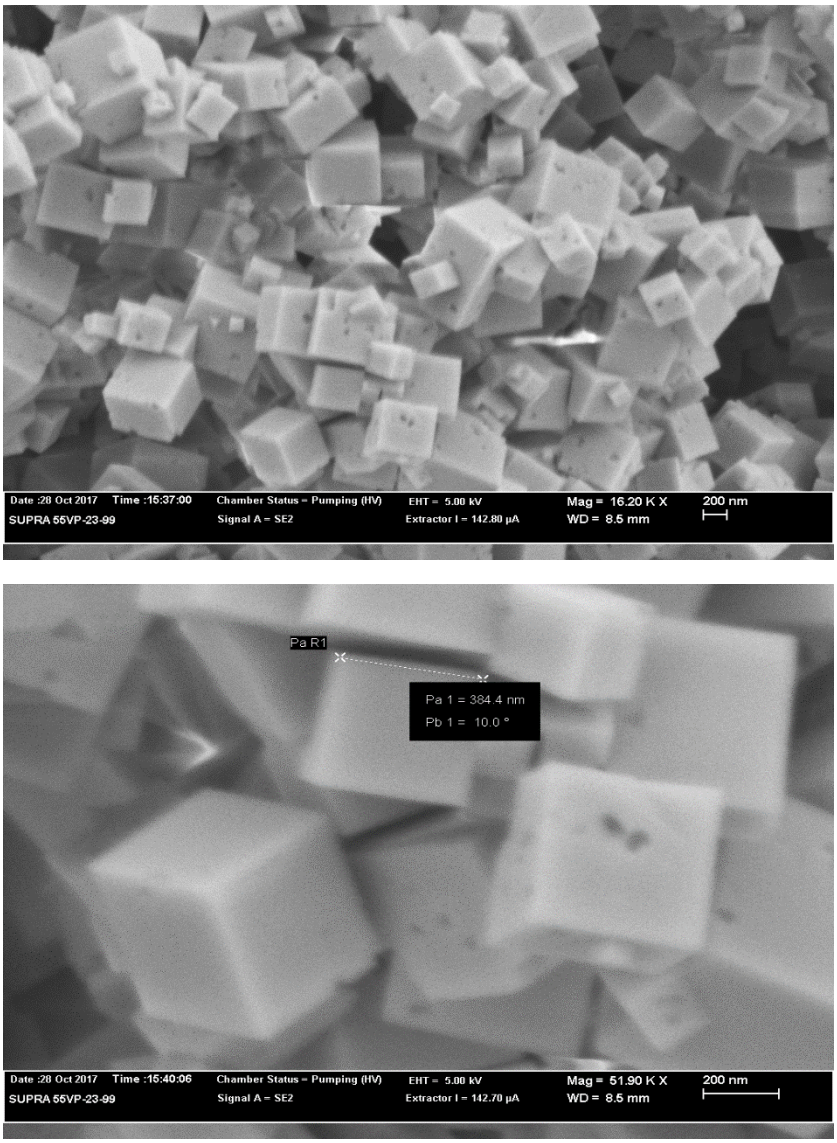

Figure 4. 3: SEM images (top and bottom) of obtained $NaTaO_3$ Nano-cubes obtained at two different magnifications exhibiting that the typical size of the Nano-cubes is in the range of 200-450nm.

The $NaTaO_3$ morphology was further analysed using high resolution transmission electron microscopy (HRTEM), performed with the JEOL 2100 LaB_6 instrument. The sample was prepared by dispersing $NaTaO_3$ powder into absolute ethanol ultrasonically for 20min., then a tiny drop of the suspension was placed onto a carbon coated 3.05 mm copper grid (Agar Scientific). The specimen was left to dry in air for few minutes, where then used to examine the powder morphology. Despite this, it was quite challenging to find exposed and clear Nano-cubes, but the HRTEM image of our sample is shown in Figure 4.4 with inset electron diffraction patterns indicating two orientations of the Nano-cubes.

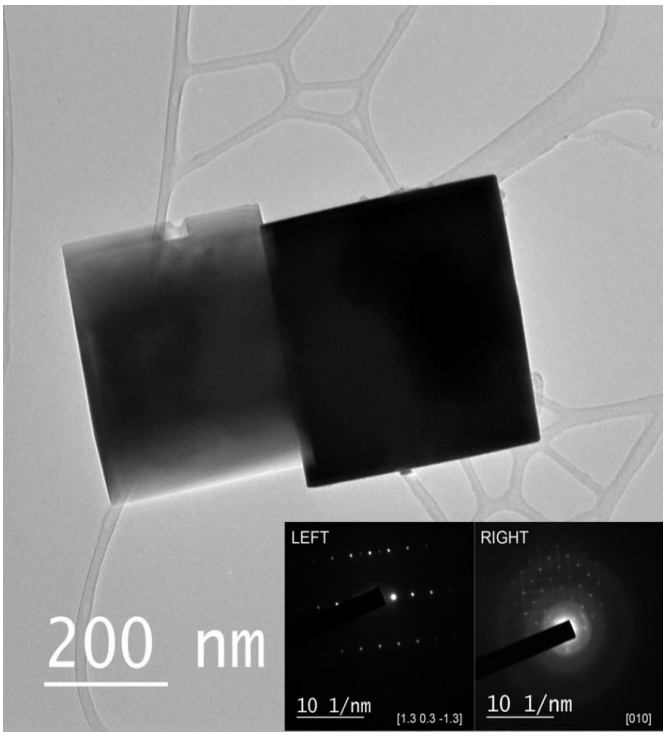

Figure 4. 4: HRTEM images and inset electron diffraction patterns of two $NaTaO_3$ Nano-cubes. Left crystal is an oblique projection, right is along [010].

To further investigate the morphological features of the synthesised structures, a particle size analysis was carried out. A series of SEM Nano-cubes images were measured in terms of their length of one side (i.e. assuming a cubic geometry). In total, more than 120 different Nano-cubes sides were measured by hand and the results recorded. This analysis indicated that the particle size exhibited a quasi-Gaussian distribution with a standard deviation, σ_{Length}, and a mean length, λ_{Length} of:

$\sigma_{Length} = 97.26$ nm

$\lambda_{Length} = 494.95$ nm

indicating that the value of the mean length is approximately half a micron, which is suitable for the use of the electrode's active material.

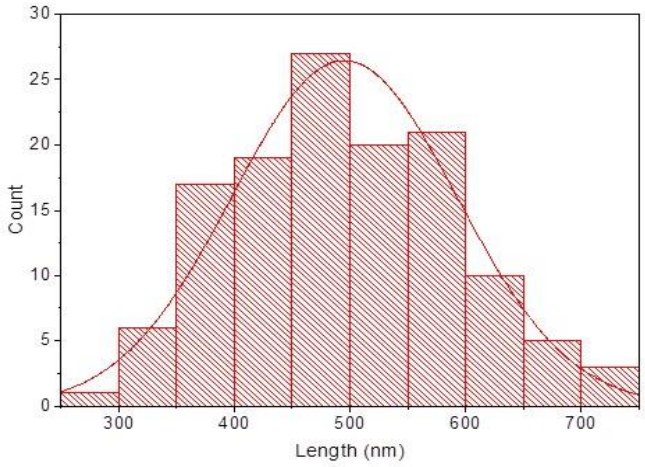

Figure 4. 5: A histogram shows the length distribution of 396 measured sides of our $NaTaO_3$ Nano-cubes structure.

The Nano-cubes volumes were calculated (assuming that the nanoparticles are perfect cubes) in order to have a sense of the average volumes of the particles. Using the information of the Nano-cubes length above, the average volume of each cube was roughly calculated. Figure 4.5 shows the approximate volume values for up to 396 nanocubes. Similarly, the volume distribution was found to be quasi- Gaussian as expected. The standard deviation, σ_{Volume} and the mean, λ_{Volume} volumes were:

$\sigma_{Volume} = .07883 nm^3$

$\lambda_{Volume} = 0.13539 nm^3$,

which indicates very small average cubes sizes.

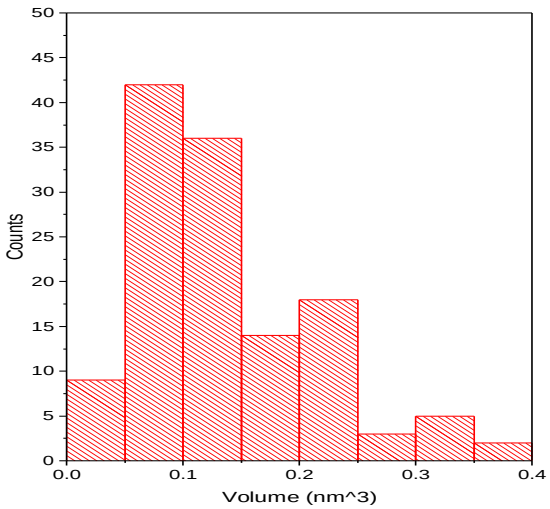

Figure 4. 6: Histogram of the enclosing volume calculated for each measure Nano-cubes. All measured Nano-cubes were assumed to be perfect cubes in the calculation

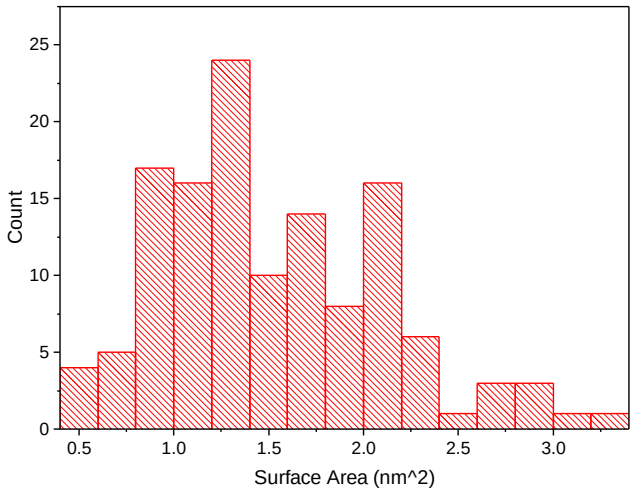

Figure 4. 7: A Calculated surface area for 396 Nano-cubes.

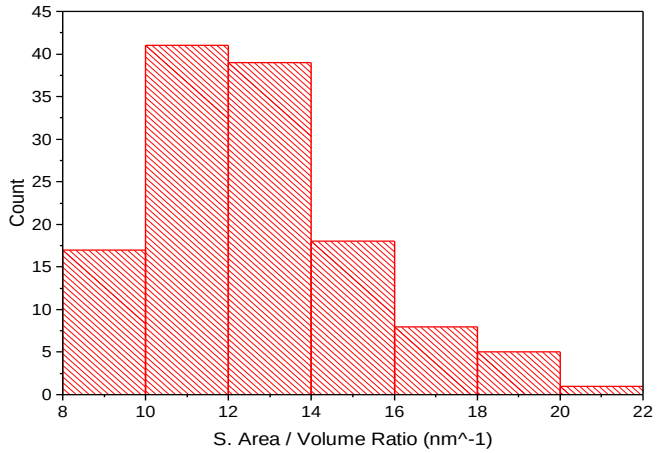

Figure 4. 8: A histogram showing surface area to volume ratio for various selected Nano-cubes particles; using SEM image. (Yu et al., 2015).

The surface area and the surface area to volume ration were then evaluated for the same Nano-cubes and found that they presented not a non-uniform distribution but a quasi-Gaussian distribution instead. The mean value of the surface area to volume ratio was found to be $\boldsymbol{\lambda}_{S.A/V\,ratio} = 12.61298 nm^{-1}$, where the standard deviation was noticeably small, $\sigma_{S.A/V\,ratio} = 2.5931\ nm^{-1}$. This physical property (i.e. m^{-1}/g); is of great importance in terms of the determination of how suitable any material is as an electrode material for lithium-ion storage purposes. (Yi *et al.*, 2012; Yoshio *et al.*, 2009; Yu *et al.*, 2015).

4.3 Electrochemical properties

As mentioned in chapter three, the electrochemical properties of the working electrodes were measured using two types of test cells. The first type; 2032 coin cells composed of our sodium tantalate, $NaTaO_3$ as athe ctive material of the working electrode, lithium metal disc as a cathode, Celgard model C2500 used as sa eparator, 1-2 spacers, and the positive and the negative casings. 1M LiPF4 in EC/EP/DEC organic solvents with 1:1:3 volume ratio was used as electrolyte. The second type of the test cells was the two electrodes Swagelok with exact same remaining components as above.

The positive electrodes were prepared from a slurry of 1.6g of sodium tantalate, $NaTaO_3$ powder as active material, 2.5g of polyvinylidene fluoride (PVdF) solution of 8% w in NMP as a binder, and 0.2g of carbon black which is well known as a conduction enhancer all mixed ultrasonically together with N-mythele-2-pyrrolidinone (NMP) solution for total time of 30-40 minutes. NMP solution is widely used in electrode fabrication. The slurry was casted onto aluminium foil using doctor blade like, and dried at around 100 °C for a few hours and was then transferred to dry overnight inside the vacuum oven.

Electrode discs of 13-16mm were punched depending on the test cell type. The 16mm was used for coin cells, where the 13mm was used to fabricate the Sawagelok cells. All cells types were assembled in the dry room at the WMG labs and tested using BioT battery tester in Galvanostatic mode. The tests were carried out at a voltage window from 0.1-3.0V at a constant current density of 10mA/g. The morphology of the engineered electrode of $NaTaO_3$ was examined using SEM. Figure 4.9 shows SEM images of the $NaTaO_3$ electrode before and after it was dried.

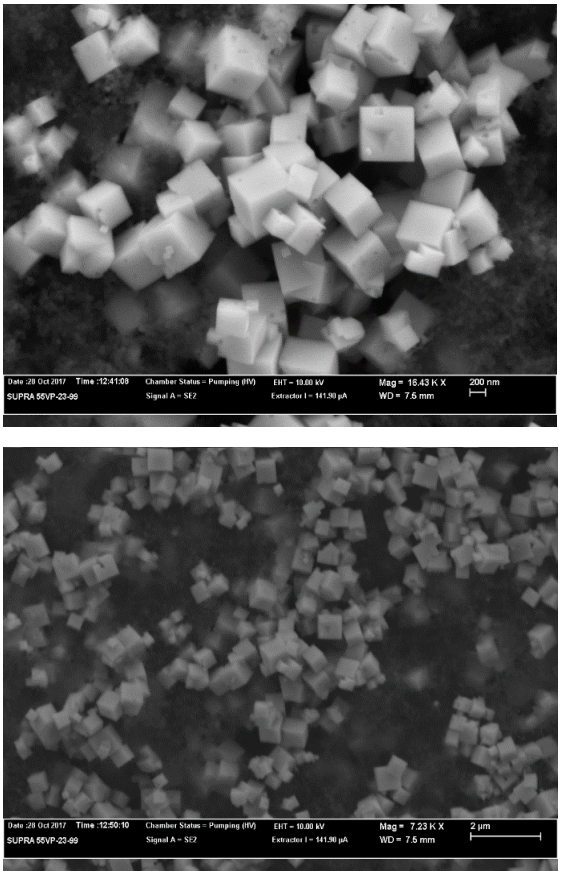

Figure 4. 9: SEM images of sodium Tantalate, NaTaO3 electrode before use at different magnifications. The particles show well distribution on the electrode surface.

The active material weight was 7.03 mg, which was 8 w% of the total electrode mass; excluding the weight of the copper foil disc. The specific capacity of the $NaTaO_3$ electrode was calculated and found to be 52mAh/g for this Swagelok test cell. From the electrochemical performance represented in Figure 4.10. the analysis shows that the reversible specific capacity of this electrode material was 52 mAh/g.

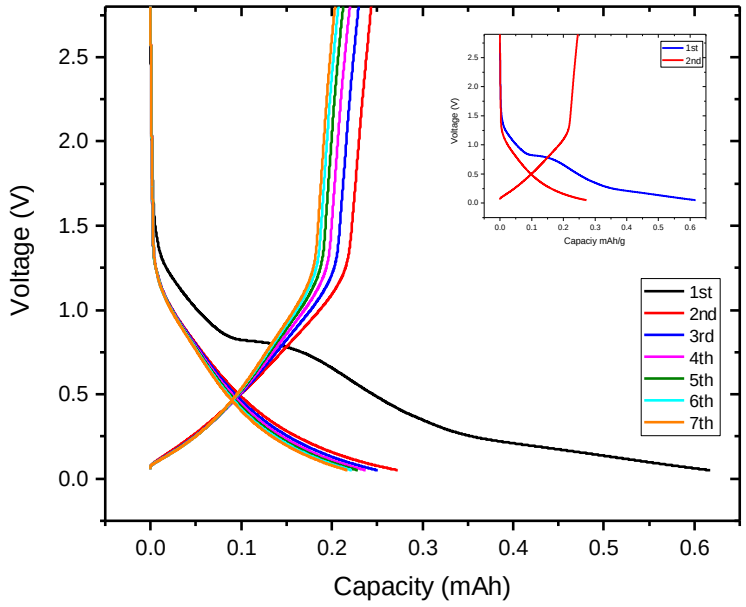

Figure 4. 10: The electrochemical performance profile of the NaTaO3 electrode at 10mA/g for 16 cycles and the Galvanostatic charge/ discharge at 10mA/g for the 1st and 2nd cycles.as a comparison of the capacity drop between the first and the second cycles.

The irreversible capacity can be calculated from the capacity of the first cycle. from the calculations, we found it to be 36.6mAh/g (the difference between the first and the second cycles' specific capacities).this is relatively high compared to the reversible amount. Figure 4.11 shows the time duration of each cycle. It shows that cycle number one took longer time which indicates a structure irreversibility transformation the material went through in the first intercalation.

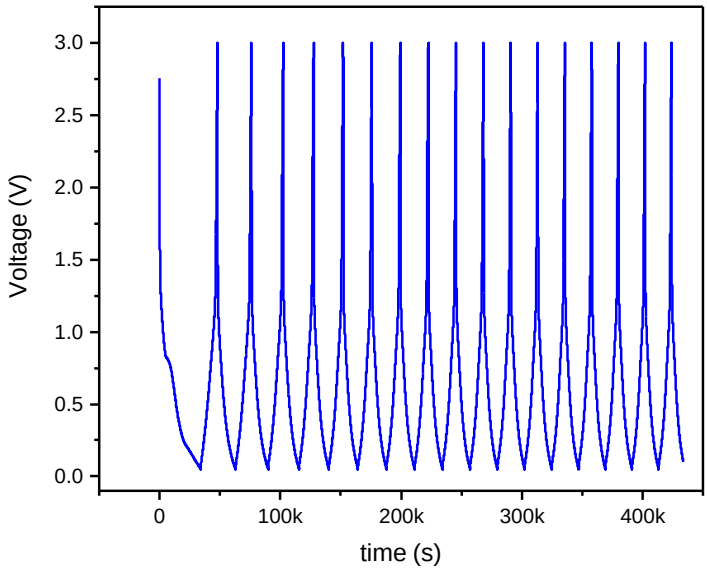

Figure 4. 11: Constant current cycling at 10 mA/g. Notice that the time for the first cycle was longer than the subsequent cycles.

For a better understanding on the electrochemical behaviour of our active material, cyclic voltammetry, CV test was applied with seven different ramping voltage , $0.5mVs^{-1}$, $1\ mVs^{-1}$, $5\ mVs^{-1}$, $10\ mVs^{-1}$, $25\ mVs^{-1}$,$50\ mVs^{-1}$, and $100\ mVs^{-1}$ between the potential range of 3 – 0.1Vvs Li^{+}/Li: as can be seen in Figure 4.13.

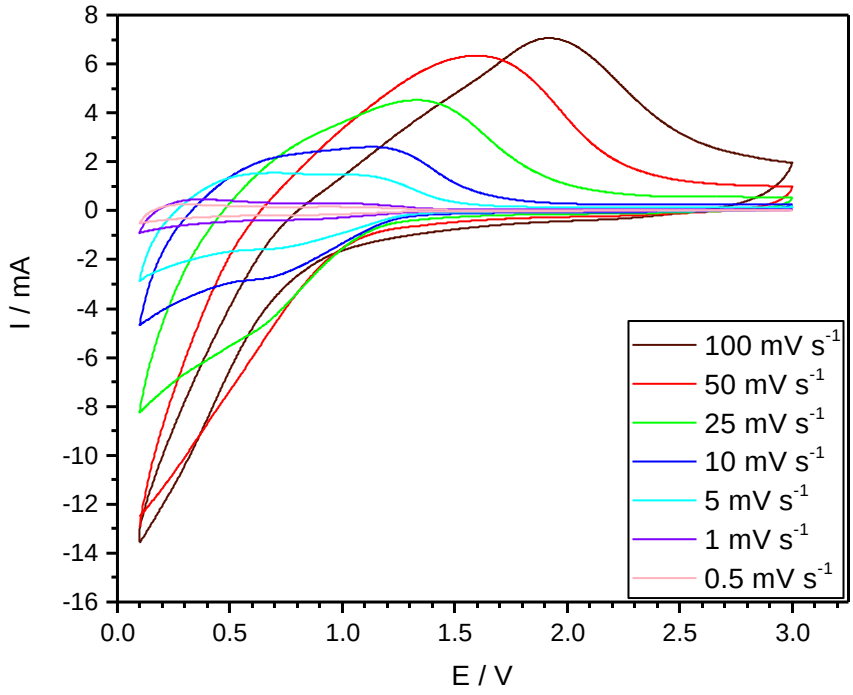

Figure 4. 12: CV curves of NaTaO3 at seven different scan rates speeds; 0.5mVs^{-1}, 1 mVs^{-1}, 5 mVs^{-1}, 10 mVs^{-1}, 25 mVs^{-1},50 mVs^{-1}, and 100 mVs^{-1}for the 2nd cycle of each ramping voltage.

Figure 4.12 exhibits the initial four CV curves of the NaTaO3 electrode at a scan rate of 10 mVs^{-1}. From the graphs in Figure 4.13, a peak shift can be noted and the highest shift id at approximately 2V for the speed rate 100mV/s. Moreover, Figure 4.14 shows the initial four CV curves of the $NaTaO_3$ electrode at a scan rate speed of 100 mVs^{-1} between the voltage range of 3.0 -0.1 V vs. Li $^{+}$/Li.

These results show that the first cycle showing the same electrochemical behaviour of the subsequent cycles except from the peak at about 2.21 volts which were reached at a lower current in the first cycle. We also ran the CV test at 100mV/s as well and this result is shown in Figure 4.15.

By comparing the two CV tests in Figure 4.13 and 4.14, it shows no much change in the overall behaviour except the peak shift. The peak is located at nearly 2 V for the speed rate of 10mV/s, whereas the voltage point where the peak exists in the second graph is around 1.57V.

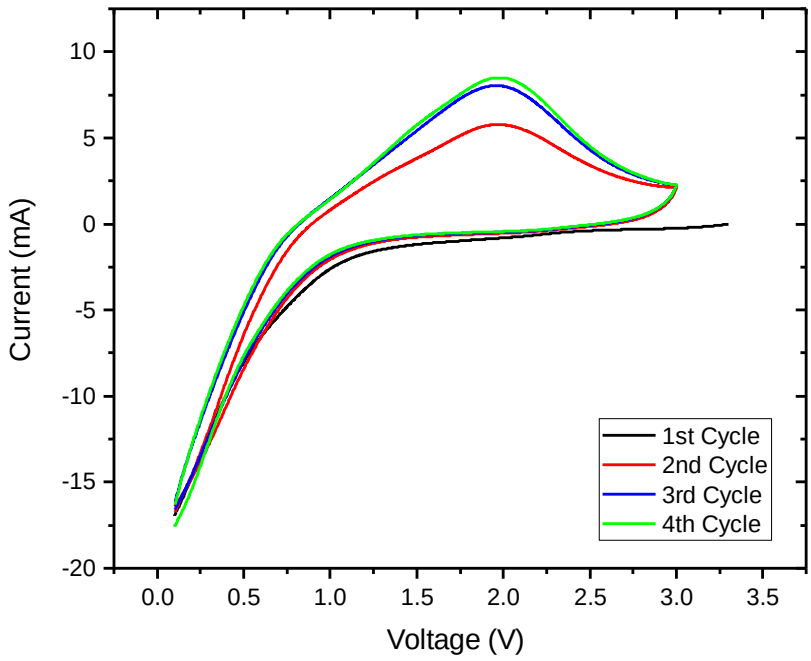

Figure 4. 13: Initial four CV curves of the NaTaO3 electrode at a scan rate speed of 10 mVs^{-1} between the voltage range of 3.0 -0.1 V vs. Li^{+}/Li.

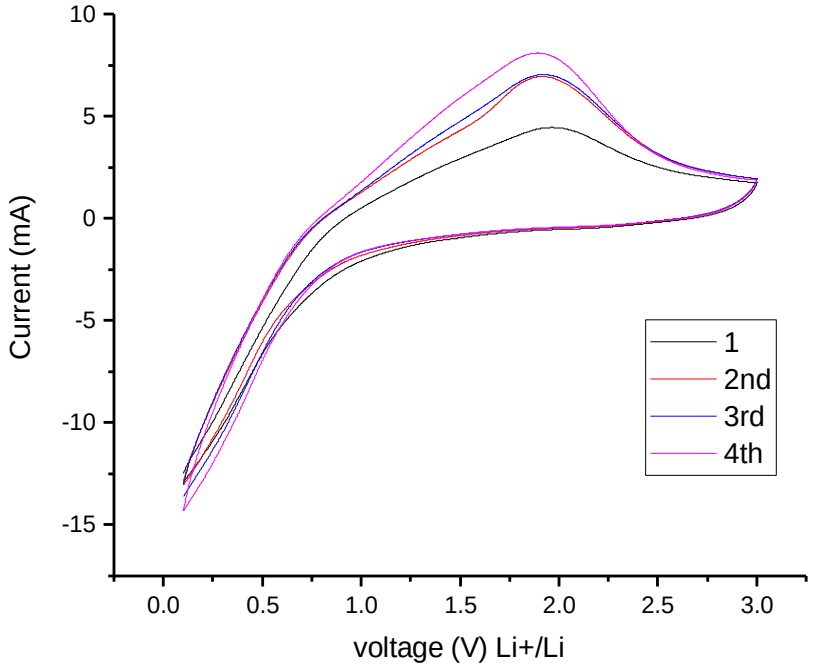

Figure 4. 14: Initial four CV curves of the $NaTaO_3$ electrode at a scan rate speed of 100 mVs^{-1} between the voltage range of 3.0 -0.1 V vs. Li^+/Li

We made one attempt to fabricate test cells of $NaTaO_3$ and $LiTaO_3$ active materials as electrodes we have used aluminium foil instead of copper. An interesting but complicated electrochemical behaviour results were depicted. Coin-type cells were first used for this work. The electrode fabrication went exactly through the same procedure, but the slurry was spread on the top of aluminium sheet instead. The electrodes left to dry under vacuum overnight. The same procedure was then followed in the test cells assembly as for the other cases.

A CV test was run on the two test cells from 3-0.1V at a speed rate of 0.1 mV s^{-1} for four cycles for each electrode. Figure 4.15 represents Cyclic voltammetry curves of our second material which will be discussed in the next chapter; $LiTaO_3$ at a scan rate of 0.1 mV s^{-1} in the voltage range 3–0.1 V vs. Li+/Li. The the first cycle showed an interesting

behaviour during the oxidation process, where two peaks at 0.46V and 0.75 respectively. The same behaviour can be seen with the sodium tantalate, NaTaO3 electrode, exhibited in Figure 4.16. but with one sharp peak during the oxidation at around 0.54 V and another possible weak peak at approximately 0.25 V. one reliable explanation was presented by (Nakahara *et al.*, 2003) and others that this behaviour is due to the full valence of Ta5+ to Ta4+ and due to the partial reduction as suggested. More investigations in depth have to be conducted on both the structure and the electrochemical properties of tantalum oxide family as there are very limited studies on them regarding ion storage issue especially the supercapacitor electrodes. (Chan & Majid; Nakahara *et al.*, 2003; Yu *et al.*, 2015)

In general, a there was an irreversible capacity took place during the first cycle which was proved from the electrochemical behaviour. More structure investigations and electrochemical characterisation has to be conducted for a better understanding of order to solve the (Long *et al.*; Matsumura *et al.*, 1995)

4.4 Conclusion

We exhibited our work on producing sodium tantalate Nano-particles. We were able to grow a pure phase of pseudo cubic structure of sodium tantalate, $NaTaO_3$ under a significantly low temperature using the hydrothermal method. The surface area to volume ratio was estimated using the statistical method. More accurate methods would be suggested if the work time for this project wasn't ended. Our material growth work has given us a better understanding of the produced structure.

The electrochemical tests show that more work needs to be done to study the electrochemical properties of this material as a Li/Na-ion storage. The capacity drop, however, shows that more factors need to be studied before a final conclusion can be decided. Unfortunately, our work on this project came to an end before further studies were applied

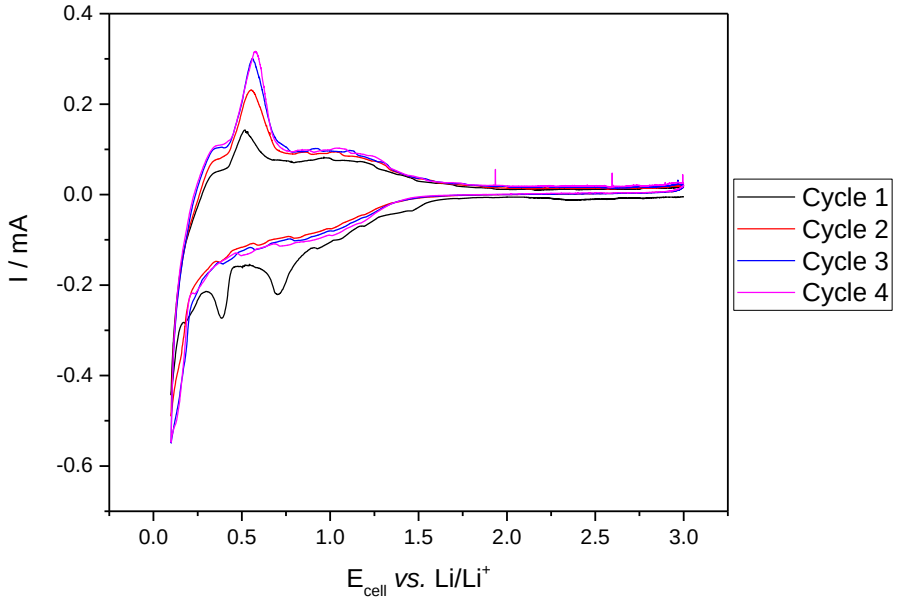

Figure 4. 15: Cyclic voltammetry curves of $LiTaO_3$ at a scan rate of 0.1 mV s^{-1} in the voltage range 3–0.1 V vs. Li/Li^+.

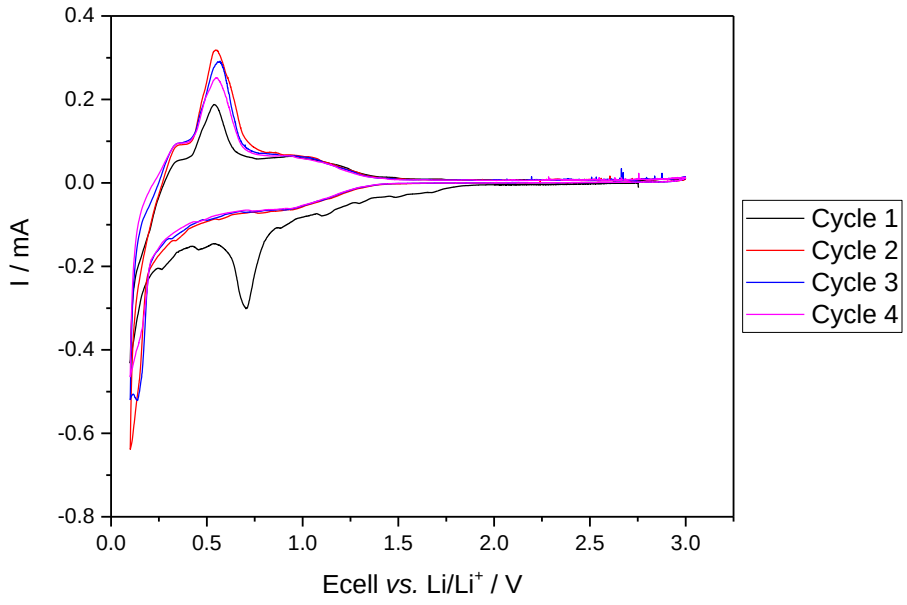

Figure 4. 16: Cyclic voltammetry curves of $NaTaO_3$ at a scan rate of 0.1 mV s^{-1} in the voltage range 3–0.1 V vs. Li/Li^+.

.

References

Chan, P. & Majid, S. Metal oxide-based electrode materials for supercapacitor applications.

Kay, H. & Miles, J. (1957) The structure of cadmium titanate and sodium tantalate. *Acta Crystallographica*, 10 (3): 213-218.

Li, X. & Zang, J. (2009) Facile hydrothermal synthesis of sodium tantalate ($NaTaO_3$) nanocubes and high photocatalytic properties. *The Journal of Physical Chemistry C*, 113 (45): 19411-19418.

Long, R. T., Sutula, J. A. & Kahn, M. J. Flammability of cartoned lithium ion batteries. [online] Available from:

Matsumura, Y., Wang, S. & Mondori, J. (1995) Mechanism leading to irreversible capacity loss in Li-ion rechargeable batteries. *Journal of the Electrochemical Society*, 142 (9): 2914-2918.

Nakahara, K., Nakajima, R., Matsushima, T. & Majima, H. (2003) Preparation of particulate Li4Ti5O12 having excellent characteristics as an electrode active material for power storage cells. *Journal of Power Sources*, 117 (1-2): 131-136.

Reznitchenko, L., Turik, A., Kuznetsova, E. & Sakhnenko, V. (2001) Piezoelectricity in NaNbO3 ceramics. *Journal of Physics: Condensed Matter*, 13 (17): 3875.

Saito, Y., Takao, H., Tani, T., Nonoyama, T., Takatori, K., Homma, T., Nagaya, T. & Nakamura, M. (2004) Lead-free piezoceramics. *Nature*, 432 (7013): 84.

Shanker, V., Samal, S. L., Pradhan, G. K., Narayana, C. & Ganguli, A. K. (2009) Nanocrystalline $NaNbO_3$ and $NaTaO_3$: Rietveld studies, Raman spectroscopy and dielectric properties. *Solid State Sciences*, 11 (2): 562-569.

Yi, T.-F., Li, X.-Y., Liu, H., Shu, J., Zhu, Y.-R. & Zhu, R.-S. (2012) Recent developments in the doping and surface modification of LiFePO4 as cathode material for power lithium-ion battery. *Ionics*, 18 (6): 529-539.

Yoshio, M., Brodd, R. J. & Kozawa, A. (2009) Lithium-ion batteries : science and technologies. [online] New York, NY: Springer

Yu, Z., Tetard, L., Zhai, L. & Thomas, J. (2015) Supercapacitor electrode materials: nanostructures from 0 to 3 dimensions. *Energy & Environmental Science*, 8 (3): 702-730.

Chapter 5

Material Synthesis and Electrochemical Properties of Lithium Tantalate, $LiTaO_3$

Lithium tantalate, $LiTaO_3$ is one of the alkali tantalates ($ATaO_3$, A = alkali metal). It is well known for its attractive physical properties and is widely used in optical and electronic applications such as detectors, waveguides, LASERs, and electro-optic devices. (Atuchin *et al.*, 1984; Busacca *et al.*, 2008)

In this work, $LiTaO_3$ powder material was used as an active material electrode in the lithium-ion test cells. The low-temperature sol-gel method was carried out to synthesise our material which was produced with exceptionally high purity.

5.1 Material synthesis

The $LiTaO_3$ material was prepared by dissolving 0.5101g of Lithium Acetate dehydrate, $LiO_2C_2H_3.2H2O$ (Sigma-Aldrich, higher >97%) and 1.1047 g of tantalum (V) oxide, Ta_2O_5 ((Sigma-Aldrich, 99.997% trace metal basis), in ethanol. After the mixture was thoroughly stirred for at least one hour until it was homogenous, approximately1.5 g of citric acid crystals, $C_6H_8O_7$ were added to the mixture to form the gel, and set to slowly dry at 100^0C to evaporate the citric acid and the ethanol. This can take quite a few hours depending on how much ethanol was used. The stirring was kept continuous with the temperature until finally a thick white precursor was formed. The precursor has then been calcinated in the furnace under air at 750^0C for 12-48 hours. Table 5.1 exhibiting a breakdown of the sample synthesis procedure for using Sol-gel synthesis method, and the reaction of the products can be summarised by the following chemical reaction:

$$Ta_2O_5 + LiO_2C_2H_3.2H_2O + C_6H_8O_7 \dashrightarrow LiTaO_3 + \text{gas waste} \uparrow \quad (5.1)$$

Parameter Name	Parameter Value
Mass of Tantalum (V) Oxide	1.104725g
Lithium Acetate dehydrate, $LiO_2C_2H_3.2H_2O$	0.5101g
citric acid crystals, $C_6H_8O_7$	1.5 g
Dwell temperature	750°C
Temperature Ramp Rate	10°C
Dwell Time	12-48 hours
Precipitate Colour	Pure White
Drying Temperature (to evaporate excess ethanol)	90-110°C
Drying Time	2-3 hours

Table 5. 1: A breakdown of the sample synthesis procedure for a typical Sol-gel synthesis

Characterisations and imaging were done to ensure the correct material was produced and to investigate its morphology. The material was found to have particles of size $200nm$ upwards (Figure 8a) which is within the range of expectation. However higher magnification, as in Figure 8b), shows the particle surface to be made of small near spherical out dents, which was not expected. To ensure the image was not distorted due to sample charging, a thin film of gold particles was placed over the sample.

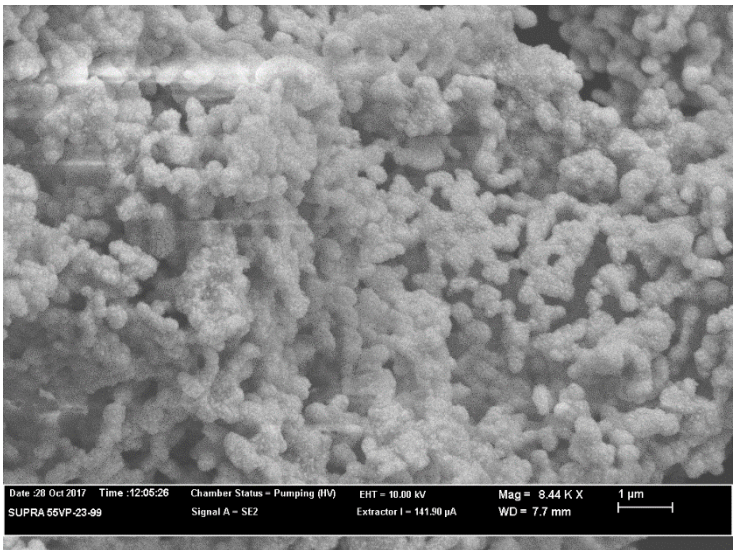

Figure 5. 1: SEM micrographs of Lithium Tantalate particles at different magnifications: a) 3.6k, b)15.6k

5.2 Results and Discussion

The $LiTaO_3$ phase was identified by using powder X-ray diffraction (XRD) measurements were carried out using Panalytical X-Pert Pro MPD powder diffractometer setup; with a Cu $K_{\alpha 1}$ (λ= 0.1541784 nm) radiation source. Diffraction patterns were collected between 10° to 100°. The diffraction structure of the produced powder was of very high purity and similar to other the same material patter compared to other publications (Cullity, 1978; Ishihara, 2009, Yamanaka, 2016). Figure 5.2 shows the XRD profile of our $LiTaO_3$ powder with a high level of purity without any secondary phases observed.

Furthermore, our material profile proved it has a rhombohedral structure when the pattern was matched to ICDD pattern, which may significantly open the door to a better understanding of the lithium ion kinetics during cycling

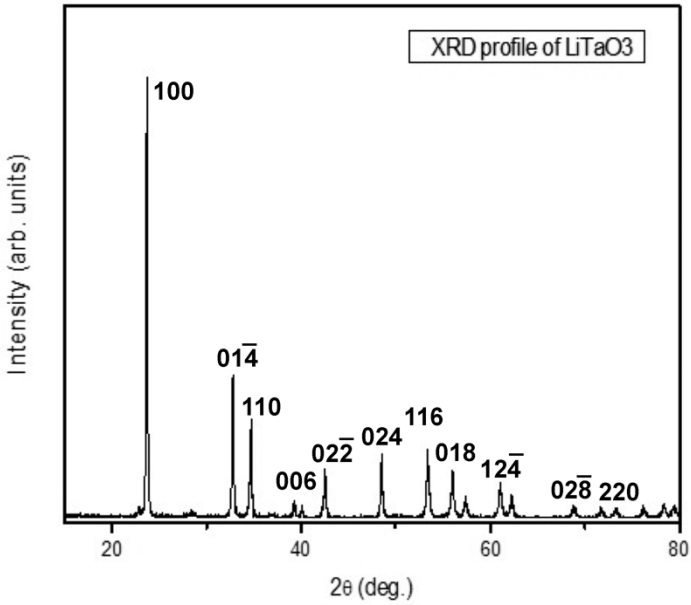

Figure 5. 2: XRD profile of $LiTaO_3$ calcined at 750 ^{0}C for 12hrs with the major peaks indexed – all of the other peaks correspond to the phase pure material (Yamanaka, 2016)

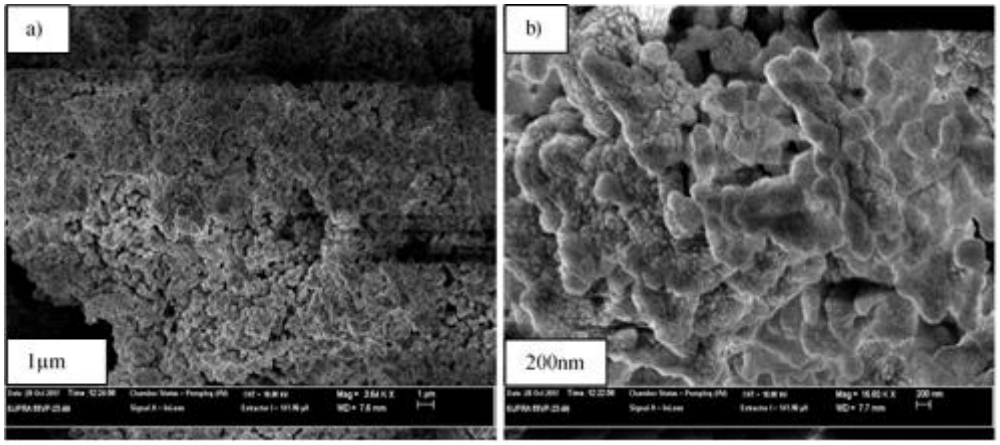

Figure 5. 3: SEM micrographs of Lithium Tantalate particles at different magnifications: a) 3.6k, b)15.6k

To view the powder sample using the SEM, it had first to be gold coated to avoid the charging problem which we faced in all three materials under investigation during this work. Figure 5.4 shows SEM image of the synthesised, $LiTaO_3$ powder using the sol-gel method. The particles sizes were found to range between 200-500 nm.

These observations (Figure 5.3, Figure 5.4) confirm the XRD result that the smallest particles are 200nm or less and the structure of the particles is almost spherical which agrees with the XRD results discussed above. This also shows a promising lithium-ion transfer between the electrodes as a result of the surface area to volume ratio as large amount of the particle surface area has remained exposed.

5.3 Electrochemical Properties of Lithium Tantalate, $LiTaO_3$

In Chapter 3, all the electrode fabrication and the test cells assembly were stated in details. the electrochemical properties of the electrodes were measured using two types of test cells. The first type; 2032 coin cells composed of our sodium tantalate, $NaTaO_3$ as the active material of the positive electrode of the test cell, lithium metal disc as a cathode, Celgard model C2500 used as a separator, 1-2 spacers, and the positive and the negative casings. 1M $LiPF_4$ in of EC (i.e. ethylene carbonate), PC (i.e. propylene carbonate), and DEC (i.e. diethyl carbonate) organic solvents with 1:1:3 volume ratio was used as our electrolyte. The second type of the test cells was the two electrodes Swagelok with the exact same reaming components as above.

The counter electrodes were prepared from a slurry contains 1.6g of sodium powder as an active material, 0.2g of polyvinylidene fluoride (PVdF) as a binder (we used PVdF solution in N-mythele-2-pyrrolidinone, NMP), and 0.2g of carbon black as a conductive material all mixed ultrasonically together with N-mythele-2-pyrrolidinone (NMP) solution. The slurry was cast onto aluminium foil using doctor blade like, and dried at around 100 ^{0}C for few hours, where then transferred to dry overnight inside the vacuum oven.

Electrode discs of 13-16mm were punched depending on the test cell type. The 16mm was used for coin cells, where the 13mm was used to fabricate the Swagelok cells. All cells types were assembled in the dry room at the WMG labs and tested in Galvanostatic mode. All cells were cycled between 0.1V and 3 V. at a current density of 10mA/g. The charge capacity is measured at a using a potentiostat and the cyclic voltammetry (CV) is achieved at a sweeping rate of 0.1 mV/s. the tester used is from the BioLogic Science

Some charged/discharged samples were disassembled and the morphology of the electrode after the use was investigated. unfortunately, the disassembled cell was not known if it was in a charge or discharge mode when it was taken for the SEM when the used electrode was examined.

Figure 5.4 reproduces SEM images for the new made lithium tantalate, (i.e. $LiTaO_3$) electrodes in different magnifications, whereas Figure 5.4 illustrates the SEM images for a cycled electrode (coin cell #6L). it is clear that the lithium tantalate, LiTaO3 particles are still dominant even after the cycling process. The sample was cycled for 6 times at a speed rate of 0.1 mV^{-1} from 3.0 V – 0.1 V.

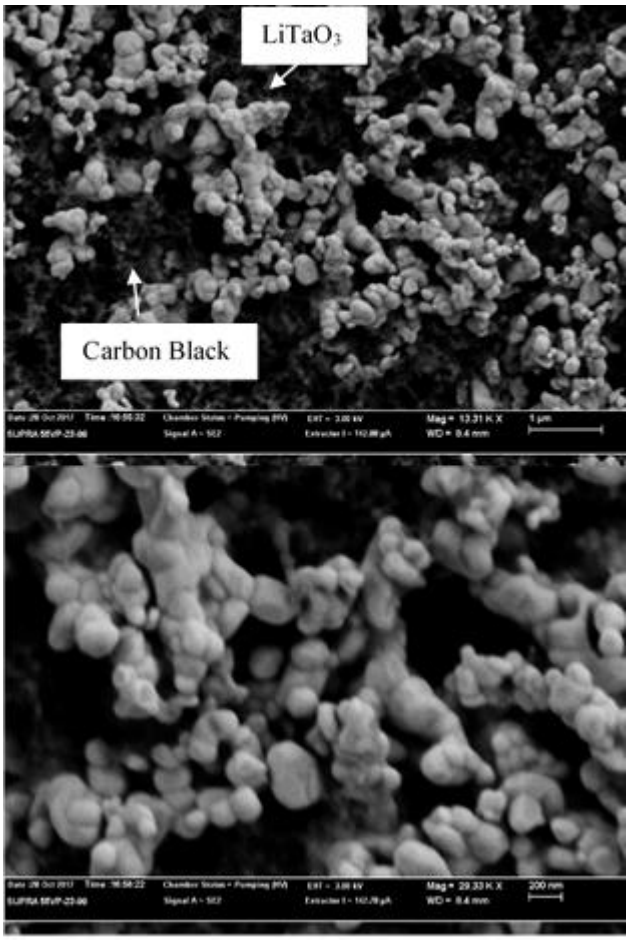

Figure 5. 4: SEM images with different magnifications for the prior to use $LiTaO_3$ electrode.

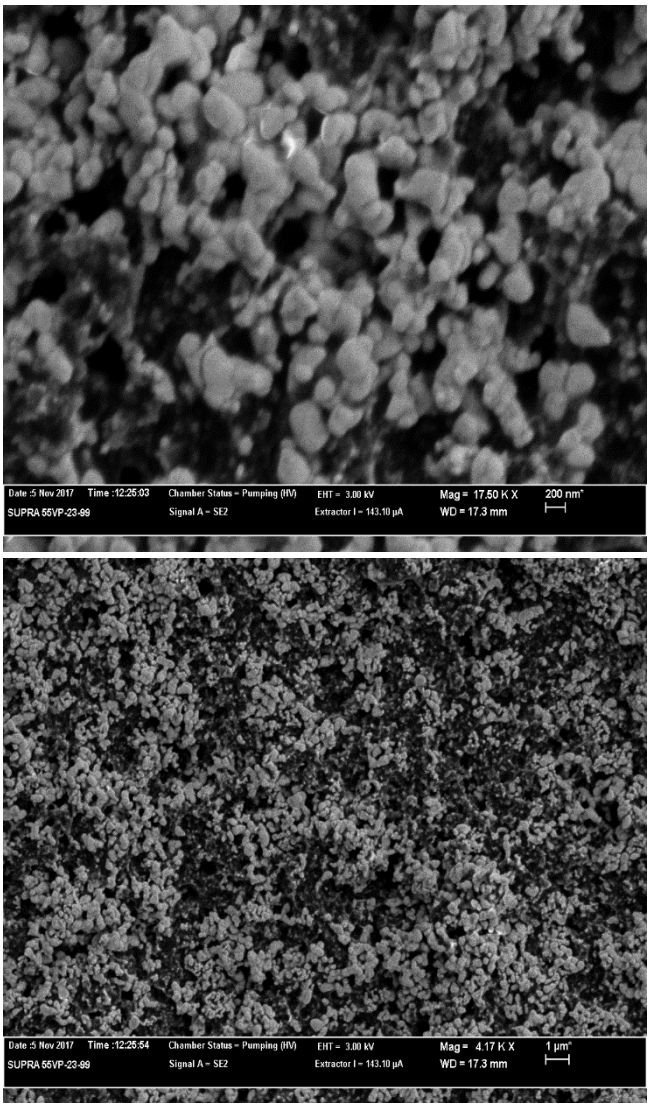

Figure 5. 5: SEM images with different magnifications for #6 coin cell electrode after use.

The active material mass was found to be 7.902 mg, which was 80% of the total electrode mass excluding the weight of the current collector disc. The specific capacity of the $LiTaO_3$ electrode was analysed using the values of the active material mass and the indicated value of the second cycle's capacity, 0.547mAh, from the graph in Figure 5.6 . The analysis shows the reversible specific capacity of our material electrode for the given mass is about 69 mAh/g.

Figure 5.6 shows that there is a high drop in the value of the irreversible capacity of almost 50%. From the calculations, we found it to be 50mAh/g the difference between the first and the second cycles' specific capacity). Moreover, it dropped again for the subsequent cycles even after the second one but not as noticeable as the difference between the first cycle and the subsequent cycles. This can be noticed from the cycling time of the first cycle as well. In Figure 5.7, the time for the first cycle was longer than that taken for the subsequent cycles. One of the explanations for the capacity loss (the irreversible capacity) is the fact that is bonded to the partial reduction Ta^{4+} to Ta^{3+} and the full valence variation of Ta^{5+} to Ta^{4+}as well as the significant irreversible phase transformation resulting in an irreversible capacity (Han *et al.*, 2011; Long *et al.*). This means that our active material exhibits anodic behaviour.

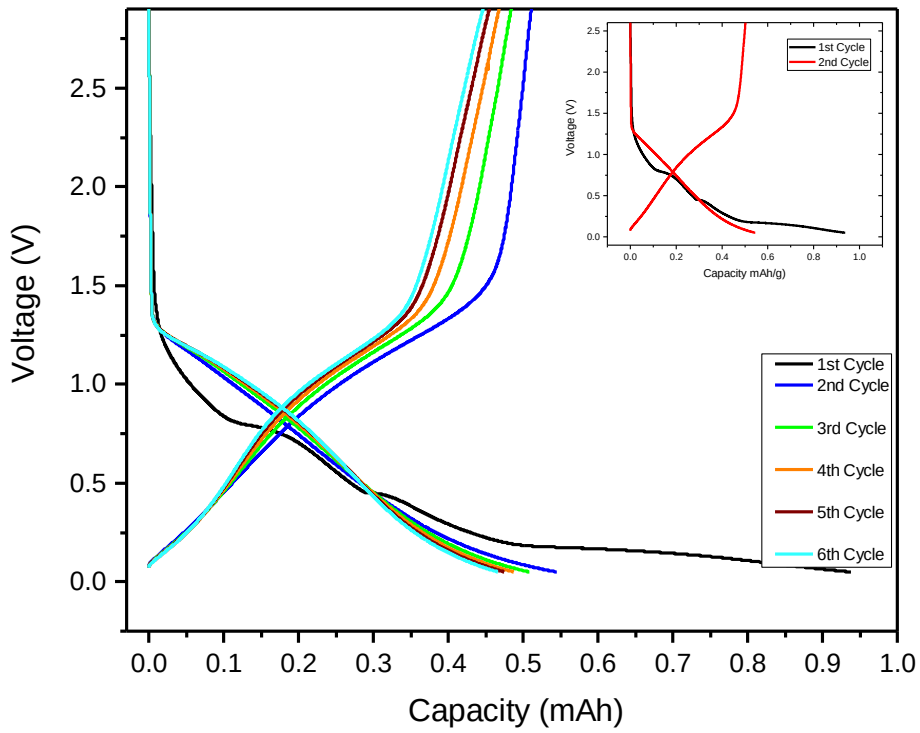

Figure 5. 6: The electrochemical performance profile of the $LiTaO_3$ electrode at 10mA/g for 16 cycles and the Galvanostatic charge/ discharge at 10mA/g for the 1st and 2nd cycles as a comparison of the capacity drop between the first and the second cycles.

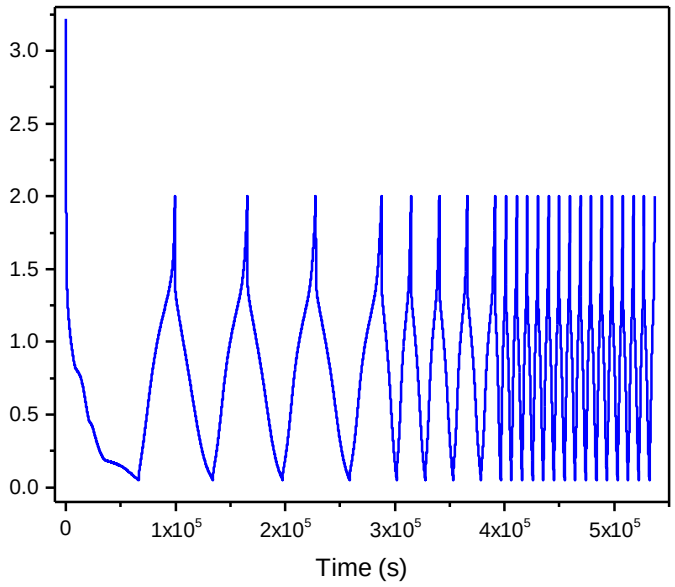

Figure 5. 7: Constant current cycling at 10 mA/g.(Notice that the time for the first cycle was longer than the subsequent cycles).

The OCV voltage was 3.30 V and the Glavanostati, we decided to apply a series of C-rate test on the Swagelok test cell was set for different scan speeds, 0.5mVs^{-1}, 1 mVs^{-1}, 5 mVs^{-1}, 10 mVs^{-1}, 25 mVs^{-1},50 mVs^{-1}, and 100 mVs^{-1} between the potential range of 3 – 0.1Vvs Li $^{+}$/Li: (see Figure 5.8).

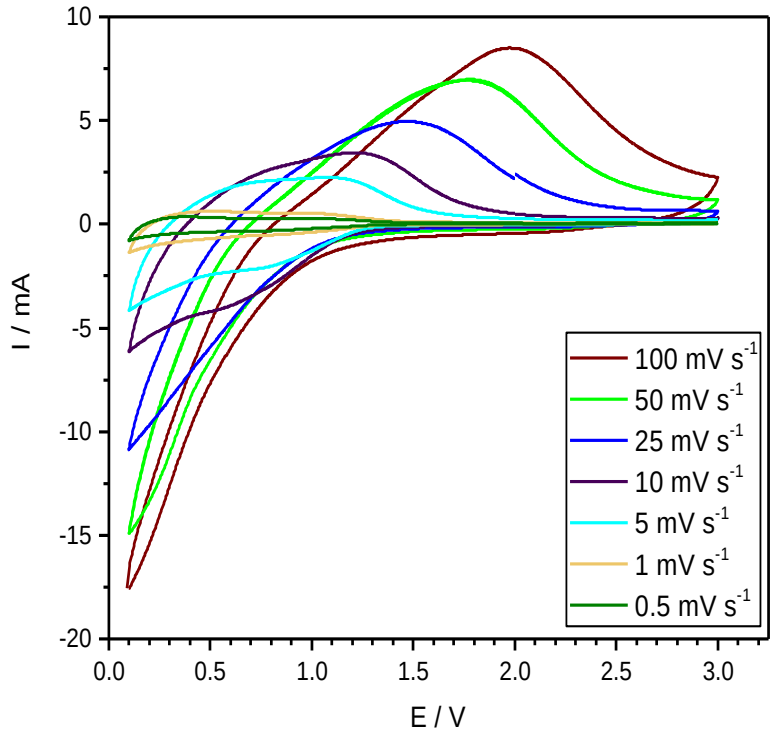

Figure 5. 8: CV curves of $LiTaO_3$ at seven different scan rates speeds; 0.5mVs^{-1}, 1 mVs^{-1}, 5 mVs^{-1}, 10 mVs^{-1}, 25 mVs^{-1},50 mVs^{-1}, and 100 mVs^{-1}for the 2nd cycle.

Figure 5.9; exhibits the initial four CV curves of the $LiTaO_3$ electrode at a scan rate of 10 mVs^{-1}. The first cycle appears to be inverted with no significant peaks. We decided to check the electrochemical behaviour by running another rate scan at different rate speed, 100 mVs^{-1} for three cycles to compare the difference under different rate speeds. The first cycle is the same though. Figure 5.10 shows the initial four CV curves of the $LiTaO_3$ electrode at a scan rate speed of 100 mVs^{-1} between the voltage range of 3.0 -0.1 V vs. Li^+/Li. It shows that the first cycle showing the same electrochemical behaviour of the subsequent cycles except for the peak at about 2.21 volts which was reached at a lower current in the first cycle.

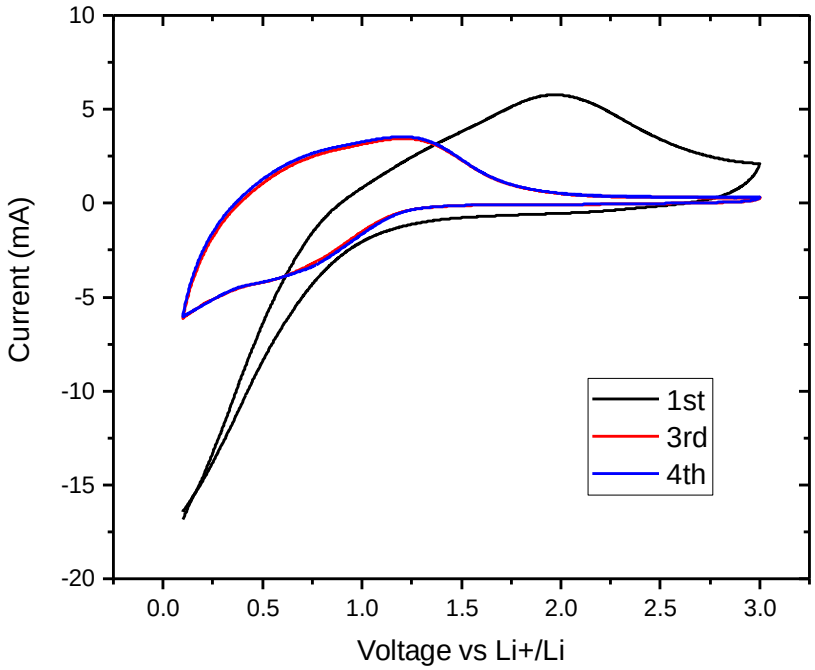

Figure 5. 9: Initial four CV curves of the LiTaO3 electrode at a scan rate speed of 10 mVs^{-1} between the voltage range of 3.0 -0.1 V vs. Li $^{+}$/Li.

One peak can be detected at 0.56V for the subsequent cycles at a ramping speed of 10 mVs^{-1} which they appear to be consistent excluding the behaviour of the first cycle. and 1.27V in the cathodic process (i.e. the discharging process) excluding the first cycle, (see Figure 5.9)

On the other hand, only a stable pair of peaks throughout can be recognised in the subsequent cycles cantered at 0.56V/1.30V which indicated the electro chemical behaviour of our $KTaO_3$ electrode. In general, a huge irreversible capacity took place during the first cycle which appeared as a drop in the overall practical capacity of this active material's electrode. (Long *et al.* 2014; Matsumura *et al.*, 1995; Inaba *et al.*, 2005; Yoon *et al.*, 2001)

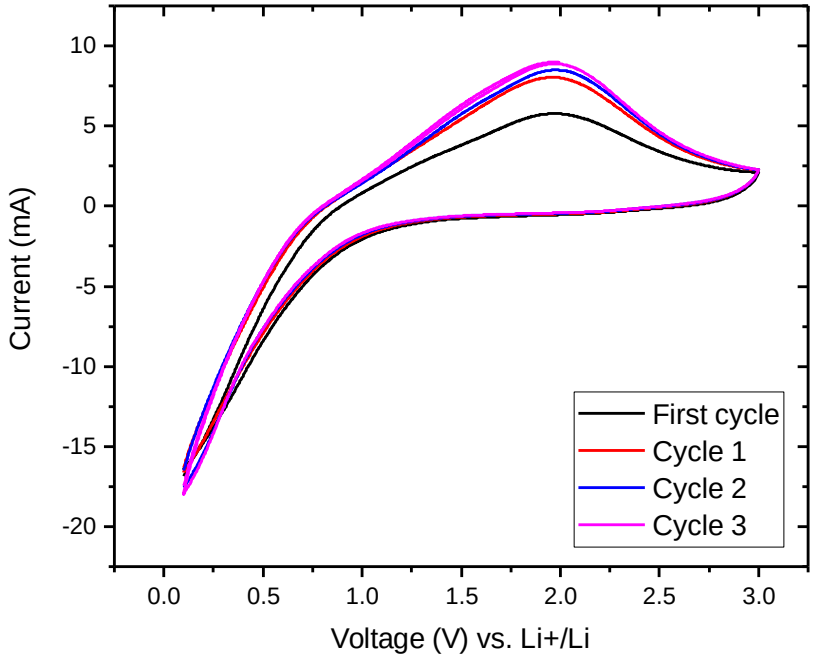

Figure 5. 10: Initial four CV curves of the $LiTaO_3$ electrode at seven different scan rate speed of 10 mVs^{-1} between the voltage range of 3.0 -0.1 V vs. Li^{+}/Li

It should be noted that four cycles are not enough to build a strong definite conclusion on the electrochemical behaviour of the $LiTaO_3$ electrodes. However, the consistent resultant capacity of the type of material acting as an active material for lithium ion storage is quite interesting and needs further extended studies in order to go deep in the explanation of its behaviour, not necessary as an anode but as a promising candidate for ion storage ingeneral, with some modifications, to be applied on the material structures of materials such as many other of the alkali metal bronzes formed from the various transition metals.

5.4 Conclusion

A successful growth of perovskite lithium tantalate was achieved using the chemical method; Sol-gel. We were able to produce a high surface area powder and made the attempt to examine it for the lithium and sodium ion storage.

The powder then used as active material in the coin cells for the purpose of electrochemical testing it as Li-ion storage. The consistent resultant capacity of the type of material acting as an active material for lithium ion storage is quite interesting and needs further extended studies in order to go deep in the explanation of its behaviour, not necessary as an anode but as a promising candidate for lithium-ion storage as well. However, our electrochemical test shows that there is a high drop in the value of the irreversible capacity after the first cycle.

References

Atuchin, V., Ziling, K. & Shipilova, D. (1984) Investigation of optical waveguides fabricated by titanium diffusion in LiTaO [sub] 3 [/sub]. *Quantum Electronics*, 14 (5): 671-674.

Busacca, A., D'Asaro, E., Pasquazi, A., Stivala, S. & Assanto, G. (2008) Ultraviolet generation in periodically poled lithium tantalate waveguides. *Applied Physics Letters*, 93 (12): 121117.

Cullity, B. (1978) Elements of X-ray Diffraction, Addison-Weseley, Philippines.

Han, H., Song, T., Bae, J.-Y., Nazar, L. F., Kim, H. & Paik, U. (2011) Nitridated TiO 2 hollow nanofibers as an anode material for high power lithium ion batteries. *Energy & Environmental Science*, 4 (11): 4532-4536.

Inaba, M., Uno, T. & Tasaka, A. (2005) Irreversible capacity of electrodeposited Sn thin film anode. *Journal of power sources*, 146 (1-2): 473-477.

Ishihara, T. (2009) Structure and properties of perovskite oxides. In: *Perovskite Oxide for Solid Oxide Fuel Cells*. Springer: 1-16.

Long, R. T., Sutula, J. A. & Kahn, M. J. Flammability of cartoned lithium ion batteries, 2014.:

Matsumura, Y., Wang, S. & Mondori, J. (1995) Mechanism leading to irreversible capacity loss in Li ion rechargeable batteries. *Journal of the Electrochemical Society*, 142 (9): 2914-2918.

Yamanaka, T., Nakamoto, Y., Takei, F., Ahart, M., Mao, H-K. & Hemley R., (2016) *Journal of Applied Physics*, 119(7), 075902/1-12.

Yoon, S., Kim, H. & Oh, S. M. (2001) Surface modification of graphite by coke coating for reduction of initial irreversible capacity in lithium secondary batteries. *Journal of power sources*, 94 (1): 68-73.

Chapter 6

Material Synthesis and Electrochemical Properties of Potassium Tantalate, $KTaO_3$

In this work, our aim was to produce the third perovskite potassium tantalate, $KTaO_3$ powder material which was attempted to be used as an active material electrode in the lithium-ion test cells. Two synthesising methodes; the solid state method and the hydrothermal method were carried out to synthesise our material. The solid state was terminated after the final product found to suffers from multi-phases and all the attempts to improve to a single perovskite phase were failed. On the other hand, the hydrothermal method produced a very fine product of pure perovskite phase (> 99%). Here, we introduce our hydrothermal synthesis in details.

The chapter is organized as follows: the syntheses methods and processing protocols used in each method were first discussed, followed by a description of the techniques used for materials characterization and for the measurement of the electrochemical half-cell performance. The results for our proposed structure and for carefully designed control experiments are then presented and discussed.

6.1 Material synthesis

We used two routes to growing potassium tantalate perovskite KTaO3. The first method was the solid-state synthesis, with different temperatures ranging from 1000-1300

ºC for 2-6 hours sintering. The second route was the hydrothermal method, under significantly low temperature (200-240 ºC) for 24-48 hours.

6.1.1 Solid state synthesis of $KTaO_3$ perovskite Phase

Working with dense $KTaO_3$ ceramics itself is a challenge from our experience in this work. Here, the attempt was to produce a pure perovskite $KTaO_3$ powder.

The powder was prepared using two chemicals as the starting producs; potassium carbonate, K_2CO_3 (Sigma-Aldrich, 99.97%) and tantalum pen oxide, Ta_2O_5 (Sigma-Aldrich, 99.997%). Potassium carbonate was dried overnight at 200 ºC prior to use. The starting mixture (5g) of the two compounds was then mixed in acetone inside a granite mortar pestle until a dry, homogeneous mixture is produced. After that, the slurry was left to dry at 60ºC for few hours. The mixture was pressed into 13mm in diameter pallets using a hydraulic press and calcined at 800 ºC. the produced powder was milled for the second time and pressed manually into pellets. Finally, it was sintered at a temperature range of 1000-1300 ºC for 2-6 hours, in order to find the optimum temperature and sintering time duration for the formation of this material.

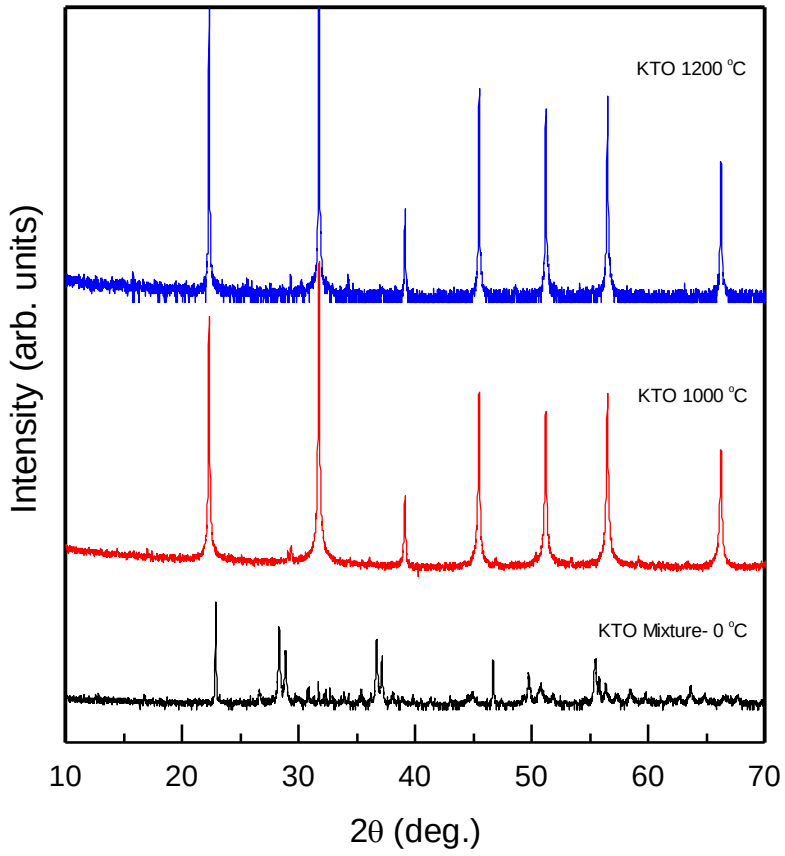

Figure 6. 1: XRD pattern of $KTaO_3$ powder sintered at 0^0C, 1000^0C, and 1200^0C

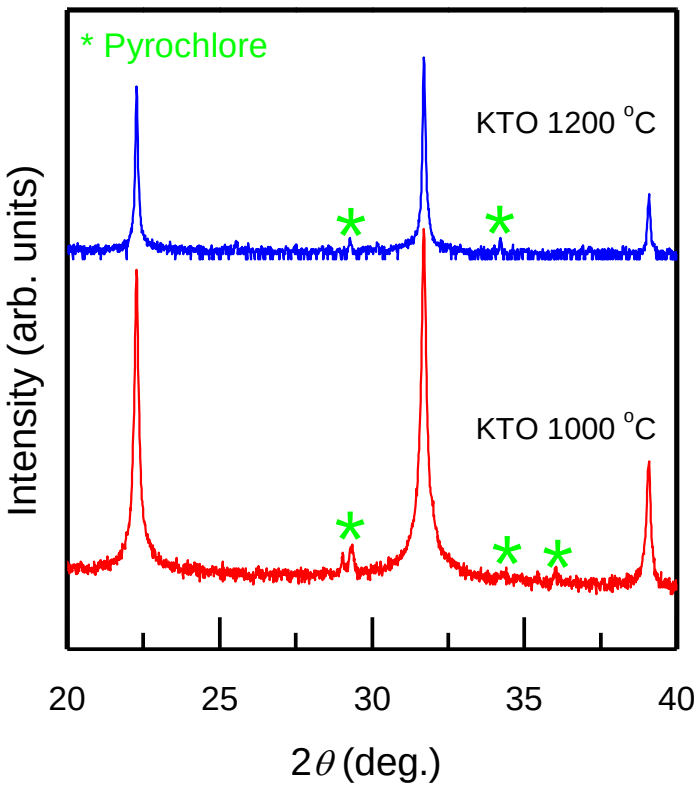

Figure 6. 2: XRD pattern of $KTaO_3$ powder sintered at 1000^0C, and 1200^0C and the existence of the pyrochlore phase

The phase composition was studied using X-ray diffraction to investigate the produced $KTaO_3$, whereas the powder morphology was examined by SEM technique. The XRD profile showed a multiphase phenomenon. At least four peaks were clearly designated pyrochlore, $K_2Ta_2O_6$ as a second phase. Figure 6.1; presents three XRD profiles of sintered powders under different temperatures; pre-sintered mixture at 0^oC, and sintered at 1000, and 1200^0C None of the optimised temperatures or time durations attempts succeeded to produce a pure *KTaO3* perovskite phase. (Chen *et al.*, 1983; Shimada *et al.*, 1984). Pyrochlore phase can be detected from the XRD profile of 1000, and 1200^0C in figure 6.2, all powder profiles contain some pyrochlore defects (green stars). Consequently, this synthesis method was terminated and alternatively, a hydrothermal synthesis was carried out to produce our *KTaO3* perovskite powder. Increasing the sintering temperature

proves no enhancement in the structure purity. It shows that new complicated phases start to appear. Figure 6.3 shows the XRD profile of a sintered mixture at 1300 ºC. New peaks appear not related to the perovskite structure indicating that temperature raising isn't the solution when dealing with volatile elements like potassium, K.

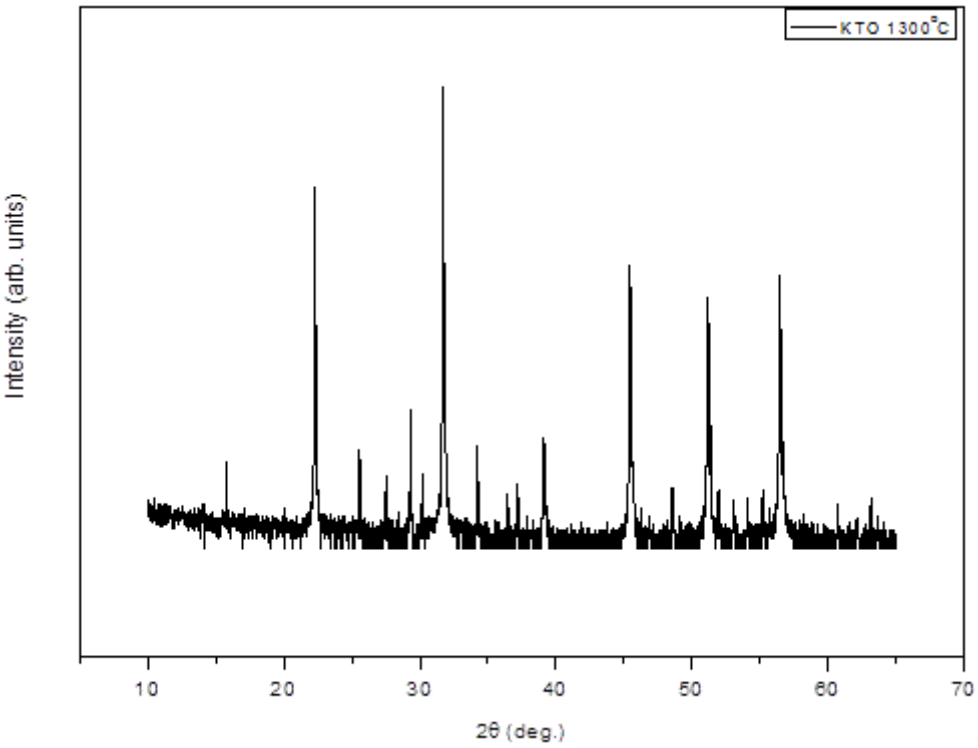

Figure 6. 3: XRD pattern of $KTaO_3$ powder sintered at 1300^{0}C, and the profile shifted away from the pure perovskite structure.

Figure 6.4 illustrates SEM image for *KTaO3* powder synthesised by the solid-state method at >1000ºC. It is clear that the powder has more than one phase or alternatively, contaminated. Comparing the peaks of the XRD profile to a standard pattern, multi-phases were detected with dominant pyrochlore phase.

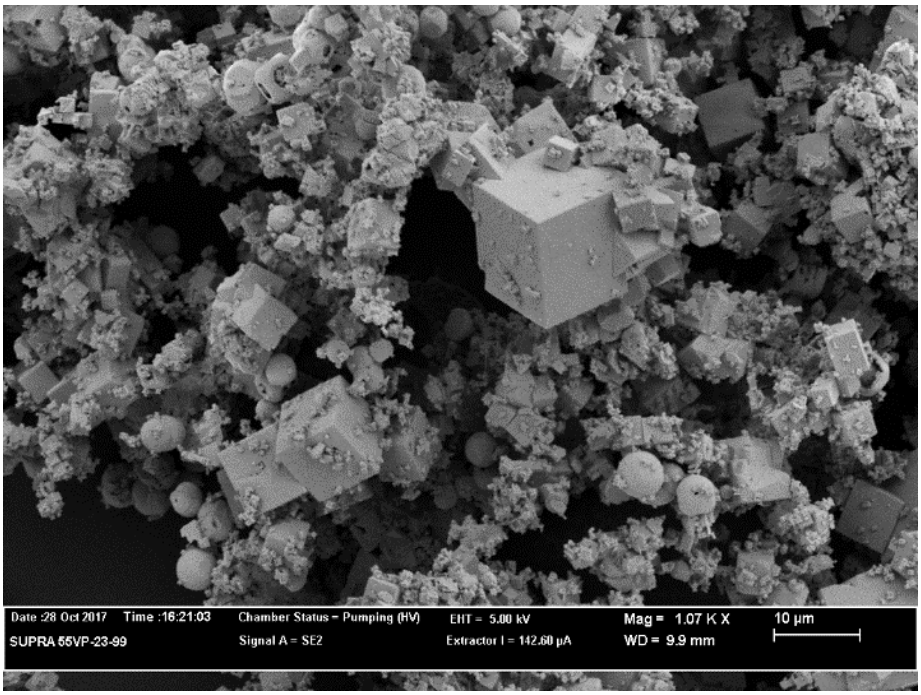

Figure 6. 4: SEM image of solid-state synthesised $KTaO_3$ powder showing the multiphase nature of the product.

6.1.2 Hydrothermal Synthesis of $KTaO_3$ Perovskite Powder

It is well known that synthesising potassium tantalate powders demands very high temperature. Techniques such as solid state synthesis, which was described above in section 6.1.1, is based on mixing two or more powders and as a result long sintering time duration and temperatures of 1000ºC or higher. Our main obstacle was with the formation of another phase; of potassium tantalate; pyrochlore, $K_2Ta_2O_6$, which starts to crystallise at around 650 °C (Sleight, 1968).

Using low-temperature synthesis method such as hydrothermal synthesis would resolve this problem. (Duan *et al.*, 1998) for the first time has reported that a relatively pure perovskite structure of $KTaO_3$ could be synthesised at a temperature as low as 200°C. In fact, I am grateful to Dr Richard Walton from chemistry department who introduced me

to the hydrothermal synthesis and gave me the chance to work in his lab to produce such a fine nanostructured version of perovskite structure of $KTaO_3$ powder.

In this method, $KTaO_3$ was synthesized by reacting 0.0025- 0.005 moles of tantalum (V) chloride, $TaCl_5$ (Sigma-Aldrich, 99.9%). in 20-40 ml aqueous, alkaline solutions containing 20M *KOH* at 240°C in a 25 – 50 ml Teflon-lined, stainless steel hydrothermal container (Parr Co., Moline, IL) respectively. The bomb was left for 24hrs inside a conventional oven. It is worthy to note that the volume of alkaline solution to be used in one synthesis is dependent on the autoclave volume.

The autoclave was taken out of the oven after 24hrs to cool down to room temperature. Deionised water was used to wash the filtered powder several times, using filter papers and a filter funnel. The wet product was left to dry at 60°C for few hours before it was ready for the next step; powder characterisation. Table 6.1 summarises the full details of the hydrothermal synthesis of fine particulate $KTaO_3$.

The $KTaO_3$ powder morphology was examined using scanning electron microscopy, SEM. Phases were identified by using powder X-ray diffraction (XRD) measurements were carried out using Panalytical X-Pert Pro MPD powder diffractometer setup; with a Cu $K_{\alpha 1}$ (λ= 0.1541784 nm) radiation source. Diffraction patterns were collected between 10° to 120°. The reaction inside the autoclave can be simply summarised in the following equation:

$$(1\ \text{mole})\ Ta_2Cl_5 + (2\ \text{moles})\ KOH \dashrightarrow (2\ \text{moles})\ KTaO_3 \qquad (6.1)$$

Parameter Name	Parameter Value
Mass of Tantalum (V) Chloride	2.5-4 g
KOH Concentration	20 M
Dwell temperature	240°C
Temperature Ramp Rate	5°C
Dwell Time	24 hours
Autoclave Volume	25-50 mL
Precipitate Colour	Pure White
Drying Temperature	60°C
Drying Time	4-6 hours

Table 6. 1: A breakdown of the sample synthesis procedure for a typical hydrothermal synthesis

6.2 Results and Discussion

The diffraction structure of the produced powder from the hydrothermal method was of a high purity with no pyrochlore phase peaks present. Figure 6.5 shows the XRD profile of our perovskite $KTaO_3$ powder with a high level of purity without any secondary phases observed. Using the nanocube size statistical measurements which were previously discussed in Chapter 4, the material was found to have particles of size 250 nm upwards which is within the range of our expectation. This can be directly observed from the obtained SEM images. Around 300 $KTaO_3$ nanocubes were used in the statistical measurements. The mean value of the length, λ_{Length} was found to be about 1.62 microns. This result agrees with the average size of $KTaO_3$ cubes in the SEM images (see Figure 6.6).

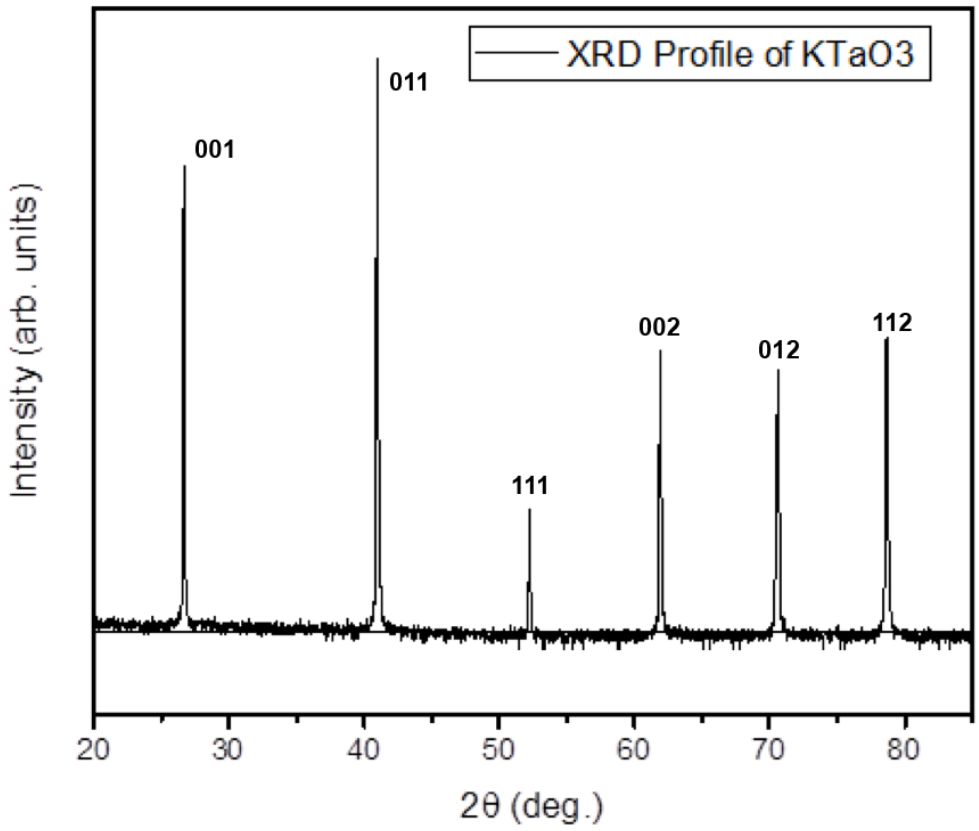

Figure 6. 5: XRD profile of $KTaO_3$ hydrothermally obtained at 240°C for 24hrs which has an excellent match with the published structure (Zhurova et al., 1992).

Compared to our state-of-the-art, $NaTaO_3$ nanocubes, $KTaO_3$ cubes are significantly larger; as well as the fact that the $KTaO_3$ crystal structure corresponds to nearly perfect cubes with a sharp Ta-O-Ta angle of 180° (Figure 6.7). This structural feature may challenge lithium-ions flux through the host layers. On the other hand, it can be a promising candidate for capacitors or supercapacitors or the solar semiconductors. (Zhang et al., 2014).

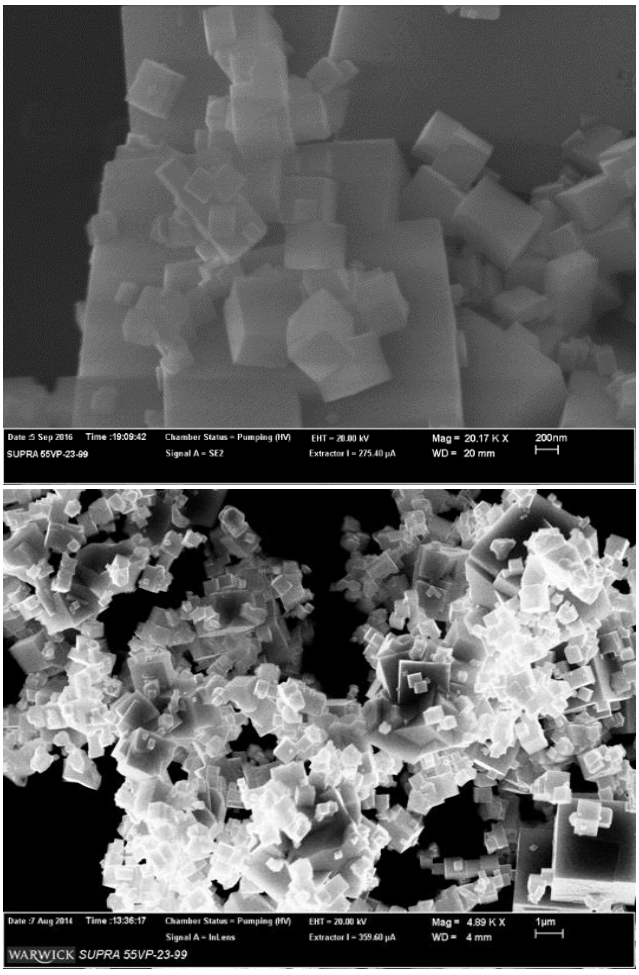

Figure 6. 6: SEM images for 2 different samples of potassium tantalate, $KTaO_3$ cubes synthesised using the hydrothermal synthesis method showing high magnification (top) and low magnification image.

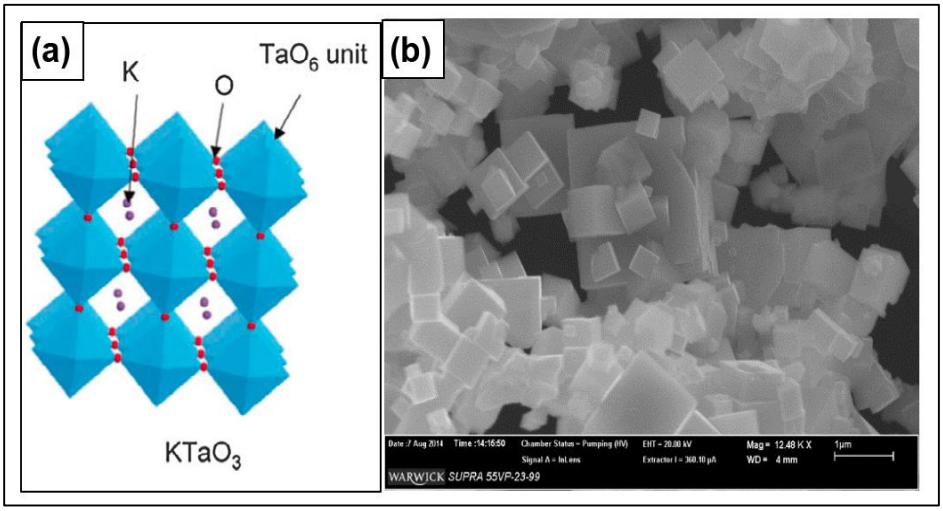

Figure 6. 7: a) shows the ideal $KTaO_3$ structure and b) SEM image of potassium tantalate, $KTaO_3$ cubes prepared by hydrothermal synthesis.

For optimum SEM images, the powder samples had to be first coated with a thin gold layer to prevent the charging problem which was encountered with all three perovskite materials studied during this investigation.

6.3 Electrochemical Properties of Potassium Tantalate, $KTaO_3$

The electrochemical properties of this material were then investigated. The material was inserted into Swagelok cells (Figure 6.7) and examined for different some electrochemical characteristics. The impedance test as an example showed a complex behaviour which is worth wise to be more investigated. But because of the time limitation, we had to stop here. However, some properties were still tested using Swagelok cells. The coin cell test failed to give any significant results which may be related to the gap spacing between the positive and the negative electrode. However, the Swagelok cells insure the electrode spacing not a possible reason for cell operation failure as screws can be correctly tightened during the cell assembly. Figure 6.8 shows the difference between the two

assembled Swagelok cells when the right one is correctly assembled and the left one was not.

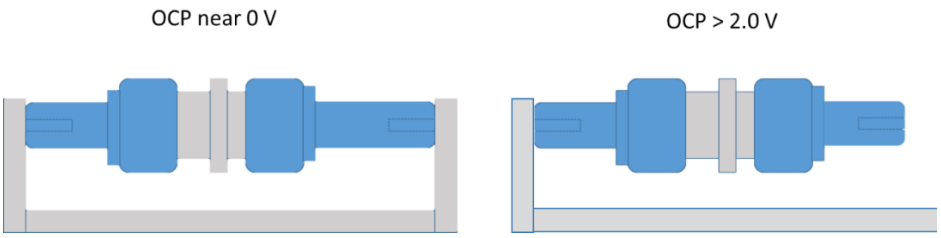

Figure 6. 8: Swagelok cells assemblies as used in this study. Right the cells placed under increased compression to ensure electrical contact through the cell.

Electrochemical properties

As mentioned in Chapter 3, the electrochemical properties of the anode electrodes were measured using two types of test cells. The first type; 2032 coin cells composed of our sodium tantalate, $NaTaO_3$ as the active material of the anode electrode, lithium metal disc as a cathode, Celgard model C2500 used as a separator, 1-2 spacers, and the positive and the negative casings. 1M $LiPF_4$ in EC/EP/DEC organic solvents with 1:1:3 v/v%; was used as the electrolyte. The second type of the test cells was the two electrodes Swagelok with exact same reaming components as above.

Positive electrodes were prepared from a slurry consists of 1.6g of sodium powder as an active material, 0.2g of polyvinylidene fluoride (PVdF) as a binder, the PVdF was mixed in NMP solution and with 8% w and 2.5g of the solution was added to the mixture, and 0.2g of carbon black as a conductive material all mixed ultrasonically together with N-mythele-2-pyrrolidinone (NMP) solution. The slurry was cast onto aluminium foil using doctor blade like, and dried at around 100C for few hours, where then transferred to dry overnight inside the vacuum oven.

Electrode discs of 13-16mm were punched depending on the test cell type. The 16mm was used for coin cells, where the 13mm was used to fabricate the Sawagelok cells. All cells types were assembled in the dry room at the WMG labratories and tested using BT2000 battery tester in Galvanostatic mode. The tests were carried out at a voltage window from 0.2-3.0V at a constant current density of 10mA/g.

The active material mass calculated and found to be 7.58 mg. It represents 80% of the total electrode mass without excluding the Cu weight. the practical capacity of the $KTaO_3$ electrode found to be 23.2 mAh/g, which was disappointing.

Despite the disappointing result of the capacity value, we decided to apply a series of C-rate test on the Swagelok test cell under different scan speeds, 0.5mVs^{-1}, mVs^{-1}, 5 mVs^{-1}, 10 mVs^{-1}, 25 mVs^{-1},50 mVs^{-1}, and 100 mVs^{-1} between the potential range of 3 – 0.1Vvs Li^{+}/Li: (see Figure 6.9).

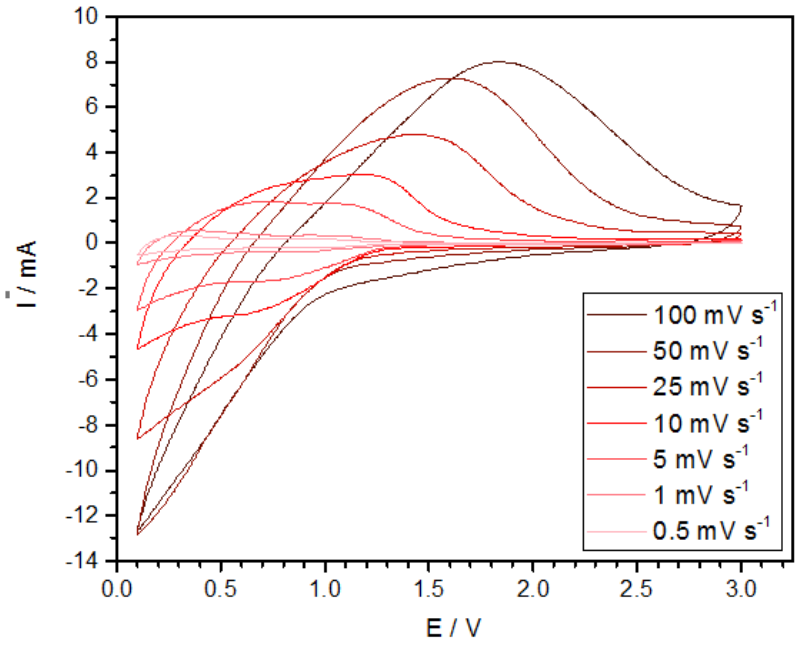

Figure 6. 9: CV curves of $KTaO_3$ at seven different scan rates speeds; 0.5mVs^{-1}, mVs^{-1}, 5 mVs^{-1}, 10 mVs^{-1}, 25 mVs^{-1},50 mVs^{-1}, and 100 mVs^{-1} for the 2nd cycle.

Figure 6.9; shows the initial four CV curves of the $KTaO_3$ electrode at a scan rate of 10 mVs^{-1}. The difference is significant between the first and the subsequent cycles. Two to three peaks were distinguished at 0.23V and 1.54V in the first cycle in the cathodic process. The possible explanation can be related to the full valence variation of Ta^{5+} to $Ta^{4+}$and the partial reduction Ta^{4+} to Ta^{3+} as a possible assign, along with significant irreversible phase transformation resulting in an irreversible capacity. (Han *et al.*, 2011; Long *et al.*)This is can be seen in figure 6.10 where the value of the practical capacity in the first cycle was much higher than the rest capacities of the subsequent cycles. The first cycle capacity was obviously high (approximately 105mAh/g), where the capacity of the next constitutive cycle was 23 mAh/g, with a difference of about 82 mAh/g. On the other hand, only a stable pair of peaks throughout can be recognised in the subsequent cycles cantered at approximately 0.56V/1.30V which indicated the electro chemical behaviour of our $KTaO_3$ electrode.

In general, a huge irreversible capacity took place during the first cycle which appeared as a drop in the overall practical capacity of this active material's electrode. (Inaba *et al.*, 2005; Matsumura *et al.*, 1995; Yoon *et al.*, 2001)

Figure 6.9 shows the significant difference between the first capacity and the subsequent capacities. The capacity profile was taken for 16 cycles. Whereas the cycles potential as a function of time can be seen in figure 6.10. in constant current cycling at 10 mA/g, as the cell potential ramping within the chosen potential window of 3.5V- 0.1V. The first cycle took considerable time to complete the cycle compared to the subsequence cycles. This is being due to the irreversible reaction where some of the lithium ions which are allocated inside the active material layers have transferred irreversibly. Meaning that less number of lithium ions will reversibly transfer back during the lithiation process.

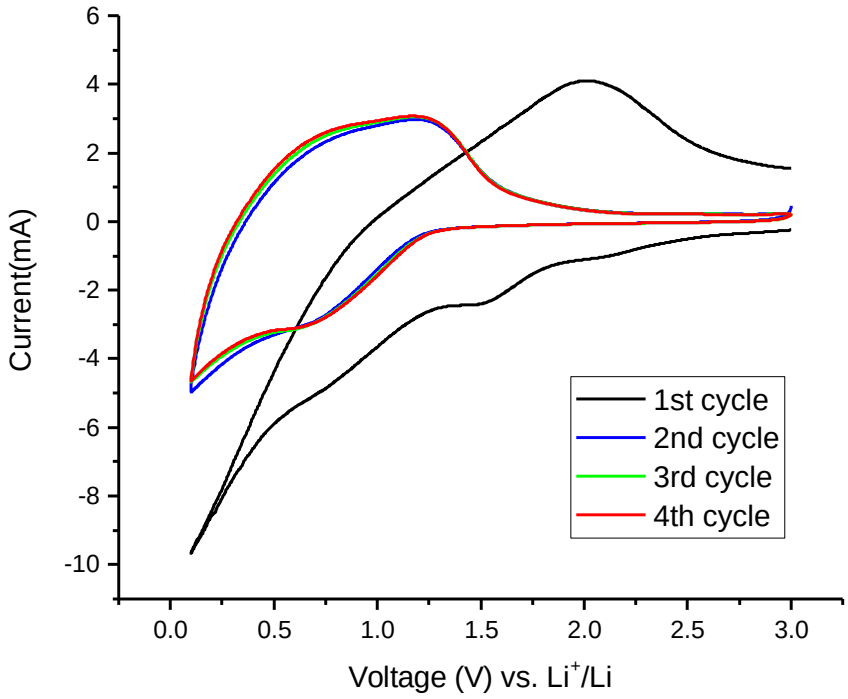

Figure 6. 10: Initial four CV curves of the $KTaO_3$ electrode at seven different scan rate speed of 10 mVs^{-1} between the voltage range of 3.0 -0.1 V vs.Li^+/Li.

Figure 11 shows the charge/discharge of a) 16 cycles, b) the second cycle where one can easily notice. from the graph, the specific capacity of the second cycle can be observed to be approximately 23mAh/g; with the active material mass being 7.58mg, i.e. the value of the capacity from the graph per unit mass of the active material.

Figure 6.12 illustrate constant current cycling at 10 mA/g, as the cell potential ramping within the chosen potential window of 3.5V- 0.1V. The first cycle took considerable time to complete the cycle compared to the subsequence cycles. This is being due to the irreversible reaction where some of the lithium ions which are allocated inside the active material layers have transferred irreversibly. Meaning that less number of lithium ions will reversibly transfer back during the de insertion process.

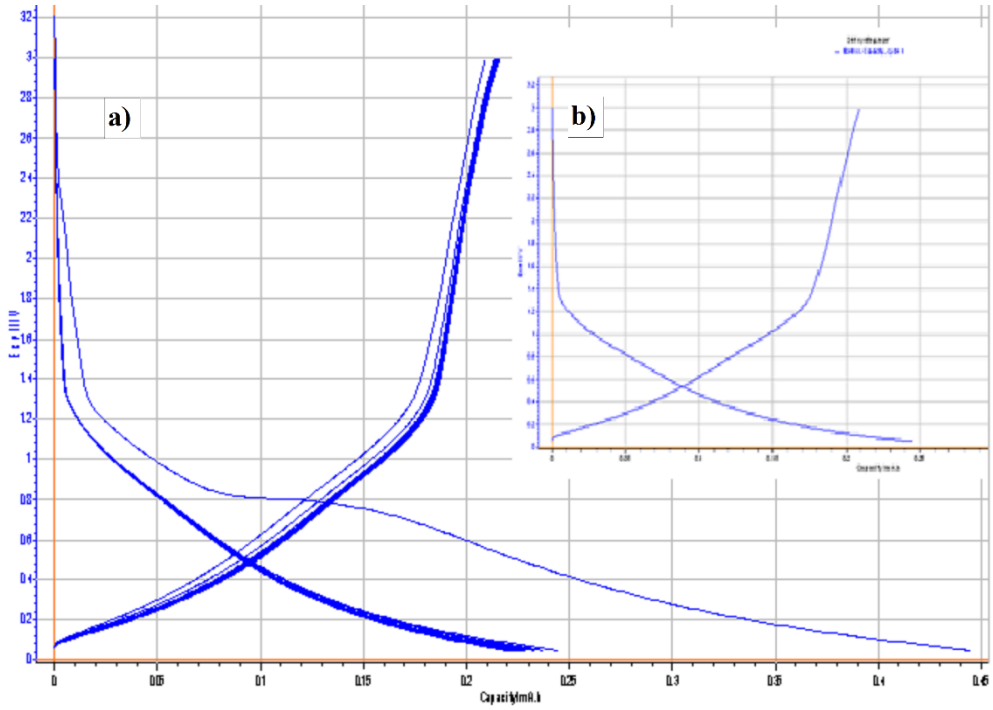

Figure 6. 11: Galvanostatic charge/ discharge profiles of the $KTaO_3$ electrode at 10mA/g for a) 16 cycles, b) The second cycle. A significant number of Li+ migrate one-way route during the first de-lithiation.

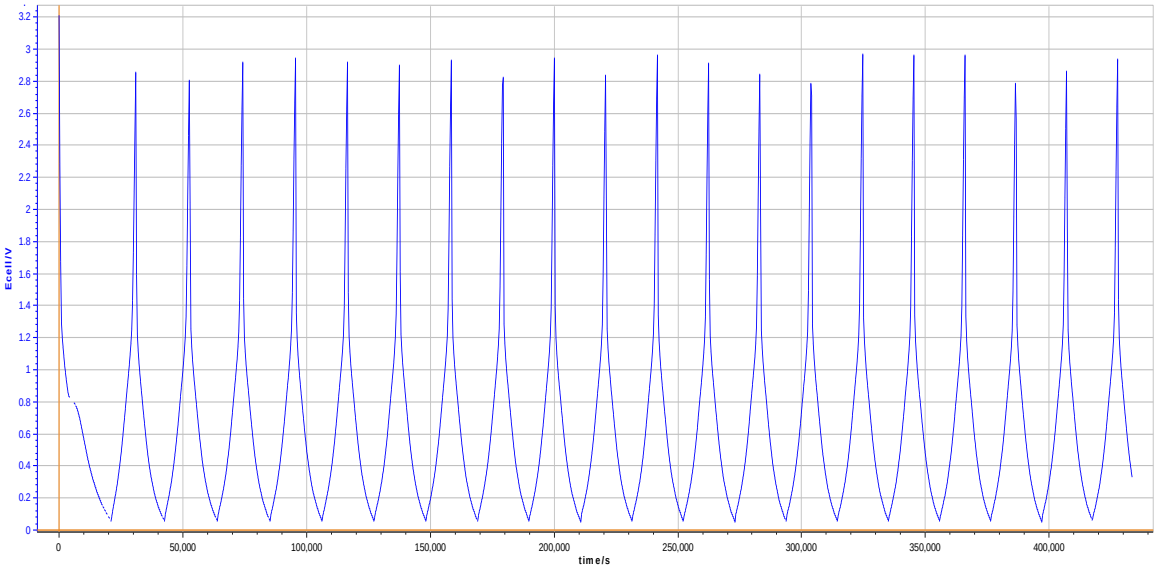

Figure 6. 12: Constant current cycling at 10 mA/g, as the cell potential ramping within the chosen potential window of 3.5V- 0.1V. The first cycle took considerable time to complete the cycle compared to the subsequence cycles. This is being due to the irreversible reaction where some of the lithium ions which are allocated inside the active material layers have transferred irreversibly. Meaning that less number of lithium ions will reversibly transfer back during the de insertion process.

6.4 Conclusion

Our work on the potassium tantalate was described and carefully listed. Two syntheses methods where used to produce this powder. The first attempt was the solid state reaction were two starting powders were used. Potassium carbonate and tantalum pent oxide were mixed and different high temperatures and time durations were applied resulting in multiphase of potassium tantalate and other impurities. In the second attempt, potassium tantalate was grown hydrothermally with a significant temperature difference compared to the solid state method. The perovskite structure is known for its growth under high temperatures like the case in the solid-state method, where we had multiple attempts to optimising the growth factors. Producing a single phase of potassium tantalate. The hydrothermal method produces a fine powder of highly pure perovskite $KTaO_3$.

The electrochemical test showed a huge irreversible capacity took place during the first cycle which appeared as a drop in the overall practical capacity of this active material's electrode. The more electrochemical test needs to be applied on this material as the active material in the Li-ion batteries before a final conclusion is given. Unfortunately, our project came to an end before we completed all the tests.

References

Chen, Z., Zhang, X. & Cross, L. E. (1983) Low-Temperature Dielectric Properties of Ceramic Potassium Tantalate (KTaO3). *Journal of the American Ceramic Society*, 66 (7): 511-515.

Duan, N., Tian, Z.-R., Willis, W. S., Suib, S. L., Newsam, J. M. & Levine, S. M. (1998) Hydrothermal synthesis and structure of a potassium tantalum defect pyrochlore. *Inorganic chemistry*, 37 (18): 4697-4701.

Han, H., Song, T., Bae, J.-Y., Nazar, L. F., Kim, H. & Paik, U. (2011) Nitridated TiO 2 hollow nanofibers as an anode material for high power lithium ion batteries. *Energy & Environmental Science*, 4 (11): 4532-4536.

Inaba, M., Uno, T. & Tasaka, A. (2005) Irreversible capacity of electrodeposited Sn thin film anode. *Journal of power sources*, 146 (1-2): 473-477.

Long, R. T., Sutula, J. A. & Kahn, M. J. Flammability of cartoned lithium-ion batteries.

Matsumura, Y., Wang, S. & Mondori, J. (1995) Mechanism leading to irreversible capacity loss in Li-ion rechargeable batteries. *Journal of the Electrochemical Society*, 142 (9): 2914-2918.

Shimada, S., Kodaira, K. & Matsushita, T. (1984) Sintering LiTaO3 and KTaO3 with the aid of manganese oxide. *Journal of Materials Science*, 19 (4): 1385-1390.

Sleight, A. (1968) New ternary oxides of mercury with the pyrochlore structure. *Inorganic Chemistry*, 7 (9): 1704-1708.

Yoon, S., Kim, H. & Oh, S. M. (2001) Surface modification of graphite by coke coating for reduction of initial irreversible capacity in lithium secondary batteries. *Journal of power sources*, 94 (1): 68-73.

Zhang, P., Zhang, J. & Gong, J. (2014) Tantalum-based semiconductors for solar water splitting. *Chemical Society Reviews*, 43 (13): 4395-4422.

Zhuroca, E. A., Zavodnik V. E., Ivanov. S. A., Tsirel'son, V. G. (1992) *Zhurnal Neoganicheskoi Khimii*, 37: 2406-2412.

Chapter 7

Conclusion

The main goal of this work; as briefly described in the first chapter, is to investigate the structure and electrochemical properties of three perovskites for the lithium-ion storage.

Summary of Work Done

Briefly, in Chapter 4 we exhibited our work on producing sodium tantalate Nano-particles. We were able to grow a pure phase of orthorhombic structure $NaTaO_3$ under a significantly low temperature using the hydrothermal method. All the structure characterisations where carried using the facilities at the physics department. The surface area to volume ratio was estimated using the statistical method. More accurate methods would be suggested if the work time for this project wasn't ended. Our material growth work has given us a better understanding of the produced structure.

Another successful growth of perovskite material was discussed in detail in Chapter 5. We were able to synthesise another type of perovskite structure in the nano size scale. lithium tantalate was produced using the chemical method; Sol-gel. We were able to produce a high surface area powder and made the attempt to examine it for the lithium and sodium ion storage.

In Chapter 6, our work on the potassium tantalate was described and carefully listed. The powder was grown hydrothermally with a significant temperature difference compared to the other widely used methods. The perovskite structure is known for its growth under high temperatures like the case in the solid-state method, where we had multiple attempts to optimising the growth factors. Producing a single phase of potassium

tantalate was a challenge, as the pyrochlore phase starts to form at temperatures lower than required for the perovskite phase to start formation.

The electrochemical performance was investigated in the WMG labs. The half-cell test was used to examine the active materials electrodes. Lithium metal was used as an anode in the test cells. Two types of cells were introduced. The coin cells and the two electrodes Swagelok cells. Sodium metal was used for a limited time to investigate the produced materials for the sodium-ion storage. Two materials were studied for the sodium-ion aim. Unfortunately, the results weren't encouraging, and more studies should be carried out in order to produce a greater understanding of the electrodes behaviour. Unfortunately, our project time came to an end and we had to stop our investigation before we were able to find alternative strategies to improve the electrochemical performance of the used electrodes and the material structure of the active material candidate, as well as the electrode stability.

Lithium tantalate, $LiTaO_3$ shoed the most stable electrochemical performance among the three materials; in spite of relatively high irreversible capacity; which indicate a significant structure irreversibility transformation the material went through in the first intercalation. Sodium tantalate, $NaTaO_3$, however, showed the least irreversible capacity, but a complicated electrochemical behaviour as well as the potassium tantalate, $KTaO_3$ material.

Suggestions for Future Work

Our latest investigations suggest the cubic structure perovskite as a promising candidate for the supercapacitors' electrodes. The more cubic the structure is, the more desirable it is for application as a lithium-ion storage material. In this work, we have produced near perfect nanocubes of sodium and potassium tantalates. Another study showed the importance of the tantalum oxide-based materials in the industry of solar

system and water splitting. Apart from the irreversible capacity obstacle, lithium tantalate exhibited a fair specific capacity and this should be investigated further. The reversibility of lithium-ion storage consistent under a high number of cycles was not thoroughly examined in this work. However, these materials or similar derivatives will be worthwhile for further studies as the ion storage for lithium or even sodium in the latest generation of ion storage materials. Initial electrochemical test cells were constructed and tested, but solid electrochemical results could not be gathered before the end of the project.

.

Abbreviations

XRD	X-Ray Diffraction
CB	Carbon Black
CV	Cyclic voltammetry
DEC	Diethyl carbonate
DMC	Dimethyl carbonate
EC	Ethylene carbonate
EDX	Energy-dispersive X-ray spectroscopy
EIC	Energy Innovation Centre
FEC	Fluoroethylene carbonate
HFP	hexafluoropropylene
HOMO	highest occupied molecular orbital
LCO	Lithium cobalt oxide
LFP	Lithium iron phosphate
LIB	Lithium-ion battery
LiFnFSI	lithium (fluoro-sulfonyl)(nonafluorobutanesulfonyl)imide
LiPDI	lithium dicyano-pentafluoroethyl-imidazole
LiTDI	lithium 4,5-dicyano-2-(trifluoromethyl)-imidazole
LiTF	lithium trifluoromethanesulfonate
LiTFSI	lithium bis(trifluoromethanesulfonyl)imide
LMO	Lithium manganese oxide

LNMO	Lithium manganese nickel oxide
LSV	linear sweep voltammetry
LTO	Lithium titanate oxide
LUMO	lowest unoccupied molecular orbital
NCA	Nickel cobalt aluminium oxide
NMC	Lithium nickel manganese cobalt oxide
NMP	N-Methyl-2-pyrrolidone
OCV	Open circuit voltage
PAA	Polyacrylic acid
PC	Propylene carbonate
PES	Photoelectron spectroscopy
PVdF	Polyvinylidene difluoride
SEI	Solid Electrolyte interphase
SEM	Scanning electron microscope
TEM	Transmission electron microscope
VC	vinylene carbonate
WMG	Warwick Manufacturing Group